UNIVERSITÀ DEGLI STUDI DEL SANNIO Benevento

Dipartimento di Ingegneria

Dottorato di Ricerca in Tecnologie dell'Informazione per l'Ingegneria
Curriculum Energia e Ambiente

XXXIV Ciclo

Process Design and Reactor Modelling for Integrated CO_2 Capture and Hydrogenation via Chemical Looping

Annunziata Forgione

Comitato scientifico

Prof. Francesco Pepe (relatore)

Prof. Piero Bareschino

Prof. Erasmo Mancusi

Coordinatore del Collegio di Dottorato

Prof. Massimiliano Di Penta

Authorship Attribution Statement

This thesis contains material from 3 papers published in the following peer-reviewed journal(s)/from papers accepted at conferences in which I am listed as an author/co-author.

Chapter 3 is published as E. Mancusi, P. Bareschino, A. Forgione and F. Pepe, "A two carriers reactor configuration for chemical-looping combustion in a packed-bed," *International Journal of Greenhouse Gas Control*, vol. 99, p. 103099, 2020.

Chapter 4 is a *Conference Paper* published as E. Mancusi, A. Forgione, P. Bareschino, C. Tregambi, F. Pepe, M. Urciuolo, P. Brachi and G. Ruoppolo, "A novel approach to methane production: Integration of solar hydrogen and chemical looping gasification," in *Proc. 15th SDEWES Conference*, Cologne, Germany, Sept. 2020.

Chapter 5 is published as E. Mancusi, P. Bareschino, A. Forgione, C. Tregambi and F. Pepe, "CO_2 methanation: Reactor modelling and parametric analysis," in *Computer Aided Chemical Engineering*, M. Türkay and R. Gani, Eds., vol. 50, pp. 585–590, Elsevier, 2021.

_____ _____

Date Annunziata Forgione

Acknowledgements

I would like to express my deepest gratitude to my supervisor, Prof. Francesco Pepe, for his constant support, invaluable guidance and encouragement throughout my doctoral studies. His expertise and insightful feedback have been fundamental in shaping both my research and academic development. I am sincerely thankful for his patience, dedication and mentorship during this important stage of my career. It has been an honour and a privilege to work under his supervision.

I am also sincerely thankful to the members of my research group - Prof. Piero Bareschino, Prof. Erasmo Mancusi and Dr. Claudio Tregambi - for their collaboration, thoughtful input and constant willingness to share their knowledge. Their expertise and fellowship have made this path both intellectually stimulating and personally rewarding. Working alongside such dedicated and supportive professionals has been an enriching experience that I will carry with me well beyond this PhD studies.

I am also grateful to the University of Sannio, Benevento and in particular to the Department of Energy Engineering, for providing me the opportunity and resources to pursue my PhD. The academic environment has been crucial in supporting my research activities.

Abstract

This thesis focuses on developing and numerically analyzing chemical looping technologies and integrated processes for sustainable energy conversion and storage. Chemical looping involves the cyclic reduction and oxidation of solid oxygen carriers to facilitate reactions such as combustion, gasification and methanation, with applications in low-carbon energy generation and renewable fuel production.

The research presented in this thesis is organized into three main directions: (a) the development and modelling of advanced Chemical Looping Combustion (CLC) fixed-bed reactor networks for methane combustion, (b) the design and numerical investigation of an integrated chemical looping gasification and methanation process for renewable methane production and energy storage and (c) the mathematical modelling and optimization of the methanation process for synthetic natural gas (SNG) production from biomass-derived syngas.

In the first part, a numerical model of a two-stage CLC reactor network is developed, where parallel pairs of reactors operate in series with Cu- and Ni-based oxygen carriers, respectively. The model assesses system performance in terms of thermal power output and gas stream composition. Results show that the two-stage configuration achieves comparable outlet gas temperatures to single-carrier reactors, allowing for shorter cycle times and requiring less active material. Furthermore, the two-stage system reduces the total number of reactor units needed, suggesting operational and material cost advantages.

The second part proposes an innovative process layout integrating chemical looping gasification of biomass and plastic solid waste with hydrogen production via water electrolysis to support methanation. The chemical looping gasifier employs Fe_2O_3 as oxygen carrier, while the methanation section consists of multiple adiabatic fixed-bed reactors with inter-stage cooling,

water condensation and product recycling. The system is designed to maintain a target H_2:CO:CO_2 molar ratio of 7:1:1 at the methanation inlet, with hydrogen produced by an array of electrolysis cells powered exclusively by renewable energy sources. The integrated model evaluates the process feasibility as a renewable energy storage solution via methane synthesis.

The third part focuses on the detailed modelling of the methanation step, which is critical for SNG production from biomass. Methanation is modelled as occurring in a series of adiabatic fixed-bed reactors with inter-stage cooling and partial product recycling. The developed mathematical model captures the essential kinetics and thermodynamics, enabling the analysis of various CO/CO_2 feed ratios and recycle fractions. This work provides guidelines for optimizing reactor performance and scaling up methanation processes.

In conclusion, this thesis contributes to the advancement of chemical looping technologies by focusing on the design, optimization and detailed analysis of innovative chemical looping processes, as well as the investigation of new materials suited for chemical looping applications.

Table of Contents

List of Figures

List of Tables

Nomenclature

E	energy
h	Specific enthalpy
$\dot{m}$	mass flow rate [kg s^{-1}]
n, m	Stoichiometric coefficients
p	partial pressure [bar]
R	universal gas constant, [8.314 J/mol/K]
R_{OC}	oxygen transport capability [kg oxygen/kg sample]
s	Specific entropy
T	temperature [°C]
t	time [s]

Greek symbols

α	Mass/heat transfer coefficient
β	Reaction rate coefficient
γ	Ratio of specific heats (adiabatic index)
η	Efficiency
κ	Thermal conductivity
ξ	Reaction progress
ρ	Density
ΔG	Gibbs free energy of reaction [kJ/mol]
ΔH	enthalpy of reaction [kJ/mol]
ω	specific work [kJ/kg]

Subscripts and superscripts

0	standard conditions
(g), (s)	Gas and solid phase
in	inlet
out	outlet
th	thermal

Acronyms

AR	Air Reactor
ASU	Air Separation Unit
BCLC	Biomass Chemical Looping Combustion
CCS	Carbon Capture and Storage
CCU	Carbon Capture and Utilization
CDCLC	Coal Direct Chemical Looping Combustion
CFB	Circulating Fluidised Bed
CFD	Computational Fluid Dynamics
CL	Chemical Looping
CLAS	Chemical Looping Air Separation
CLC	Chemical Looping Combustion
CLOU	Chemical Looping Oxygen Uncoupling
CSP	Concentrated Solar Power
DRM	Dry Reforming of Methane
EoS	Equation Of State
EPP	Equilibrium Partial Pressure
FEM	Finite Element Method
FR	Fuel Reactor
GT	Gas Turbine
HHV	Higher Heating Value
HP	High Pressure

HRSG	Heat Recovery Steam Generator
IGCC	Integrated Gasification Combined Cycle
iG-CLC	In-Situ Gasified Chemical Looping Combustion
LHV	Lower Heating Value
LP	Low Pressure
OC	Oxygen Carrier
OR	Oxidation Reactor
PCC	Pulverised Coal Combustion
POM	Partial Oxidation Of Methane
SMR	Steam Methane Reforming
SNG	Synthetic Natural Gas
ST	Steam Turbine
TGA	Thermogravimetric Analysis
TIT	Turbine Inlet Temperature

Chapter 1 Introduction

1.1 Background

The urgent need to mitigate greenhouse gas emissions and limit the global temperature increase to no more than 1.5°C above pre-industrial levels was reaffirmed during the COP21 (Conference of the Parties, December 2015) in Paris. A significant reduction in CO_2 emissions from fossil fuel combustion is critical to preventing further global warming and the associated adverse effects on the Earth's climate. CO_2 remains the most prominent greenhouse gas, with an estimated average atmospheric lifetime of around 300 years and 25% of emitted CO_2 persists indefinitely [1]. Approximately 50% of total anthropogenic CO_2 emissions stem from electricity and heat production activities [2]. In particular, coal was responsible for 40% of CO_2 emissions between 2018 and 2020, while oil and natural gas contributed 34% and 27%, respectively [3]. The combustion of fossil fuels not only releases large quantities of CO_2 but also emits other pollutants, creating significant environmental harm, particularly due to the processes involved in their extraction. The available options for the clean utilization of fossil fuels remain limited, which presents a considerable environmental challenge. Although there has been a decline in the construction of new coal-fired power plants, global coal production saw an increase of 4.3% in 2018 [4, 5]. Additionally, the relatively slow growth of renewable energy sources and the low cost of coal ensure that coal will continue to be a dominant energy source in the near future [6]. In this context, retrofitting existing and new coal-fired power plants with carbon capture and storage (CCS) systems presents a viable solution to generating affordable, low-carbon electricity. CCS technologies help decarbonize point sources of emissions, though they come with a trade-off in the form of reduced energy efficiency within thermal power cycles. Moreover, due to the intermittent nature of renewable energy sources, coal-fired power plants equipped with CCS could serve as a stable baseload power source for a decarbonized electrical grid [7].

Carbon capture technologies can generally be categorized based on their operational approach: post-combustion, pre-combustion, oxy-fuel combustion and chemical looping combustion. Post-combustion capture involves removing CO_2 from flue gases through various gas separation techniques, including physical absorption, chemical adsorption with sorbents, cryogenic separation and membrane-based methods [8]. Although post-combustion capture is commercially available, it is often costly due to the significant energy requirements involved in separating CO_2 from large volumes of combustion gases [9, 10]. Pre-combustion capture relies on the water-gas shift reaction, $CO + H_2O \leftrightarrow CO_2 + H_2$ ($\Delta H°298 = -41.09$ kJ/mol), to convert syngas, produced by the gasification of solid fuels or reforming of gaseous fuels, into a mixture of CO_2 and H_2 [11]. The CO_2 is then separated from the H_2, which can be used for power generation with zero carbon emissions. To date, pre-combustion capture has been predominantly implemented in hydrogen production plants, which represent the largest share of commercially deployed CCS capacities, along with natural gas processing [12]. However, this method also faces challenges such as energy losses due to the regeneration of sorbents in gas separation units [9]. Additionally, the drying of syngas before CO_2 capture with physical solvents presents technical challenges, along with substantial investment and operational costs [13].

Oxy-fuel combustion entails burning fuel in an atmosphere devoid of nitrogen and other inert gases found in air. In this process, pure oxygen is injected into the combustion chamber, typically obtained through cryogenic air separation. Following combustion, a pure CO_2 stream is captured by condensing the water vapor produced, thus facilitating inherent carbon capture. A portion of the generated CO_2 is recirculated back into the combustion chamber to control the flame temperature. Further purification of the CO_2 stream is required downstream to meet the pipeline specifications of >95%, ensuring its suitability for transportation, sequestration, or further use [14]. Currently, no commercial-scale oxy-fuel combustion plants are in operation [9]. The primary

cost associated with carbon capture in oxy-fuel combustion arises from the energy demands of the cryogenic air separation unit (ASU).

1.2 Chemical looping

Chemical looping (CL) technology utilizes solid intermediates to cyclically run a reaction into two or more distinct steps, preventing direct interaction between the reactants and facilitating the easier separation of products [15]. CL processes are known for their high energy conversion efficiency, reduced exergy losses and safer operation due to the elimination of gaseous oxygen [16].

This adaptable technique can be applied in a variety of processes, including fossil fuel combustion, water splitting, air separation and the production of high-value chemicals [16-19]. In most CL processes, a solid intermediate (typically a metal oxide, nitride, or hydride) transfers oxygen, nitrogen, or hydrogen between reactors, performing a specific part of the overall reaction. These intermediates, known as carriers, are mandatory to the function of chemical looping systems. Although recent interest has focused on nitrogen and hydrogen carriers, oxygen carriers (OCs) have been the primary focus of research to date [19]. In the context of carbon capture and storage, the relevant CL processes include chemical looping combustion (CLC), chemical looping air separation (CLAS), chemical looping reforming and chemical looping CO_2 capture (also referred to as sorbent looping or calcium looping).

Chemical Looping Combustion

Chemical looping combustion is considered one of the most promising technologies for carbon capture, offering the advantages of a low energy efficiency penalty and avoiding the need for gas-gas separation [20]. This is achieved by splitting the combustion process into two separate redox reactions that take place in the air reactor (AR) and the fuel reactor (FR), respectively. As depicted in Figure 1.1, the concept of CLC involves the transport of oxygen from the AR to the FR via solid oxygen carriers (OCs). In the FR, the fuel undergoes combustion with the lattice oxygen provided

by the OCs, forming CO_2 and H_2O, as represented by reactions (1.1) and (1.2). The reduced OCs are then re-oxidized in the AR by air, replenishing their lattice oxygen, as shown in reaction (1.3), thus completing the redox cycle. This process enables the complete oxidation (combustion) of hydrocarbon fuels to produce CO_2 and H_2O without direct contact with atmospheric air.

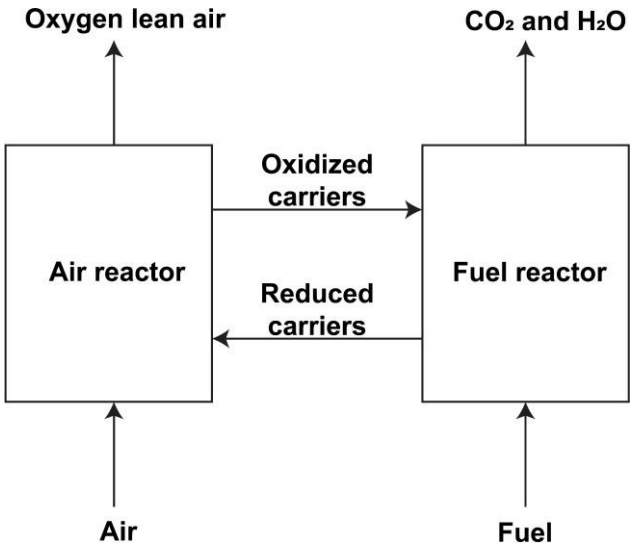

Figure 1.1 Visual representation of the chemical looping combustion process.

$$Me_xO_y\,(s) + CO\,(g) \rightarrow Me_xO_{y-1}\,(s) + CO_2\,(g) \quad (1.1)$$

$$Me_xO_y\,(s) + H_2(g) \rightarrow Me_xO_{y-1}\,(s) + H_2O\,(g) \quad (1.2)$$

$$2Me_xO_{y-1}\,(s) + O_2\,(g) \rightarrow 2Me_xO_y\,(s) \quad (1.3)$$

Chemical looping combustion (CLC) offers numerous advantages compared to conventional carbon capture technologies, as highlighted below:

• Pure CO_2 stream and net-zero emissions: Unlike traditional methods, CLC produces a pure CO_2 stream without the need for additional gas separation units. This distinctive characteristic enables the potential for net-zero CO_2 emissions and even negative emissions when using biomass [21,

22]. Moreover, the exhaust from the air reactor is a low-oxygen air stream, which poses no significant issues.

• Simplified operation: CLC removes the need for complicated air separation and CO_2 treatment systems, thereby simplifying the overall process.

• Strong thermodynamic and economic performance: Extensive analyses have shown that CLC outperforms other technologies in terms of both thermodynamic efficiency and economic feasibility [23-25].

• Lower emissions of harmful pollutants: CLC results in reduced emissions of harmful pollutants, such as SOx and NOx, compared to conventional combustion methods [11]. However, it is essential to note that chemical looping is still in its developmental stages, facing challenges related to scalability, material selection and system optimization. This thesis aims to contribute to the ongoing research and development efforts that are key to the commercialization of CLC, furthering progress toward a sustainable future.

1.2.1 Operational principles of chemical looping combustion (CLC)

When utilizing solid fuels, typical power plants can employ two distinct power cycle configurations: (1) direct combustion of fuel to generate steam for the Rankine cycle and (2) gasification of the solid fuel, followed by cleaning and combustion in a gas turbine. The first method, applied in pulverized solid fuel combustion (e.g., coal), is illustrated in Figure 1.2. The second method, which combines both the Rankine and Brayton cycles, is known as an integrated gasification combined cycle (IGCC), as shown in Figure 1.3.

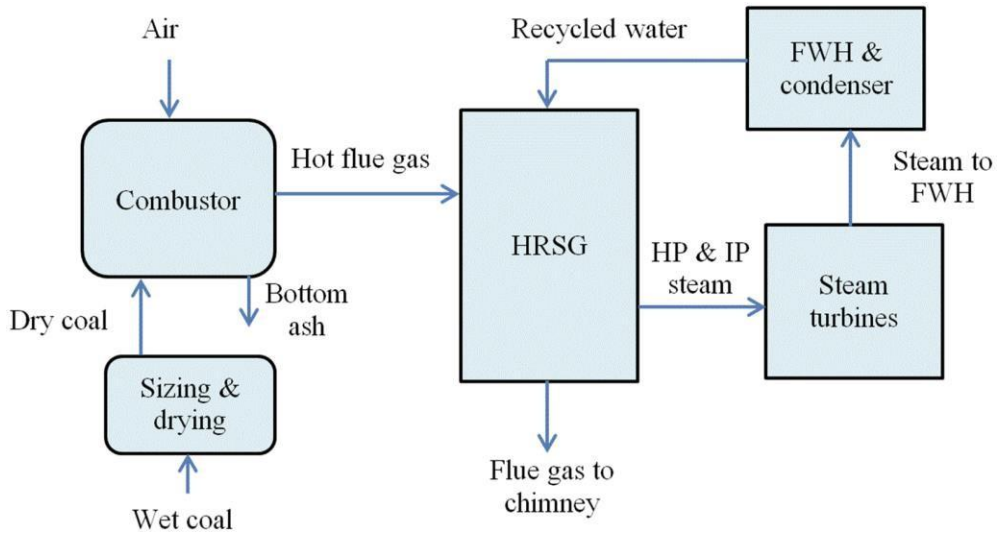

Figure 1.2 Schematic representation of power production using pulverized coal combustion technology (PCC) [26]

The CLC variants for PCC and IGCC are labeled iG-CLC (in situ gasified CLC) and IGCC-CLC (integrated gasification combined cycle CLC), with their respective process flow diagrams presented in Figure 1.4 and Figure 1.5.

iG-CLC refers to a process that integrates coal gasification with CLC [27]. It is sometimes called coal direct CLC (CDCLC) or coal-fired power plant CLC (CFPP CLC) in the literature. This process involves introducing oxygen carrier (OC) particles and fine coal powder into a reducer, where coal is first converted into volatile matter and char. The key reactions for this process are shown in reactions (1.4) - (1.9).

The char undergoes gasification in the presence of steam or CO_2, producing carbon monoxide (CO) and hydrogen (H_2) [16]. The oxygen carrier then reacts with the gasified products to generate water, CO_2 and heat. Since gasification and combustion occur in the same reactor, the process is called in-situ gasification CLC. Some oxygen carriers are also capable of releasing gaseous oxygen at combustion temperatures, a phenomenon known as chemical looping oxygen uncoupling (CLOU), as shown in reaction (1.8).

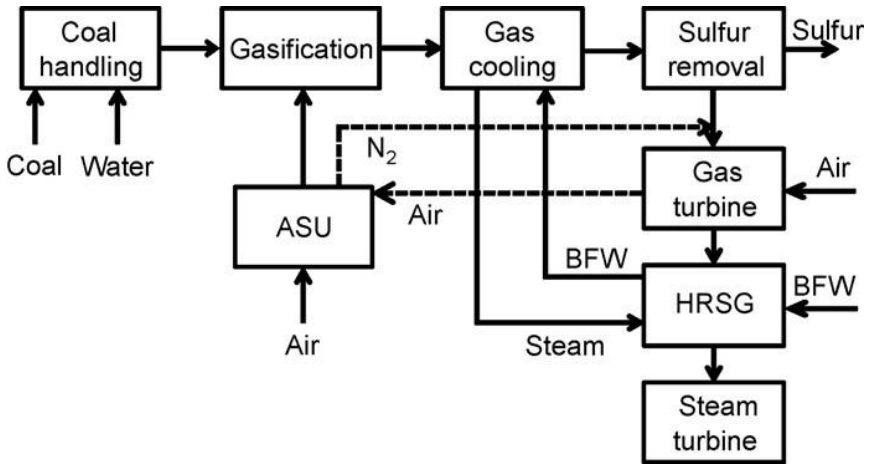

Figure 1.3 Schematic of power generation via a conventional Integrated Gasification Combined Cycle (IGCC) system without CO_2 capture [28].

$$\text{Coal} \rightarrow \text{Volatile matter} + \text{Char (C)} \tag{1.4}$$

$$\text{Char (C)} + H_2O \rightarrow H_2\,(g) + CO\,(g) \tag{1.5}$$

$$\text{Char (C)} + CO_2 \rightarrow 2CO\,(g) \tag{1.6}$$

$$H_2, CO, \text{volatile matter} + nMe_xO_y\,(s) \rightarrow CO_2\,(g) + H_2O\,(g) + nMe_xO_{y-1}\,(s) \tag{1.7}$$

$$nMe_xO_y\,(s) \rightarrow nMe_xO_{y-1}\,(s) + 0.5\,O_2\,(g) \tag{1.8}$$

$$\text{Char} + \text{Volatile matter} + \left(n + \frac{m}{2}\right) O_2\,(g) \rightarrow nCO_2\,(g) + mH_2O\,(g) \tag{1.9}$$

In the absence of CLOU, i.e., when iG-CLC (heterogeneous CLC) is in operation, the combustion reactions between the gas and solid phases occur exclusively on the surface of the solid oxygen carrier particles, as depicted in Figure 1.6. However, when CLOU materials are used, gaseous oxygen can leave the oxygen carrier, facilitating combustion reactions on the surface of the char [29]. The reduced oxygen carrier is then transported to either an air or oxygen reactor, where it

undergoes oxidation, releasing heat that can be harnessed for steam generation and electricity production.

The Integrated Gasification Combined Cycle Chemical Looping Combustion (IGCC-CLC) is a more complex system that integrates coal gasification with a combined cycle power plant and CLC [30]. In the IGCC-CLC process, coal or other solid fuels are initially gasified to produce syngas, which is then fed into the fuel reactor, where combustion occurs. Much like the iG-CLC process, the reduced oxygen carrier is oxidized in the air reactor. The flue gas from the air reactor, assuming it operates under elevated pressure, is directed to a gas turbine, where it expands to generate electricity. Finally, the heat recovered from the exhaust gases of both the fuel reactor and the gas turbine is used to generate steam, which is introduced into a steam turbine to produce further electricity.

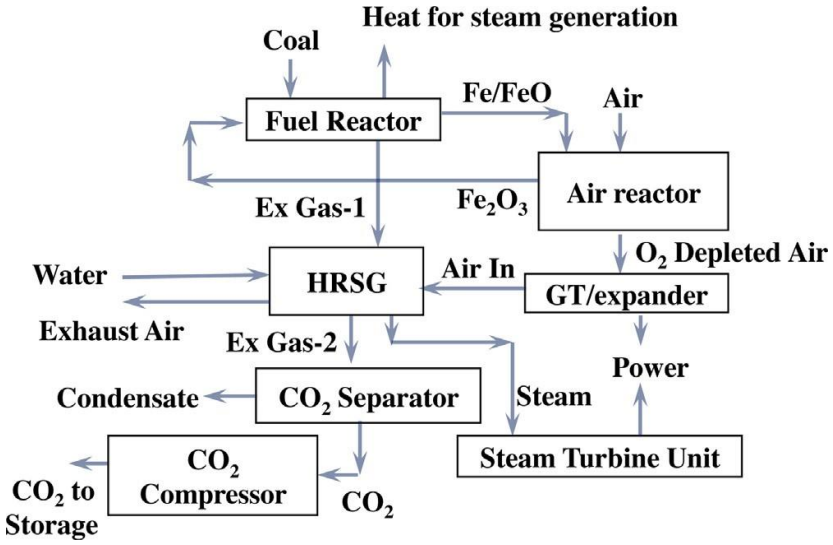

Figure 1.4 Schematic representation of power generation through in-situ gasification chemical looping combustion (iG-CLC) system [24].

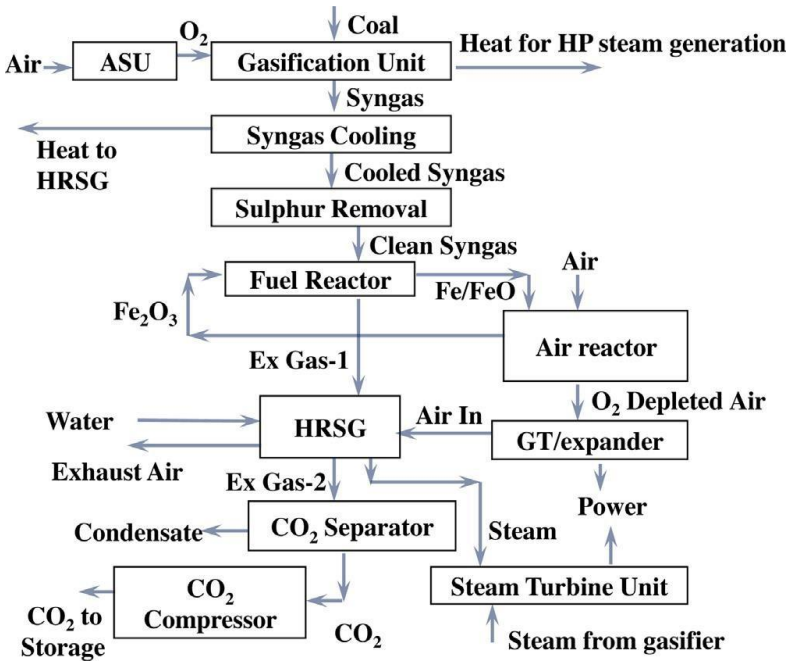

Figure 1.5 Schematic layout of power generation using integrated gasification combined cycle integrated with chemical looping combustion (IGCC-CLC) [24].

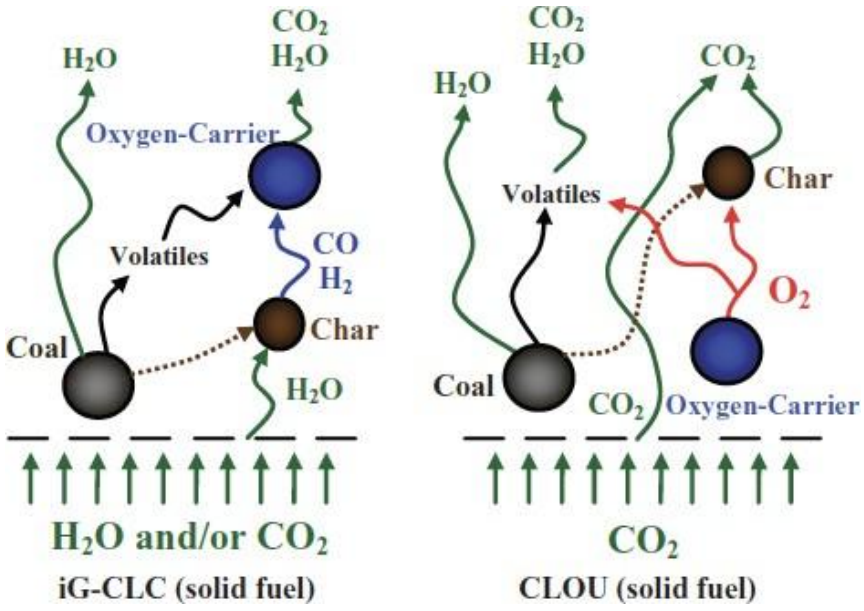

Figure 1.6 Comparative analysis of iG-CLC and CLOU approaches in the chemical looping combustion of solid fuels, with coal as a reference fuel [31].

1.2.1.1 Critical parameters governing the efficiency of Chemical Looping Combustion Power Plants

Several elements can affect the performance of a CLC power plant and some of these are discussed in detail below.

• Reactor Design

The design of the reactor plays a crucial role in determining the reaction kinetics, heat transfer efficiency and pressure drop across the system [32]. Factors influencing reactor design include the type of reactor, its size, configuration and the materials selected for construction. A well-designed reactor should facilitate optimal heat transfer, minimize energy losses and ensure mechanical strength and resistance to corrosion. Various reactor types have been explored for CLC applications, such as bubbling fluidized beds, fixed beds and circulating fluidized beds [33]. Each reactor type presents unique advantages and challenges in terms of operational efficiency, performance and ease of use. Furthermore, the materials chosen for construction must withstand high operational temperatures and pressures, minimize corrosion and resist mechanical wear caused by fluidized particles.

• Fuel Selection

The choice of fuel for a CLC plant can greatly influence its overall performance. Key fuel properties, including heating value, moisture content and ash content, must be carefully considered when designing the CLC system. Fuels with a higher heating value can boost energy production and improve the efficiency of the power plant. The moisture and ash content of the fuel can affect the combustion efficiency and CO_2 capture rate in the CLC reactor [34], while the particle size can impact both the pressure drop and the gas-solid mixing efficiency [35]. The ash content also has implications for ash deposition and erosion of the reactor walls, which can, in turn, affect reactor performance and its operational lifespan.

• Oxygen Carrier Selection

The selection of an oxygen carrier (OC) is another vital factor in the CLC process. The OC affects oxygen transfer rates, carbon capture effectiveness and the kinetics of the redox reactions. The essential properties of OCs, such as their ability to transport oxygen, react with fuels, endure high temperatures, resist coke formation, avoid agglomeration and withstand attrition, are critical for the success of the chemical looping process [36]. Additionally, desirable OCs should exhibit excellent fluidization properties, environmental sustainability and low production costs.

• Operating Conditions

The operating conditions of a CLC power plant, including temperature, pressure and flow rates, can significantly impact system efficiency. These factors influence the rate of reaction, heat transfer and pressure drop across the system. Among these parameters, the temperature of the air reactor is recognized as a critical factor that affects the performance of the CLC system. Studies have shown that air reactor temperature has a substantial impact on the overall efficiency. For example, higher air reactor temperatures can lead to increased NOx formation [37]. In a three-reactor CLC system, consisting of the air, steam and fuel reactors (as illustrated in Figure 1.7), a reduction in air reactor temperature from 1000 °C to 900 °C resulted in a 1.6% decrease in energy efficiency [38]. However, a study by Keairns et al. [39] suggests that raising the air reactor temperature does not lead to significant performance improvements or cost reductions. Although many modeling studies assume air reactor temperatures around 1000 °C, practical constraints such as sintering, agglomeration and reduced mechanical strength of oxygen carriers at high temperatures typically limit the operating temperature of solid fuel CLC systems to below 1000 °C in experimental studies [40].

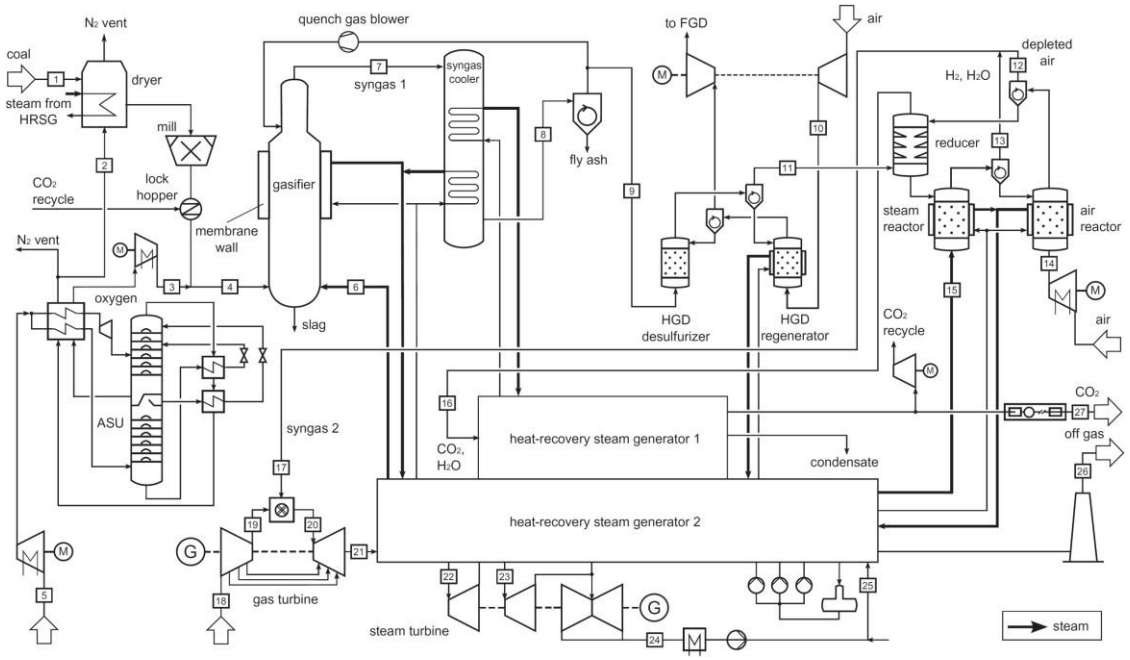

Figure 1.7 Configuration layout of a triple-reactor IGCC-CLC power plant [38].

In principle, the upper temperature limit for the operation of Chemical Looping Combustion (CLC) is crucial for its integration with various power generation cycles. Generally, the iG-CLC configuration is particularly well-suited for coupling with an indirectly heated steam Rankine cycle due to its relatively low operating temperature range. The upper temperature limit for CLC operation typically falls between the turbine inlet temperature (TIT ~ 1200 - 1500 °C) of a standard Brayton cycle in an Integrated Gasification Combined Cycle (IGCC) power plant and that of a conventional subcritical steam Rankine cycle (< 560 °C). As a result, CLC typically performs better when implemented in the iG-CLC configuration, showing less compatibility with IGCC systems. Numerous studies have found IG-CLC to be more efficient than other configurations, such as IGCC-CLC, pre-combustion capture and ASU oxy-combustion. For instance, Mukherjee et al. [24] demonstrated that iG-CLC outperforms other CLC configurations in terms of efficiency for a given operating pressure and fuel type. Similarly, Cormos et al. [41] reported that Fe-based iG-CLC exhibits higher efficiency than IGCC-CLC when operating at 900 °C. However, other

research has suggested that IGCC-CLC may outperform some alternative technologies [25, 42]. Erlach et al. [23] observed that, under higher TIT (>1400 °C), the performance of pre-combustion capture with physical absorption becomes comparable to CLC. In conclusion, selecting the most appropriate CLC configuration depends on the specific application and the operational conditions of the power generation cycle.

• Operating Pressure

The operating pressure is another critical factor influencing the overall efficiency of CLC systems. Pressurizing CLC systems can lower capital costs, with moderate pressurization (0.5–1.0 MPa) generally delivering strong performance [43, 44]. Research on pressurized CLC systems typically suggests that 0.5 MPa is the optimal pressure, with peak efficiencies for iG-CLC achieved within the 0.1 – 3.0 MPa range [26].

• Type of Power Cycle Used

The type of power cycle employed in a CLC-based power plant also impacts its efficiency. For example, a supercritical steam cycle can provide higher efficiency compared to a subcritical steam cycle. By using advanced engineering materials, both the TIT and the operating pressure of steam turbines can be increased, thereby improving the performance of coal-fired power plants. Thus, understanding the effects of higher TIT on the feasibility of various CLC configurations is crucial. A recent process modeling study showed that using Mn-based carriers in iG-CLC, coupled with a supercritical steam cycle operating at 28.0 MPa, results in a net electrical efficiency of 41.6% [45]. In contrast, utilizing iron ore in an iG-CLC system, paired with different types of steam cycles (ranging from subcritical to ultra-supercritical), yields net efficiencies between 37.2% and 40.9% [26]. Moreover, integrating a combustor with an ultra-supercritical steam cycle leads to only a 2.5% reduction in efficiency penalty when compared to an air-fired circulating fluidized bed (CFB) ultra-supercritical boiler without carbon capture [46]. In summary, advanced engineering materials

can significantly enhance the efficiency of coal-fired power plants by increasing the TIT and operating pressure of steam turbines.

1.2.1.2 Oxygen carriers

The oxygen carriers used in chemical looping systems must be capable of withstanding multiple cycles of redox reactions without significant degradation in their physical or chemical structure. These carriers need to facilitate both the reduction and oxidation stages efficiently, in terms of both thermodynamic feasibility and reaction kinetics. A common approach when choosing oxygen carriers is to use an Ellingham diagram, which visually represents the standard free energy of oxidation (ΔG°) as a function of temperature for various metal oxides. This diagram serves as a practical tool for an initial evaluation of the thermodynamic stability of different metal oxides under varying redox conditions, which depend on factors such as temperature and oxygen partial pressure. For example, the Ellingham diagram is helpful for determining whether a metal oxide can be reduced to its metal form by carbon or other reducing agents, thus aiding in the selection of appropriate oxygen carriers for specific chemical looping applications. The slopes of the lines in the diagram (illustrated in Figure 1.8) correspond to the enthalpies involved in the reduction of metal oxides, while the y-intercept at 0 K indicates the standard free energy for the reduction process. The diagram also features several key lines that represent important reactions. One such line, representing metal oxide formation (Metal → Metal oxide), shows the energy required for a metal to oxidize and form its respective metal oxide. A steeper negative slope along this line indicates greater thermodynamic stability for the metal oxide. Metals situated below this line are more prone to oxidation, leading to the formation of oxides as temperature increases. This line is instrumental in predicting the oxidation behavior of metals.

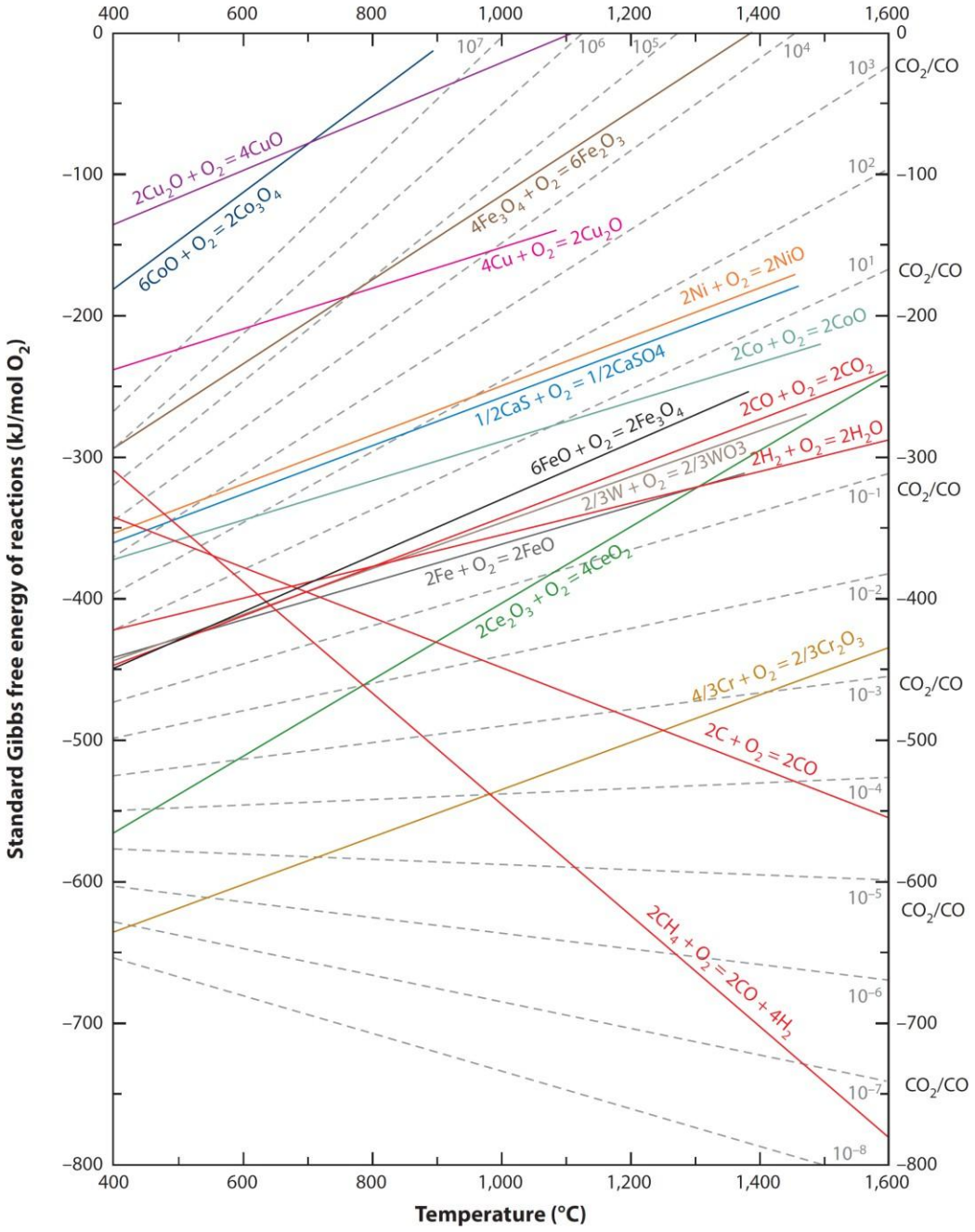

Figure 1.8 Ellingham diagram illustrating the temperature-dependent stability of various metal oxide systems [59].

The formation of water vapor ($H_2 + 0.5O_2 \rightarrow H_2O$) is represented by a line that signifies the energy released when hydrogen and oxygen gases react to produce water vapor. This exothermic reaction

is utilized in high-temperature processes and serves as a source of oxygen for certain reactions. Metals located beneath this line can react with water vapor, leading to the formation of oxides.

Similarly, the line for carbon dioxide formation ($CO + 0.5O_2 \rightarrow CO_2$) demonstrates the energy released when carbon monoxide and oxygen gas react to form carbon dioxide. This exothermic process plays a crucial role in applications involving carbon-based gases at elevated temperatures. Metals found below this line can interact with carbon monoxide, forming oxides in the process.

A simplified version of this diagram is presented in Figure 1.9. As depicted in Figure 1.9, redox-active metal oxides can be grouped into three categories based on their oxidation potential, each corresponding to different types of applications [47]. The strong oxidizing agents in Zone A, including oxides of Nickel (Ni), Iron (Fe), Manganese (Mn), Copper (Cu) and Cobalt (Co), are suitable for both partial and complete oxidation of hydrocarbon fuels. The materials in Zone B (e.g., CeO_2 and WO_3) are capable of partial oxidation, but not full oxidation, while those in Zone C (e.g., Cr_2O_3 and SiO_2) are considered inert and unsuitable as oxygen carriers.

For Chemical Looping Combustion (CLC) applications, the development of oxygen carriers primarily focuses on the metal oxides from Zone A. Oxygen carriers are typically synthesized using techniques such as solid-state reactions [48], the sol-gel method [49], co-precipitation [50], spray drying [51], hydrothermal synthesis [52] and flame spray pyrolysis [53], before being tested for CLC performance in fixed-bed reactors and thermogravimetric analysis (TGA) [54]. Alternatively, oxygen carriers can be obtained inexpensively from ores, minerals, by-products and waste from industrial processes like steel production [55].

A recent review on CLC technology highlights that out of 11,000 hours of pilot-scale operation of CLC [56], 8,000 hours were conducted using manufactured synthetic oxygen carriers, while the remainder utilized natural materials [57].

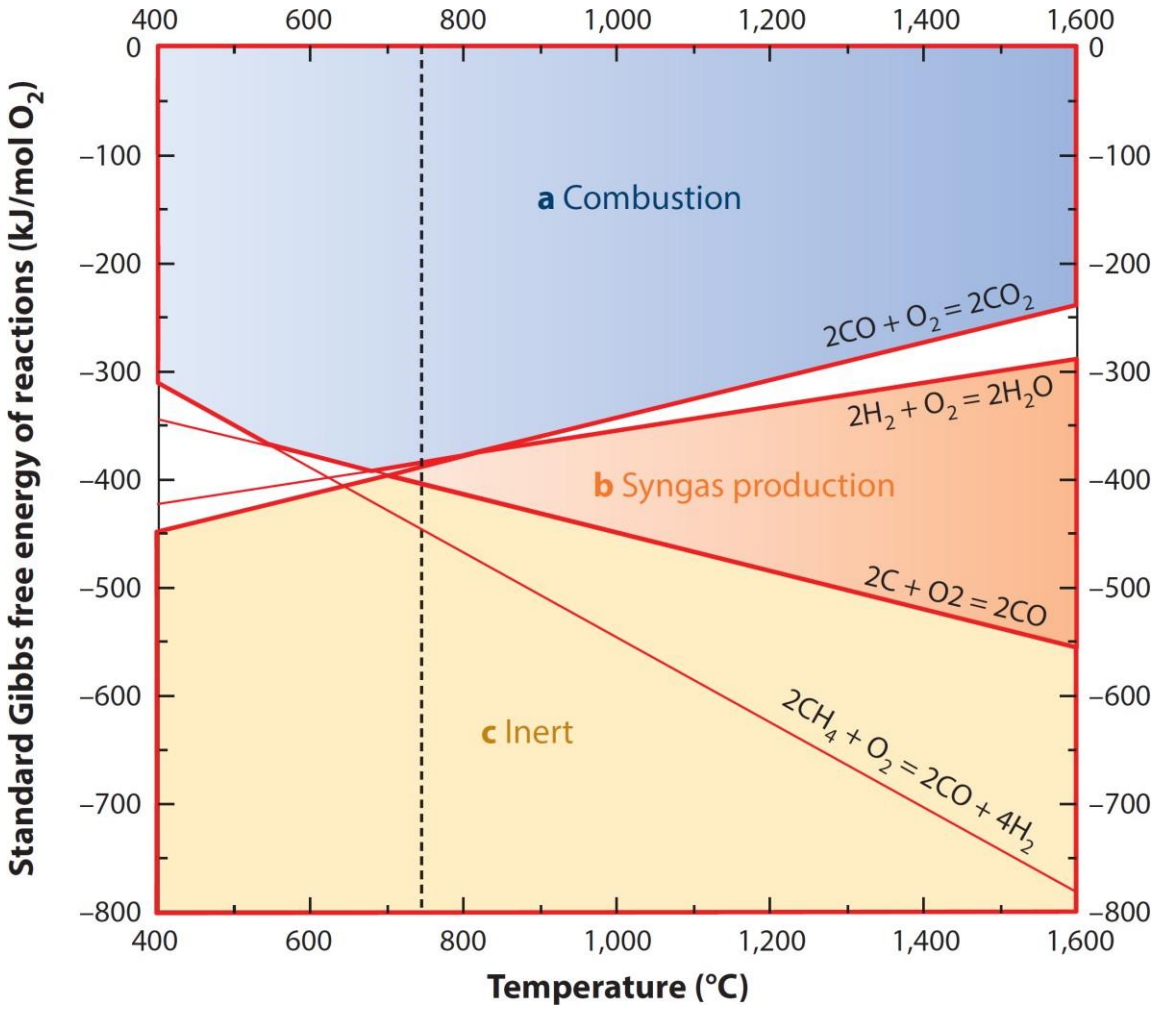

Figure 1.9 Classification of metal oxide behavior in chemical looping according to the Ellingham diagram regions. [47].

Monometallic metal oxides, when used in isolation, typically exhibit limited suitability as oxygen carriers in chemical looping systems due to two principal deactivation pathways. Firstly, high-temperature operation promotes sintering, a process further intensified by recurrent phase transitions. In the second instance, the mechanical transfer of oxygen carrier particles between the fuel and air reactors results in significant attrition and particle agglomeration [58]. These effects can lead to defluidisation, a reduction in specific surface area and eventual particle loss through

elutriation. Notably, monometallic oxides are especially vulnerable to all aforementioned degradation mechanisms.

To mitigate these drawbacks, considerable research has been devoted to enhancing oxygen carrier performance by incorporating support materials such as Al_2O_3, SiO_2, TiO_2, ZrO_2, YSZ and bentonite [60, 61]. These supports not only strengthen the mechanical integrity of the carriers but also expand their surface area and introduce additional reactive sites, thereby improving the efficiency of the chemical looping combustion (CLC) process and reducing the overall bed inventory required. Furthermore, these materials aid in the retention of the active phase within the system by shielding it from direct contact with the reactor walls, which minimizes the need for frequent replenishment [62]. Importantly, they also contribute to the thermal stability of the carriers, helping to preserve their surface properties throughout extended redox cycling at elevated temperatures.

Among the various options, NiO-based oxygen carriers are particularly advantageous for natural gas combustion. Upon reduction, NiO yields metallic Ni, which effectively catalyses the cleavage of C–H bonds in methane and other hydrocarbons present in natural gas. To enhance both thermal durability and mechanical resilience, NiO is commonly supported on non-reducible oxides like ZrO_2 and TiO_2 [63]. A composite of NiO and $NiAl_2O_4$, for instance, demonstrated stable reactivity in a 10 kW CLC reactor over 160 hours of operation with natural gas, although some agglomeration was observed [64]. Despite their high activity and robustness, NiO-based oxygen carriers necessitate the pre-removal of sulphur compounds from the fuel, as Ni readily forms nickel sulphides and sulphates under sulphur exposure—compounds that are toxic, carcinogenic and pose serious environmental risks [65].

Cu oxides have been widely explored as oxygen carriers in chemical looping combustion (CLC) systems. A major limitation of Cu is its relatively low melting point (~1079 °C), which promotes

sintering and particle agglomeration under operating conditions. One strategy to mitigate these effects involves dispersing Cu-based OCs onto various support materials to enhance their thermal stability and mechanical robustness. For example, CuO supported on γ-Al_2O_3, α-Al_2O_3, $MgAl_2O_4$ and NiO/γ-Al_2O_3 has been employed in continuous CLC operations at 950 °C using methane as the fuel, showing complete conversion without evidence of defluidisation or particle agglomeration [66].

In a CLOU (Chemical Looping with Oxygen Uncoupling) test without fuel injection, a CuO loading of 60 wt% on $MgAl_2O_4$ exhibited stable performance, maintaining both high oxidation and oxygen release rates [51]. Nonetheless, the trial was halted after 40 h due to the generation of excessive fines from the air reactor's entrainment system. In a separate 120 kW pilot CLC unit, a CuO OC containing 9 wt% was capable of fully converting CO and H_2 (produced via biomass steam gasification) into CO_2 and H_2O [67]. However, CuO shows limited reactivity with methane, achieving only 53% and 64% conversion at 850 °C and 900 °C, respectively. Using Al_2O_3 as a support can mitigate attrition and agglomeration issues, but the formation of a $CuAl_2O_4$ spinel phase tends to reduce the CLOU effectiveness of CuO [56]. Moreover, the comparatively high cost of copper means its OCs must demonstrate significantly longer operational lifespans to be economically viable.

Manganese-based OCs have primarily been studied for the CLC of gaseous fuels, including natural gas and syngas. Research involving Mn_2O_3 supported on magnesia-stabilised zirconia revealed a greater suitability for syngas conversion over natural gas [68]. Similar findings emerged from studies on Mn-Fe mixed oxide carriers, derived both synthetically and from natural mineral sources, reinforcing the conclusion that Mn-based OCs are less effective with natural gas [69].

Despite their promising CLOU characteristics, cobalt-based OCs are rarely investigated due to high toxicity and cost concerns. Nonetheless, tests using cobalt oxide supported on Al_2O_3 in a

50 kW CLC setup running on methane achieved a fuel conversion efficiency of 96.6% over 25 h [70]. However, mechanical degradation during prolonged operation curtailed further testing.

Iron-based OCs are among the most extensively researched, primarily due to iron ores' abundance and low cost [36]. From a thermodynamic perspective, the reduction of Fe_2O_3 to Fe_3O_4 is more favourable than that of NiO to metallic Ni. Iron is also non-toxic and environmentally benign [71]. Many studies have focused on synthetic iron oxides; for instance, an alumina-supported OC with 17 wt% Fe_2O_3 tested in a 120 kW methane CLC unit achieved a fuel conversion rate of 60% at an oxygen carrier-to-fuel ratio of 4.5–5.0 [72].

Although Fe-based OCs have been predominantly used with gaseous fuels, their application in solid fuel CLC has grown due to the role of bioenergy with carbon capture and storage (BECCS) in delivering negative emissions. Technical challenges such as ash and char separation make solid fuel CLC more complex, but iron oxides' magnetic properties offer advantages in separating OCs from residual ash and char. For example, when coal was employed as the feedstock, Fe_2O_3 carriers achieved carbon conversion rates as high as 95% at temperatures exceeding 900 °C [71]. Nevertheless, Fe-based materials are limited by their relatively low oxygen transport capacity and poor reactivity with methane [73].

1.2.2 Chemical looping air separation (CLAS)

Chemical Looping Air Separation (CLAS) is a high-temperature process that operates on principles analogous to Chemical Looping Combustion (CLC). It enables the generation of oxygen-rich gas streams through the reversible thermal decomposition of solid metal oxide materials [17]. The separation of oxygen occurs via a redox cycle consisting of two distinct reactions:

$$MexOy{-}2\ (s) + O_2\ (g) \rightarrow MexOy\ (s) \qquad (1.10)$$

$$MexOy\ (s) \rightarrow MexOy{-}2\ (s) + O_2\ (g) \qquad (1.11)$$

As in CLC, the CLAS system involves two primary reactors: an oxidation reactor and a reduction reactor, where reactions (1.10) and (1.11) take place, respectively. A schematic representation of the CLAS process is provided in Figure 1.10.

According to Figure 1.10, metal oxides in their fully oxidised form are introduced into the reduction reactor. In the presence of a carrier gas, commonly steam or CO_2, they undergo reaction (1.11), releasing gaseous O_2 into the carrier stream. This O_2-enriched gas mixture can be utilised as an oxidising agent in processes such as oxy-fuel combustion. The reduced metal oxide particles are subsequently cycled back to the oxidation reactor, where reaction (1.10) occurs upon contact with heated air. The air, now depleted of oxygen, can be employed to preheat incoming air or, under pressurised conditions, expanded in a gas turbine for power generation.

Theoretically, CLAS is an energy-efficient process since the total heat exchanged across the redox cycle is zero. Furthermore, the oxygen carriers also function as thermal vectors, transferring energy from the exothermic oxidation (1.10) to the endothermic reduction (1.11).

In conventional oxy-fuel combustion systems, oxygen is typically supplied via cryogenic Air Separation Units (ASUs), resulting in a 4–6% energy efficiency loss for oxygen of 95% purity and up to a 10% loss for 99.5% purity O_2 [74]. These efficiency penalties may negate the economic advantages of CO_2 capture via oxy-fuel combustion. Historical efforts to circumvent cryogenic and adsorption-based air separation have explored alternatives such as temperature swing absorption using alkali nitrates/nitrites, electrochemical methods and thermochemical water splitting [17]. However, these approaches have seen limited adoption due to challenges in thermodynamic efficiency and scalability.

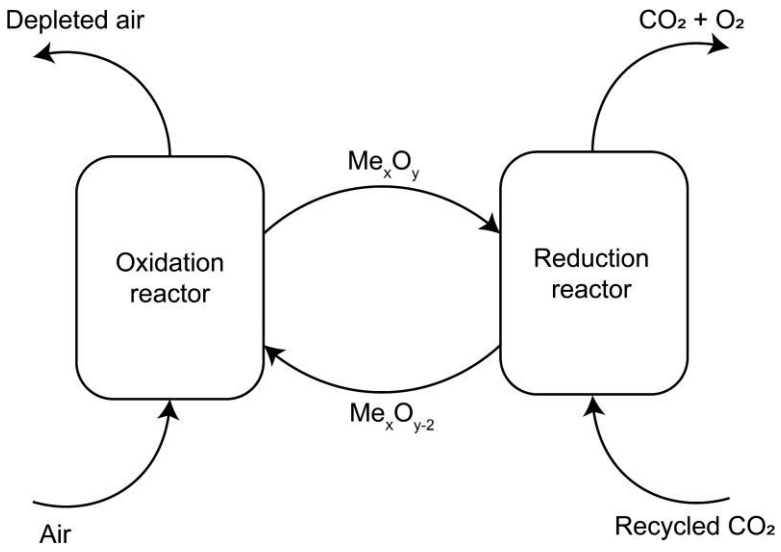

Figure 1.10 Schematic of the CLAS process.

For a metal oxide system to be considered suitable for chemical looping air separation (CLAS), it must be capable of undergoing both reactions (1.10) and (1.11) under favorable temperature and gas environment conditions. Figure 1.11 presents the standard Gibbs free energy changes (ΔG) for the reaction of 1 mol of CO with different redox couples as a function of temperature. A more negative ΔG indicates a greater tendency of the oxide to completely oxidize CO to CO_2, thereby signifying stronger oxidizing properties [47]. At elevated temperatures, oxides such as CuO, Co_3O_4 and Mn_2O_3 approach the reference line for gaseous O_2, suggesting their ability to decompose and liberate molecular oxygen at a partial pressure of 1 atm.

Among the various 3d transition metal oxides, redox couples like MnO_2/Mn_2O_3, Mn_2O_3/Mn_3O_4, CoO/Co_3O_4 and CuO/Cu_2O emerge as particularly promising candidates for CLAS applications. Ternary oxides such as $SrFeO_3$ have also demonstrated exceptional performance in CLAS systems [75–77]. However, in mixed oxygen compounds, the extent of oxygen release can be highly sensitive to the concentration of oxygen vacancies or deviations from stoichiometry—this is particularly evident in perovskite-type oxygen carriers [78].

Moreover, recent advancements have explored ternary oxides like $SrFeO_3$ for their potential to deliver CLOU (chemical looping with oxygen uncoupling) activity comparable to that of conventional materials. These compounds may mitigate issues commonly associated with traditional CLOU oxygen carriers, including performance degradation, thermal deactivation, physical disintegration, particle agglomeration and economic feasibility concerns [56].

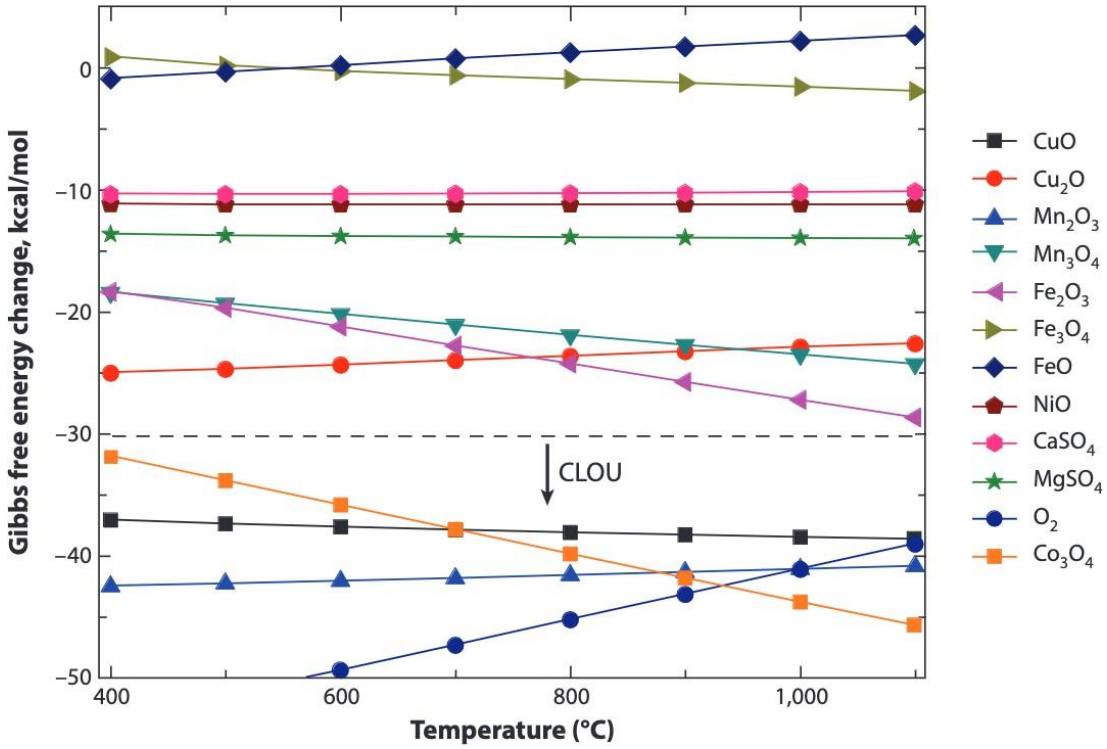

Figure 1.11 Gibbs free energy change of reduction of different oxygen carriers with 1 mol of CO [47].

1.2.3 Chemical looping reforming

In recent years, global focus has increasingly shifted toward the generation of clean energy and the mitigation of greenhouse gas emissions [79]. Over the last several decades, fossil fuels like coal and petroleum have served as the primary energy sources, significantly contributing to the sharp rise in atmospheric CO_2 levels, from 310 ppm in 1960 to 419 ppm by 2021, raising major

environmental alarms [80]. Anthropogenic emissions of greenhouse gases are directly associated with critical ecological consequences such as global warming, rising sea levels, ocean acidification and the extinction of various species [81]. As a result, adopting effective strategies and increasing reliance on renewable energy resources are essential for curbing global CO_2 emissions.

Hydrogen has emerged as a promising alternative to traditional carbon-based fuels, offering a viable path to diminish the effects of climate change [82]. Its zero-emission profile, high energy content and widespread availability make hydrogen an attractive candidate for clean energy applications [83]. Furthermore, with the global population and industrial activity continuously rising, hydrogen demand is expected to grow correspondingly [84].

Despite the current dominance of carbon-intensive fuels, which provide around 85% of global energy needs, projections indicate that hydrogen could fulfill up to 90% of global energy demand by the year 2080, underscoring its anticipated significance in the future energy landscape [85]. Key industries, including food processing, metal treatment, chemical production, petroleum refining, glass purification, hydrocracking and fuel cells, already utilize hydrogen in various capacities [86]. Nevertheless, to enable hydrogen to serve as a mainstream energy source, it must be produced through sustainable and efficient methods. Hydrogen is typically categorized into three main types, grey, blue and green, depending on the production method and feedstock involved [87].

Among these, green hydrogen stands out for its minimal environmental footprint compared to its grey and blue counterparts [88]. Considerable progress has recently been made in addressing material, cost and technical challenges related to green hydrogen production from renewable sources, with expectations that production costs could decrease by up to 70% within the next ten years [87].

Hydrogen can be generated through various technological pathways, including biological methods, photoelectrochemical systems, high-temperature thermolysis, water electrolysis, gasification of coal or biomass and reforming of natural gas or biogas [89]. Selecting the optimal production route depends on multiple considerations such as system integration, technological readiness, resource availability, economic viability, efficiency and environmental impact [90]. Among the available technologies, chemical looping represents a particularly innovative and promising method for hydrogen production coupled with CO_2 capture [91]. This approach involves a cyclic redox process in which a solid metal oxide serves as an oxygen carrier between air and fuel [92]. From an energy efficiency and environmental standpoint, chemical looping offers a versatile platform capable of converting a range of feedstocks into valuable products like ammonia, alkenes, syngas and H_2/CO, all while enabling low-cost CO_2 capture [93].

Depending on the composition of gas products and the source of oxygen atoms involved, this technology finds utility in diverse processes including chemical looping hydrogen production, chemical looping reforming (CLR), chemical looping gasification and chemical looping combustion [94]. The success of chemical looping technologies largely hinges on two critical aspects: the appropriate selection of oxygen carriers and the efficient design of the reactor system. These factors have guided extensive research efforts aimed at advancing oxygen carrier materials [95]. Over the years, the literature has seen numerous reviews covering various chemical looping applications, with a particular focus on the development of oxygen carriers tailored to specific feedstocks or CLR configurations. The CLR process involves fuel oxidation through the cyclical redox activity of a solid oxygen carrier. One major benefit of this system is the ability to supply the heat required for hydrogen production without relying on costly oxygen generation, avoiding both the mixing of air with carbon-rich gases and the consumption of produced hydrogen [96]. The

endothermic reactions in the fuel reactor are thermally sustained by the high-temperature solids circulated from the air reactor, thus eliminating the need for external heat sources.

A notable advantage of the a-CLR approach is the potential to generate a pure N_2 stream at the air reactor outlet by carefully regulating the air feed [97]. CLR systems also show reduced risk of coke accumulation due to their inherently regenerative cycling. Nevertheless, deactivation remains a concern in many oxide-based systems, often caused by incomplete removal of carbon deposits [98]. The use of circulating fluidized beds in CLR promotes effective gas–solid interaction and facilitates seamless particle transport between reactors. Among the various technical challenges, selecting a suitable oxygen carrier remains pivotal to optimizing system performance. Issues like carbon deposition can significantly undermine the long-term stability of oxygen carriers, posing substantial barriers to industrial deployment. In addition to deactivation, toxicity and economic considerations associated with oxygen carriers further limit their practical applicability [99].

In recent years, coal, natural gas and biomass have been explored as potential sources for Chemical Looping Reforming (CLR) applications. Although various feedstocks are viable for reforming processes, methane stands out as the preferred option for hydrogen generation due to its low cost, broad availability, high hydrogen-to-carbon ratio and reduced byproduct formation compared to alternative substrates [100]. Steam methane reforming remains the most mature and widely implemented large-scale method for hydrogen production [101].

While most CLR developments have historically focused on gaseous fuels, interest in renewable liquid fuels, particularly those derived from biomass and biofuels, has grown substantially due to sustainability concerns. Due to its abundance, high hydrogen content, safety in handling and transport and significant heating value, ethanol has emerged as a promising candidate [102]. Glycerol, another bio-derived feedstock, has also demonstrated potential in steam reforming. Its

attractiveness stems largely from its widespread availability and low cost as a by-product of biodiesel production [103].

A broad range of liquid and gaseous hydrocarbon fuels can be utilized as inputs in hydrogen production via CLR. The fuel type and its physical state significantly influence the reactor design and the nature of the oxygen carrier employed. Studies in the literature have examined the application of fluidized beds, packed beds and moving bed reactors for CLR using both liquid and gaseous fuels [104]. Additional factors, such as hydrogen purity, production cost, process control and heat transfer efficiency, are critical in determining the optimal feedstock.

Operational parameters within the fuel reactor, such as the fuel-to-steam ratio, pressure, temperature and residence time, must be carefully tailored to the feedstock. For instance, glycerol steam reforming entails a network of reactions producing intermediates that influence hydrogen yield and selectivity. The enthalpy changes associated with these reactions depend on both the fuel composition and the metal oxide used as the oxygen carrier. Impurities present in either gaseous or liquid fuels can negatively impact the oxygen carrier's performance in terms of transfer capacity, selectivity and reactivity. Hence, the careful matching of oxygen carrier material to the specific fuel is essential for maximizing fuel conversion and ensuring oxygen carrier durability [105]. A consolidated summary of CLR studies with various fuels is provided in Table 1.1.

1.2.3.1 Chemical Looping Reforming of Methane

Methane, the principal component of natural and unconventional gas reserves, represents a highly efficient and energy-conserving route for hydrogen production to meet rising global energy demands [106]. CLR bears similarities to chemical looping combustion; however, instead of complete oxidation to CO_2 and water, methane undergoes partial oxidation via a solid oxygen

carrier to produce syngas, comprising H_2 and CO, suitable for downstream conversion into high-value chemicals [107].

CLR is designed to generate H_2 + CO through the partial oxidation of methane using the lattice oxygen in a metal oxide oxygen carrier. The reduced oxygen carrier is then reoxidized in a separate air reactor [108]. The heat released during these redox cycles can be effectively harnessed to drive the endothermic steam or dry reforming of methane [109].

Typically, CLR systems include two reactors, often configured as fixed, moving, or fluidized beds. The choice of reactor setup depends on desired mass and heat transfer rates, redox kinetics and the degree of reduction needed in the oxygen carrier [110]. The specific oxygen-to-fuel ratio and the chemical nature of the oxygen carrier dictate the reforming pathways and reaction products, thereby influencing reactor design and syngas composition [110].

Partial oxidation of methane:

$$CH_4 + Me_xO_y \rightarrow 2H_2 + CO + Me_xO_{y-1}. \quad \text{(R-1)}$$

Full methane oxidation:

$$CH_4 + 4Me_xO_y \rightarrow 2H_2O + CO_2 + 4Me_xO_{y-1}. \quad \text{(R-2)}$$

Table 1.1 Summary of chemical looping reforming of various feedstocks studied in the literature.

Oxygen carrier	Reactant	Temperature (°C)	H_2 Purity	Reactant conversion	References
$CuO–Ni/Al_2O_3$	Ethanol	500–650	83%	98%–100%	[111]
NiO/Al_2O_3	Ethanol	600	97%	82%–93%	[112]
NiFe/MgAl	Ethanol	400–700	78%	100%	[113]
Ni/Al_2O_4	Ethanol	900	82%	91%	[114]
Ni/Al_2O_3	Ethanol	600–900	61%	72%	[115]
$NiO–CuO/Al_2O_3$	Ethanol	100–900	N.A.	N.A.	[116]
LaSrNiO	Ethanol	650	75%–83%	80%–85%	[117]
CeNi/SBA	Ethanol	200–900	90%–95%	100%	[118]
$NiFe_2O_4$	Ethanol	450	70%–80%	100%	[119]
Ni/CeO_2	Ethanol	200–800	N.A.	88%	[120]
$NiMn_2O_4$	Ethanol	500–800	N.A.	N.A.	[121]

$LaNiO_3$/MMT	Ethanol	650	70%–80%	87%	[122]
Ni/CeO_2	Ethanol	100–600	88%	80%	[123]
NiO/Al_2O_3	Ethanol	850–950	62%	100%	[101]
NiO/MMT	Ethanol	550	60%–70%	70%–80%	[124]
Ir/La_2O_3	Ethanol	400–850	90%–100%	N.A.	[125]
Ni–Ca/Al_2O_3	Ethanol	550–650	N.A.	99%	[126]
Ce–Ni/Fe	Glycerol	200–800	80%–90%	60%–80%	[127]
CeNiO	Glycerol	500–650	85%	60%	[115]
Rh/Al_2O_3	Glycerol	550–700	N.A.	93%–100%	[128]
NiO	Glycerol	750–850	60%	100%	[129]
Fe–Ce–Ni	Glycerol	600–800	80.6%	70%–100%	[130]
Rh/UGSO	Glycerol	650	N.A.	94%–100%	[131]
Ni–Mg/ATP	Glycerol	400–800	94.7%	87.9%	[132]
Ni/Al_2O_3	Glycerol	600–750	N.A.	65%–95%	[133]
Ni/ZrO_2	Glycerol	650	94%	99%	[134]
Rh–Mg/Al_2O_4	Glycerol	300–600	76%	99.6%	[135]
Ni–Co–Cu/Al_2O_3	Glycerol	400–750	65%	80%–95%	[136]
Ce–Ni/PSNT	Glycerol	650	70%–90%	88%	[137]
Ni/Al_2O_3	Glycerol	500–600	80%–95%	N.A.	[138]
Ni/Al_2O_3	Glycerol	550	87.9%	85%–98%	[103]
Ni/Al_2O_3	Glycerol	450–600	93%	99%	[139]
N.A.	Glycerol	350–700	45%–55%	90%–96%	[140]
Rh–CeO_2/Al_2O_3	Glycerol	400–750	78%	90%	[141]
Ni/Al_2O_3	Glycerol	450–650	N.A.	100%	[142]
Ni–Cu–Al	Glycerol	450–650	92.9	90.9%	[143]
Ni/Al_2O_3	Glycerol	400–700	97%	100%	[144]
Ni/Al_2O_3	Glycerol	600–700	65%	50%	[145]
$LaSrFeO_3$	Methane	850	N.A.	85%–88%	[146]
LaSrMnCoO	Methane	850	65%	40%–78%	[106]
$CeFeO_3$	Methane	650–850	80%–85%	70%–80%	[147]
Fe_2O_3/$MgAl_2O_4$	Methane	900	91%–100%	83%–92%	[148]
NiO/$CeZrO_4$	Methane	700	N.A.	52.8%	[149]
Ni/Fe	Methane	800	93%	96%	[150]
Ni–CeO2/MgO	Methane	550–700	N.A.	45%	[151]
Ni–Cu	Methane	800	70%–80%	30%	[152]
NiO	Methane	650	75%–80%	80%–87%	[153]
Ni–CeO2/Al2O3	Methane	700	N.A.	95%	[154]
Ni/CeO2-IMP	Methane	800	N.A.	90%	[155]
Cu–Ni–Mn	Methane	650	N.A.	99.4%	[156]
$LaFe_2O_3$/Al_2O_3	Methane	800–900	N.A.	55%	[157]
Fe_2O_3/Al_2O_3	Methane	700–900	96%	98%	[158]
$LaSrFeO_6$	Methane	500–900	50%–60%	70%–85%	[159]
$Ce_{0.5}Fe_{0.5}O_2$	Methane	800–900	92%	90%–98%	[160]
$LaFe_{0.7}Co_{0.3}O_3$	Methane	500–700	50%	85%	[161]
Fe/Al_2O_3	Methane	600–800	55%	99%	[162]
NiO	Methane	600–900	>50%	92%	[163]
NiO/$CaAl_2O_3$	Methane	400–900	N.A.	99%	[164]
17%Ni/Al_2O_3	Methane	600–750	60%	40%	[165]
NiO	Methane	450–650	N.A.	90%	[166]
Ni–Ce	Methane	600–800	N.A.	50%–61%	[167]

Methane decomposition:

$$CH_4 \rightarrow C + 2H_2 \quad \text{(R-3)}$$

Water-gas shift:

$$CO + H_2O \rightarrow CO_2 + H_2 \quad \text{(R-4)}$$

Steam methane reforming:

$$CH_4 + H_2O \rightarrow CO + 3H_2 \quad \text{(R-5)}$$

Dry methane reforming:

$$CH_4 + CO_2 \rightarrow 2CO + 2H_2 \quad \text{(R-6)}$$

From a selectivity standpoint, methane reduction can yield a variety of products depending on the reaction pathway. While Fe-based oxygen carriers are appealing due to their environmental friendliness, cost-effectiveness and favorable thermodynamics, pure iron oxides are insufficient for methane reforming, particularly with respect to CH_4 conversion and H_2 selectivity [168]. Consequently, a significant reduction to FeO or metallic Fe is required to effectively generate hydrogen. However, Fe exhibits relatively low reactivity toward methane compared to other transition metals [155]. To address this, many studies have investigated the incorporation of promoters to improve Fe-based material performance.

In chemical looping reforming (CLR) of methane at 900 °C, Fe-based carriers achieved 84% CH_4 conversion, while Fe–Ni, Fe–Co and Fe–Cu demonstrated higher conversions of 92%, 83% and 85%, respectively. This suggests that methane decomposition, rather than oxidation via lattice oxygen, contributes to elevated conversion rates. Promoters have also been shown to enhance hydrogen purity: following ten cycles, the H_2 purity reached 91% for Fe, 94% for Fe–Ni, 98% for

Fe–Cu and 100% for Fe–Co. Co was found to increase the quantity of active lattice oxygen, while Cu facilitates initial reduction but inhibits full reduction. Ni displayed the strongest interaction with Fe and even minimal additions improved the extent of deep reduction. Thus, Ni, Co and Cu enhance H_2 purity and H_2–CO yield, although they reduce CO purity due to improved oxygen mobility [148].

Compared to steam methane reforming (SMR), the reaction rate for partial oxidation of methane (POM) is significantly faster, by several orders of magnitude. Additionally, the methane reforming process is highly temperature-sensitive in the 500–700 °C range [149]. Qin et al. [169] demonstrated that doping Fe-based carriers with 1% Cu increases low-temperature reactivity, resulting in a 47% higher CH_4 conversion rate for Cu–Fe_2O_3 compared to Fe_2O_3 at 700 °C, with up to 35% energy savings.

A detailed examination of the influence of steam-to-oxygen carrier and methane-to-oxygen carrier ratios on CH_4 conversion and product yields in SMR has been conducted by several researchers [150]. It was observed that increasing the steam-to-carrier ratio lowers H_2 concentration while CO_2 and CO levels rise. This occurs because high steam concentrations suppress the complete oxidation of CH_4, leading to its transformation into CO_2 and H_2 and sometimes into carbon and H_2. CaO in the system captures CO_2 to form $CaCO_3$, resulting in only a modest rise in CO_2 concentration with more steam. Furthermore, excessive steam promotes carbon oxidation to CO, reducing H_2 levels while CH_4 and CO concentrations increase.

Higher steam ratios also result in less carbon deposition and lower CH_4 conversion during reforming, as H_2O reacts with deposited carbon to form CO and H_2, reducing carbon build-up. Moreover, increasing the methane-to-oxygen carrier ratio reduces both methane conversion and hydrogen yield, as the oxygen carrier lacks sufficient active sites to process the excess methane

[150]. In comparison with SMR and POM, dry reforming of methane (DRM) achieves a H_2/CO ratio near unity, favoring the synthesis of oxygenated compounds and hydrocarbons [170]. Due to the endothermic nature of DRM, increasing temperature up to 800 °C results in an H_2/CO ratio approaching 1 [171]. The reverse water-gas shift reaction and the CO_2/CH_4 feed ratio significantly influence DRM behavior in the absence of O_2. According to Chein and Fung [172], a higher CO_2/CH_4 ratio increases methane conversion but reduces hydrogen yield.

The steam-to-carbon ratio is another critical parameter in determining CH_4 conversion and product distribution during CLR. Excess steam is undesirable due to higher operational costs and reduced energy efficiency, so an optimized ratio is necessary. The impact of steam/carbon ratios on conversion rates, selectivity and syngas composition has been evaluated by Nazari et al. [156], as illustrated in Figure 1.12.

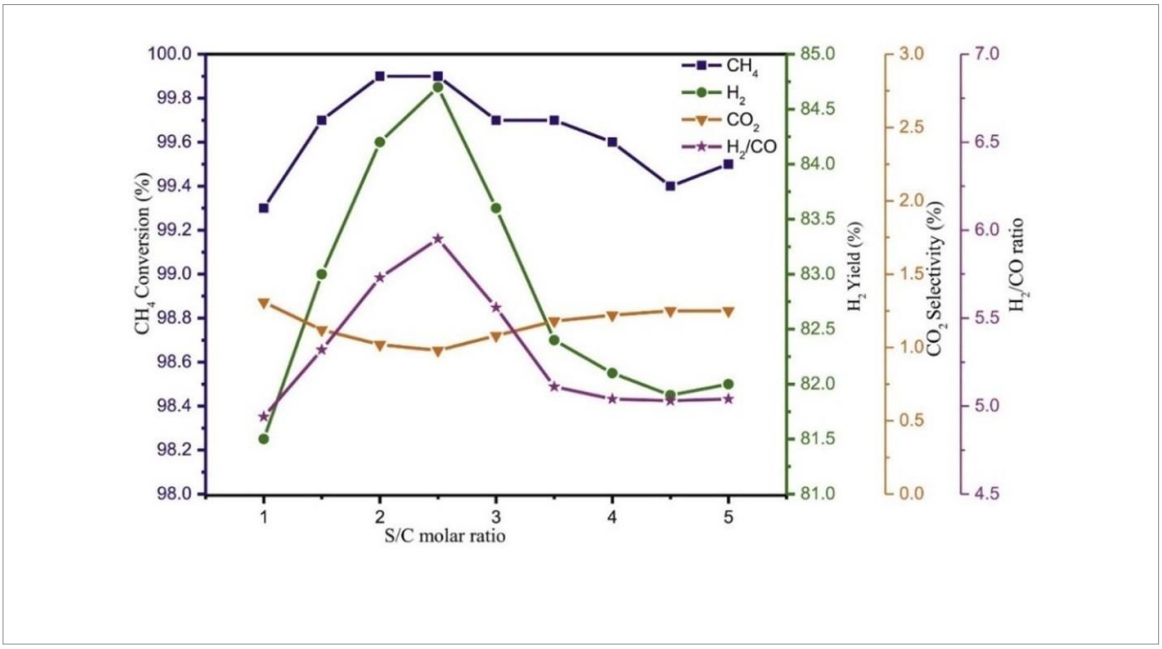

Figure 1.12 Methane conversion, hydrogen production, CO_2 selectivity and H_2/CO ratio at 650 °C depending on the Steam-to-Carbon molar ratio. Adapted from Nazari et al. [156]

Increasing the bed height in the fuel reactor improves CH_4 reforming performance in fluidized bed systems due to extended residence times, which support oxidation of surface carbides formed from CH_4 dissociation [157]. Iglesias et al. [167], investigated temperature effects and found that higher temperatures favor CO selectivity by enhancing bulk oxygen mobility. Additionally, CH_4 conversion and H_2 yields rise with increasing temperature. Compared to $NiO/NiAl_2O_4$, $NiO/MgAl_2O_4$ demonstrated superior CH_4 reforming activity, higher conversion and greater resistance to carbon formation in fluidized beds at 950 °C [173].

Operating pressure is another significant factor affecting product distribution in CLR. Both CO_2 and CH_4 conversions decrease as pressure increases from 1 to 25 bar. Therefore, atmospheric pressure is recommended for effective CO_2 reforming and syngas production [174]. Pressure also promotes carbon deposition. Nevertheless, Spallina et al. [163], evaluated CLR under high-pressure conditions (~20 bar) with integrated CO_2 capture, achieving 92% CH_4 conversion and nearly zero CO_2 emissions. Their results confirmed that combining chemical looping combustion and steam reforming is feasible through controlled thermal cycling. Argyris et al. [164], demonstrated that in packed bed reactors, higher pressure enhances solid conversion, particularly under low-velocity operating conditions.

1.2.4 Calcium looping

Industrial activities, especially the burning of fossil fuels, are widely acknowledged as the main contributors to climate change due to the substantial emission of carbon dioxide (CO_2) [6]. In light of this, the advancement of efficient technologies for capturing and storing CO_2 has become a critical area of research. Among the various capture strategies, calcium looping stands out as a promising method due to its favorable cost and energy efficiency [175]. This technology can also be synergistically combined with approaches like chemical looping combustion (CLC) and oxy-fuel combustion to further improve CO_2 capture rates [176]. Moreover, integration with renewable

systems such as concentrated solar power (CSP) makes calcium looping an attractive pathway for achieving carbon-neutral energy generation [177].

As shown in Figure 1.13, the calcium looping cycle is based on a reversible chemical reaction where a metal oxide reacts with CO_2 to form a metal carbonate. This carbonate is then thermally decomposed to release CO_2 and regenerate the metal oxide, allowing for continuous operation. The generalized reactions for a divalent metal carbonate are provided in equations (1.12) and (1.13):

$$MeO\ (s) + CO_2\ (g) \rightarrow MeCO_3\ (s) \quad (1.12)$$

$$MeCO_3\ (s) \rightarrow MeO\ (s) + CO_2\ (g) \quad (1.13)$$

Naturally occurring minerals such as limestone and dolomite have been extensively employed in calcium looping due to their low cost, high reactivity and widespread availability [178]. However, the use of synthetic oxides, including non-calcium-based compounds, has enabled further refinement of the operational conditions (temperature and pressure), enhancing the efficiency of CO_2 capture across various processes such as sorbent-enhanced reforming [179, 180]. In post-combustion applications, calcium looping can be integrated with power generation facilities that utilize coal, natural gas, or biomass.

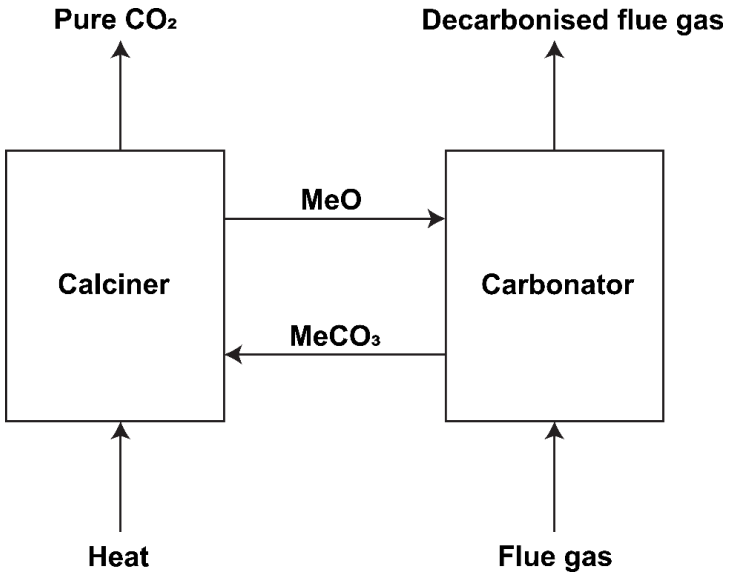

Figure 1.13 Schematic illustration of calcium looping using a metal carbonate.

Research has explored a broad spectrum of synthetic oxides for calcium looping, encompassing monometallic, doped and mixed metal oxides. CaO and MgO are among the most widely studied sorbents [181, 182], primarily due to the economic and practical advantages of using naturally sourced materials like limestone and magnesite. The cost of CO_2 capture via calcium looping, under some specific circumstances, has been shown to be competitive with conventional amine-based systems [183].

$$CaO\ (s) + CO_2\ (g) \leftrightarrow CaCO_3\ (s), \quad \Delta H_{298} = -178\ kJ/mol \tag{1.14}$$

$$MgO\ (s) + CO_2\ (g) \leftrightarrow MgCO_3\ (s), \quad \Delta H_{298} = -118\ kJ/mol \tag{1.15}$$

Numerous studies have focused on synthesizing, characterizing and evaluating CaO- and MgO-based sorbents for CO_2 capture. For example, Wang et al. [184] reviewed the effects of synthesis methods, dopants and support materials on the carbonation performance and durability of CaO-based sorbents. The kinetics of the carbonation process are heavily influenced by diffusion barriers during the rapid reaction phase. Nonetheless, overall CO_2 uptake depends on both the fast and slow carbonation stages. Consequently, in laboratory-scale systems, sorbent particle size has shown minimal effect, whereas the number of calcination-carbonation cycles plays a more critical role in

determining sorption performance [185]. Li et al. [186] reported that introducing steam enhances the decomposition rate of $CaCO_3$, thereby improving the CO_2 capture performance of CaO.

The work of Manovic et al. [187] revealed that increasing the calcination temperature and CO_2 concentration positively affects the CO_2 uptake of CaO. For MgO-based materials, Heo and Park [188] studied a novel synthesis technique, noting that morphological and pore structure variations significantly influence CO_2 adsorption capacity.

Despite significant advancements, CaO and MgO still present challenges related to thermal stability and deactivation at elevated temperatures [189]. These issues stem from sintering-induced loss of surface area and porosity, as $CaCO_3$'s Tammann temperature (~529 °C) lies below the operating range of the carbonation (600–700 °C) and calcination (900–950 °C) processes [190]. These limitations can be mitigated through the use of doped or supported sorbents, albeit with increased synthesis complexity and cost.

Emerging synthetic strategies, including the use of nanostructured supports, incorporation of transition metal dopants and fabrication of composite materials, offer promising avenues to enhance the physicochemical characteristics of sorbents. Doping can improve both the reactivity and durability of CaO, facilitating greater CO_2 uptake and reduced regeneration temperatures. Luo et al. [191] demonstrated that CaO doped with La_2O_3 exhibited superior carbonation conversion and cyclic stability compared to undoped $CaCO_3$, attributed to inhibited sintering and the preservation of surface area and pore structure. While dopants such as Sr, Al and Mg have also been investigated for CaO enhancement, findings regarding their efficacy remain mixed [192]. For MgO-based materials, doping with alkali metal carbonates or nitrates has proven effective in improving both capture capacity and thermal stability [193, 194]. The success of these modifications largely depends on dopant type, concentration and process conditions.

Mixed metal oxides (MMOs) composed of multiple metal constituents can exhibit synergistic effects that improve CO_2 uptake and long-term stability. Additives such as alumina (Al_2O_3), silica (SiO_2) and zirconia (ZrO_2) are often used to support CaO, enhancing sorption characteristics. Soleimanisalim et al. [195] compared uncoated and Zr/Si-coated CaO sorbents, reporting improved cyclic stability and capture performance with the coated variants. Such supports inhibit sintering and lower intraparticle diffusion resistance, thereby accelerating CO_2 capture. In integrated systems combining chemical looping and calcium looping, Al_2O_3 and MgO have served as stabilizers in CaO/CuO composites, yielding improved cyclic performance due to the formation of mixed calcium-aluminium oxides [196].

Beyond CaO and MgO systems, other metal oxide-based sorbents, particularly MMOs, have gained interest for CO_2 capture applications [197–199]. These materials offer tunable chemical properties, allowing for optimization of selectivity, capacity and durability. Recently, ternary metal oxides have attracted growing attention as calcium looping candidates [200], owing to their complex crystal structures and diverse coordination environments [201; 202, 203]. A notable class of ternary oxides is the perovskite family (general formula ABO_3), characterized by slightly distorted cubic structures. Perovskite materials have been explored for CO_2 capture in industries such as cement, steel and power generation. For example, $CaSiO_3$, a perovskite-based material, has demonstrated reversible CO_2 absorption at temperatures as low as 400 °C, with water content playing a facilitating role [204]. Sr_2CeO_4 sorbents have shown high capacities of up to 0.25 g CO_2/g sorbent [205]. Additional ternary oxides like Ca_2SiO_4, Li_4SiO_4, Li_2ZrO_3, Na_2ZrO_3 and $CaFeO_{2.5}$ have also been evaluated for CO_2 capture [202, 203, 206–208]. Compared to simpler oxides, ternary systems typically offer better structural and thermal stability over multiple cycles, with resistance to sintering and structural degradation [189]. Their robustness also allows substitutional doping at A and B sites, enabling extensive customization for optimal performance.

In conclusion, ternary metal oxides represent a promising class of materials for CO_2 capture and storage due to their high capacity, cycle durability and adaptability to diverse industrial conditions. However, further studies are necessary to refine their properties for faster kinetics, enhanced regeneration and long-term operational viability before they can be deployed at commercial scales.

1.2.5 Coupling chemical looping technologies with power cycles

To date, chemical looping combustion technologies, namely chemical looping combustion (CLC) and chemical looping with oxygen uncoupling (CLOU), have primarily been developed with the objective of substituting the combustor in conventional power generation systems, such as the steam Rankine cycle, with CLC systems. As a result, the design and operational parameters of CLC and CLOU have been optimized to align with the requirements of traditional steam Rankine cycles. However, the advent of advanced power generation methods, including supercritical steam cycles and the Allam cycle, introduces new thermodynamic frameworks characterized by enhanced efficiency and greater process integration. In light of the growing prominence of these next-generation cycles, it becomes essential to re-evaluate the potential of chemical looping technologies when adapted to operate within these emerging power generation paradigms.

1.2.5.1 Advanced Thermal Power Cycle Technologies

Thermal power cycles play a central role in energy generation by transforming heat into mechanical work and subsequently into electricity. Among these, the steam Rankine cycle is the most prevalent, as illustrated in Figure 1.14, because of water's favorable characteristics, such as its high density in liquid form, widespread availability and thermodynamic suitability [209]. In this process, subcooled liquid water undergoes progressive heating until it becomes superheated steam, which then powers a turbine to generate mechanical and electrical energy. The steam is subsequently condensed into liquid and recirculated to the heat source, completing the loop.

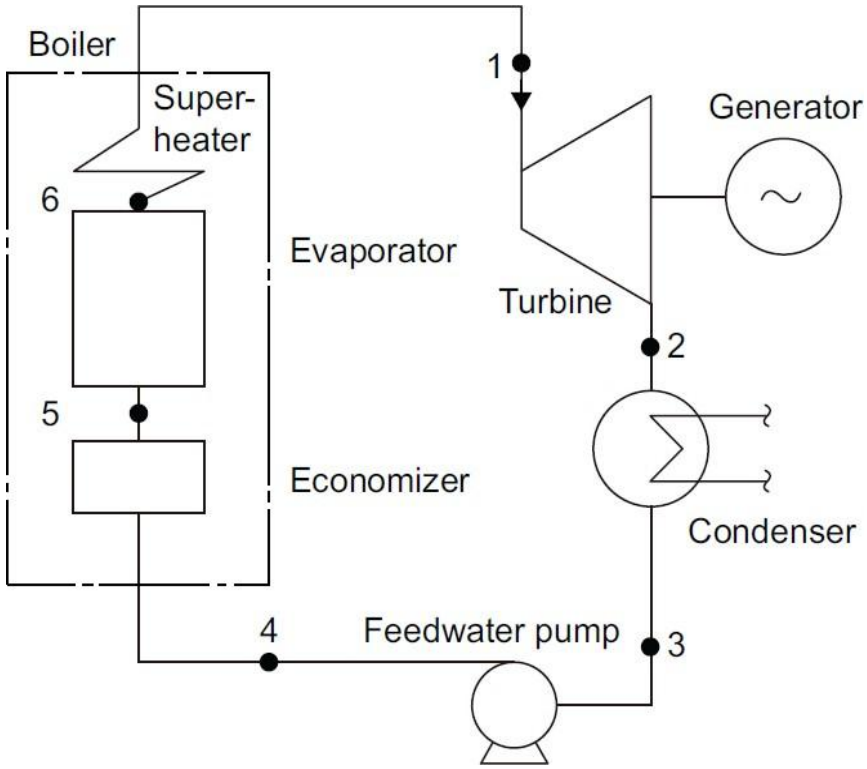

Figure 1.14 Schematic layout of a steam Rankine cycle system [210].

The T–s and h–s diagrams representing the steam Rankine cycle are illustrated in Figure 1.15. In these diagrams, *T* denotes the absolute temperature, *h* the specific enthalpy and *s* the specific entropy. The cycle begins with steam entering the turbine in a superheated state, identified as point 1. An adiabatic expansion then takes place within the turbine, resulting in a mixture of steam and water, commonly referred to as wet steam, at the turbine exit, which also serves as the condenser inlet, denoted as point 2.

Following this, the working fluid is condensed within the condenser. The outlet of the condenser, corresponding to the boiler feed pump inlet, is represented by point 3. At this stage, the fluid undergoes adiabatic compression in the boiler feed-water pump to reach the pressure required at the boiler inlet. Upon exiting the pump (point 4), the fluid is in the form of compressed liquid. It then proceeds through a heating phase at constant pressure until it reaches saturated liquid conditions in the boiler, indicated as point 5.

Within the boiler evaporator, the fluid experiences a phase change through evaporation at constant pressure, becoming saturated vapour at point 6. In the final stage, this saturated vapour is superheated in the boiler's superheater, completing the cycle as it returns to point 1.

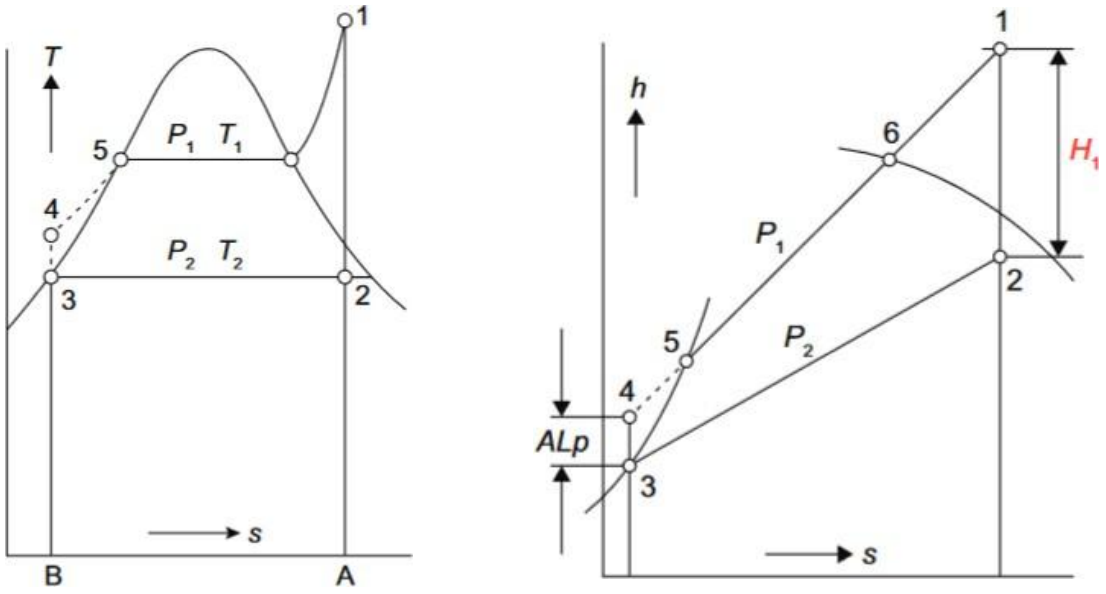

Figure 1.15 T-s diagram (left) and h-s diagram (right) of a steam Rankine cycle [210].

The theoretical upper limit of the efficiency of the Rankine cycle is constrained by the difference in temperatures between the heat source and the heat sink. In practice, the efficiency of the steam Rankine cycle is influenced by a range of factors, including steam quality, pressure and temperature levels within the cycle, as well as the design of the process components such as the boiler, turbine and condenser. At present, the most advanced coal-fired power plants are capable of attaining a state-of-the-art efficiency of approximately 47.5%, with superheated steam at 30 MPa [211].

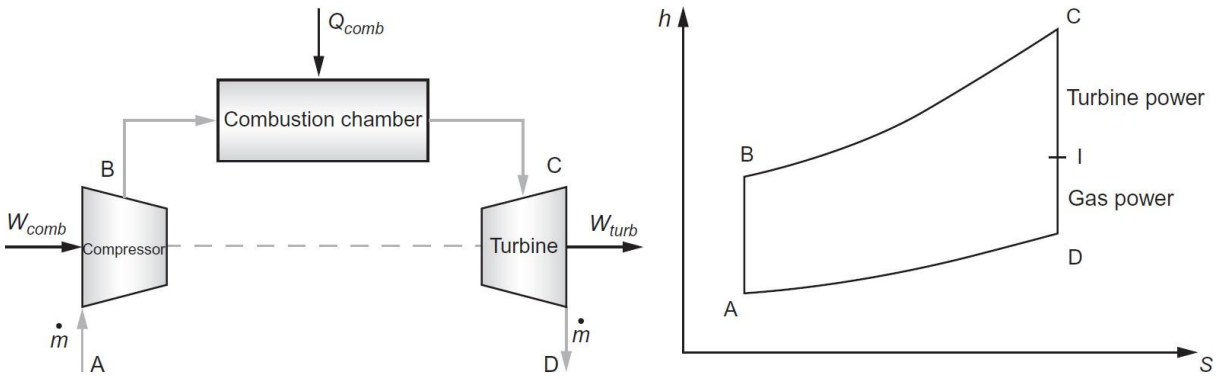

Figure 1.16 (Left) Schematic overview of the Brayton cycle; (Right) enthalpy-entropy (h-s) diagram illustrating the Brayton cycle [212].

The Brayton cycle is commonly used in gas turbines and some internal combustion engines, where air is compressed, mixed with the fuel and burned to produce high-temperature gases that drive the turbine. The process of the Brayton cycle involves several steps, as shown in Figure 1.16 [212]. First, air is compressed isentropically through the compressor from point A to point B. After that, the compressed air is mixed with fuel in the combustion chamber, resulting in the production of heat and hot combustion products from point B to point C. Next, the high-pressure and high-temperature exhaust gases undergo expansion in the turbine (point C to point D), generating thrust and/or motor shaft rotation. To calculate the efficiency of the cycle, the net power output (point I to point D, also known as the gas power) is calculated by subtracting the power output of the turbine (CD) from the power consumption of the compressor (AB = CI).

Similar to the Rankine cycle, the Brayton cycle's state of the art efficiency also varies depending on the specific configuration and operating conditions of the cycle. The maximum theoretical efficiency of the Brayton cycle is limited by the ratio of the compressor exit temperature to the turbine inlet temperature, as well as the pressure ratio. In practice, the efficiency of the Brayton cycle can be influenced by factors such as the design of the turbine and compressor, the combustion

process and the heat exchanger efficiency. Currently, the state-of-the-art efficiency of a combined-cycle gas turbine powerplant, which couples the Brayton cycle with the Rankine cycle, is slightly short of 60% [213], which could be achieved in some of the most advanced natural gas-fired power plants in operation. Other advanced gas turbine technologies, such as the Brayton cycle with intercooling and reheat, or the Brayton cycle with recuperation and intercooling, could potentially achieve higher efficiencies.

1.3 Purpose and Structural Overview of the Thesis

Given the increasing relevance of low-carbon energy solutions, chemical looping technologies have emerged as a promising class of processes for sustainable energy conversion, carbon capture and renewable fuel production. These systems enable efficient thermochemical transformations by utilizing solid oxygen carriers that undergo cyclic redox reactions to drive processes such as combustion, gasification and methanation. To fully harness the potential of chemical looping technologies, however, several critical challenges must be addressed through rigorous process modelling, innovative process integration and the development of robust reactor configurations.

This Thesis is concerned with advancing the understanding, design and optimizations of chemical looping systems for both energy generation and long-term energy storage.

A brief overview of the Thesis structure is provided below.

1. Chapter 1 introduces the background and motivation for carbon capture and chemical looping technologies, highlighting their importance in the context of sustainable energy conversion and storage.
2. Chapter 2 describes the modelling methodologies and simulation tools employed in this work.
3. Chapter 3 presents the development and numerical analysis of a two-stage CLC fixed-bed reactor network for methane combustion. The system combines Cu- and Ni-based oxygen carriers to enhance process efficiency and reduce the number of reactor units required.

4. Chapter 4 explores an innovative integrated process combining chemical looping gasification of biomass and plastic waste with renewable hydrogen from electrolysis for synthetic methane production. The proposed layout is evaluated for its potential as a long-term renewable energy storage solution.
5. Chapter 5 focuses on the modelling and optimization of the methanation process, analyzing the influence of feed composition and recycle ratios on reactor performance. The aim is to establish design guidelines for industrial-scale SNG production from biomass-derived syngas.
6. Chapter 6 summarizes the main conclusions drawn from the research and outlines possible future research directions to further advance chemical looping technologies.

It is important to highlight that Chapters 4 and 5 are thematically connected and should be interpreted as two complementary contributions within the broader topic of chemical looping processes for methane production. While Chapter 4 deals with the coupling of solar-derived hydrogen with Chemical Looping Gasification (CLG), Chapter 5 focuses on the parametric evaluation of CO_2 methanation integrated with Chemical Looping Gasification (CLG). Despite being presented separately to preserve the structure and integrity of two independent research works, the chapters are intrinsically linked. Moreover, the Chemical Looping Gasification process is described in detail in Chapter 4, together with the key modelling assumptions underlying its implementation, ensuring consistency and continuity across both studies

Chapter 2 Process Simulation Methodology

2.1 Introduction

The development and assessment of chemical looping technologies for combustion, gasification, and methanation processes require robust modeling approaches capable of addressing both equilibrium and kinetic aspects. Accurate simulation frameworks are essential not only to predict reactor performance under steady-state and dynamic conditions but also to provide guidelines for scale-up and industrial deployment.

This chapter presents a critical overview of the modeling methodologies employed in this thesis, including equilibrium-based methods, one-dimensional fixed-bed formulations, pseudo-homogeneous approaches, and detailed heterogeneous reactor models. The rationale behind adopting multiple levels of modeling complexity is to exploit the strengths of each method while mitigating their intrinsic limitations through cross-validation.

2.2 Modelling approach

When modelling and optimising a chemical process, several critical factors must be taken into account, including the selection of design parameters, thermodynamic models, foundational assumptions, operational conditions and performance metrics. Each element requires careful justification and deliberate choice. Moreover, it is essential to incorporate the detailed characteristics and parameters specific to the process under study, such as the design basis and fuel compositions, which are discussed extensively in the dedicated results chapters of this Thesis, namely Chapters 3, 4 and 5. Adopting a thorough and methodical approach to process design enables enhancements in performance and efficiency while concurrently minimizing costs and environmental footprint.

2.2.1 Thermodynamic Equilibrium Models

Thermodynamic equilibrium models, based on the principle of Gibbs free energy minimization, represent a fundamental approach for modeling chemical looping systems. At constant temperature and pressure, a chemical system reaches a stable state when its total Gibbs free energy is minimized. Solving this optimization problem allows equilibrium models to predict the theoretical distribution of products in the absence of kinetic or transport limitations.

These models have been widely applied in Chemical Looping Combustion (CLC), Chemical Looping Gasification (CLG), and Chemical Looping Reforming (CLR). They are particularly useful for establishing the maximum achievable conversion efficiencies, predicting syngas composition and H_2/CO ratios, which are critical for downstream processes such as methanation or Fischer–Tropsch synthesis, and performing rapid process screening across a broad range of operating conditions, including temperature, pressure, and feedstock composition. Furthermore, equilibrium models provide essential benchmark references for evaluating the performance of more complex kinetic or heterogeneous reactor models.

The main advantages of thermodynamic equilibrium modeling lie in its computational efficiency, broad applicability, and ability to define theoretical performance limits. These models are particularly valuable in guiding the initial stages of process design, identifying promising operating windows, and supporting pre-screening for integrated process configurations. However, they also have inherent limitations. By neglecting reaction kinetics and transient phenomena, they cannot capture time-dependent behavior, ignition or extinction events, or incomplete conversions. Idealized assumptions may lead to overestimated efficiencies, as factors such as diffusion limitations, catalyst deactivation, and non-ideal transport effects are not considered. Additionally, the reliability of predictions depends heavily on the completeness and accuracy of the underlying thermodynamic databases, especially in complex gas–solid systems.

Recent studies illustrate the continued relevance of equilibrium modeling in chemical looping research. Qi et al. [214] applied Gibbs free energy minimization to a process combining CLG with steam reforming (CLG–SR), showing that the integration improves thermal efficiency, enhances syngas quality, and simplifies system design through process intensification. Similarly, López van der Horst et al. [215] examined CLR with various oxygen carriers (WO_3, $MnWO_4$, $NiWO_4$), demonstrating that certain carriers achieve complete conversion at lower temperatures and that hydrogen yields can approach 98% under stoichiometric conditions. Their work also highlighted the importance of adjusting fuel-to-carrier ratios and oxidation conditions to achieve autothermal operation.

Equilibrium modeling has also been extended to reactor-scale simulations, where Gibbs energy minimization is coupled with flow and transport constraints. This hybrid approach bridges the gap between theoretical predictions and practical reactor design, supporting scale-up studies for CLC and CLG systems. Cai et al. [216] used an equilibrium-based model to study calcium looping gasification of municipal solid waste, identifying optimal sorbents and operating conditions to maximize hydrogen-rich syngas production while maintaining process stability and CO_2 capture. Their analysis further illustrated trade-offs between efficiency, autothermal feasibility, and system self-sufficiency, emphasizing the practical insights equilibrium models can provide in waste-to-energy applications.

A recent study by Abdalla et al. [217] investigated a copper-based chemical looping air separation (CLAS) process, integrating thermodynamic analysis, kinetic modeling, and fluidized bed simulations. Using both bubbling and circulating fluidization regimes, the study evaluated oxygen generation performance under various temperature and flow conditions. This work highlights the importance of combining thermodynamic equilibrium predictions with kinetic and reactor-scale simulations, providing a comprehensive understanding of process behavior and guiding optimization for practical implementations.

In summary, thermodynamic equilibrium models serve as the foundational layer in the multi-scale modeling hierarchy of chemical looping systems. While they cannot replace kinetic or transport-based approaches, their ability to define performance boundaries, guide material selection, and identify promising operating windows makes them indispensable in the early stages of process design, optimization, and techno-economic evaluation.

2.2.2 One-Dimensional Fixed-Bed Reactor Models

A packed bed catalytic reactor consists of typically uniform catalytic particles that are randomly packed and securely held within a vessel or tube, allowing the bulk fluid to flow through the interstitial voids. Reactants are transported from the bulk fluid to the catalyst surface and then diffuse through the catalyst pores, where adsorption occurs on the pore surfaces followed by chemical transformation. The resulting products desorb and are carried back into the bulk fluid. The convective movement of the bulk fluid is coupled with both heat and mass transfer processes, and dispersion effects arise primarily from the complex flow patterns induced by the packed structure. Additional contributions to dispersion come from molecular diffusion, thermal conduction in the fluid and solid phases, and radiation. In many cases, chemical reactions involve either the release or absorption of heat, which, when significant, must be exchanged with the surroundings via the reactor walls.

The first documented commercial use of a packed bed reactor dates back to 1831, when Peregrine Philips, a British vinegar manufacturer, patented a process to produce sulfur trioxide by passing air and sulfur dioxide over a heated bed of platinum sponge. Because the catalyst was not consumed, it could be reused continuously, with reactants flowing over the bed without the need for separation or recycling of the catalyst.

Since then, packed bed catalytic reactors have become among the most widely employed units for gas–solid and liquid–solid reactions. Although newer reactor types, such as fluidized beds, exist, packed bed reactors remain extensively used for large-scale processes in the petroleum industry,

including catalytic reforming and hydro-treatment, as well as in basic chemical production, such as ammonia and sulfuric acid synthesis. Within these reactors, a variety of physical and chemical phenomena occur as reactant-containing fluids flow through the packed bed.

Due to the intricate interplay of physical and chemical processes, a detailed and exact description of packed bed reactors is often impractical or leads to highly complex mathematical formulations. More detailed models require numerous parameters, many of which cannot be independently measured, leaving only effective parameters available for estimation. Consequently, overly detailed models frequently suffer from a lack of reliable parameter values. In practice, simplified models that capture the key phenomena are preferred. The choice of model depends on the specific system, the properties of interest, the availability of parameters, and the feasibility of numerical solutions.

Several modeling approaches exist for packed bed reactors. The most commonly used are continuum models, which treat the heterogeneous system as a one- or multi-phase continuum, resulting in differential-algebraic equations describing bulk fluid and solid phase variables [218-221]. Another approach considers each catalyst pellet with its surrounding bulk fluid as a reactor unit or cell, which interacts with neighboring cells to form a network [220,222-224]. The transport processes included in the model determine the nature of the interaction between cells. A third class, often termed channel models, incorporates measured variations in void fraction (porosity) along the reactor cross-section. Here, porosity is maximal near the wall and decreases toward the tube axis in an oscillatory manner over 1–2 particle diameters. At approximately 4–5 particle diameters from the wall, its influence diminishes. Channel models divide the reactor into coaxial annular channels, each considered as a plug flow reactor with velocity determined by the average porosity, exchanging heat and mass with neighboring channels. Channel models thus generalize classical continuum models, inheriting both their advantages and limitations, though they remain less used due to limited engineering data.

Despite differences among modeling approaches, continuum models dominate packed bed reactor analysis and optimization. This prevalence is partly because mass and heat transfer experiments have historically been interpreted within the continuum framework, providing directly applicable parameter values. Moreover, nonlinear reaction rates are sometimes more tractable within differential equations than algebraic formulations, though modern numerical methods for nonlinear differential equations also employ techniques used for nonlinear algebraic systems. Accordingly, the present work emphasizes continuum modeling and its numerical treatment.

The following section introduces a classification of continuum models for packed bed reactors.

2.3 Continuum models

To accurately simulate a packed bed reactor, it is essential to define suitable reaction rate expressions and to model the transport phenomena occurring within the catalyst pellets, the bulk fluid, and at their interfaces. These transport processes can generally be grouped into several categories: intraparticle diffusion of both heat and mass, heat and mass exchange between the catalyst pellet and the bulk fluid, convective transport of the fluid, dispersion of heat and mass in the fluid phase, thermal conduction through the solid phase, and heat transfer to the surrounding reactor walls.

The level of detail in a reactor model depends on the assumptions made and on how these various phenomena are represented mathematically. Following the widely accepted classification by Froment and Bischoff [221] continuum models are commonly divided into two principal types: pseudo-homogeneous and heterogeneous models. In pseudo-homogeneous models, the catalyst surface is assumed to be fully exposed to the bulk fluid, implying that no resistances to heat or mass transfer exist between the fluid and the particles. In contrast, heterogeneous models treat the solid and fluid phases separately, solving conservation equations for each phase independently. A general schematic classification of continuum models is provided in Table 2.1.

Beyond the basic frameworks summarized in Table 2.1, numerous modifications and hybrid approaches are possible. For example, it is common to include dispersion effects in the energy balance while neglecting them in mass balances, to associate axial dispersion with either the fluid phase, the solid phase, or both, to account only for intraparticle mass diffusion under isothermal pellet conditions, or to consider solely the interfacial resistance in heat transfer. These variations allow modelers to tailor the level of complexity to the specific system and phenomena of interest.

Table 2.1. Classification of classical continuum models

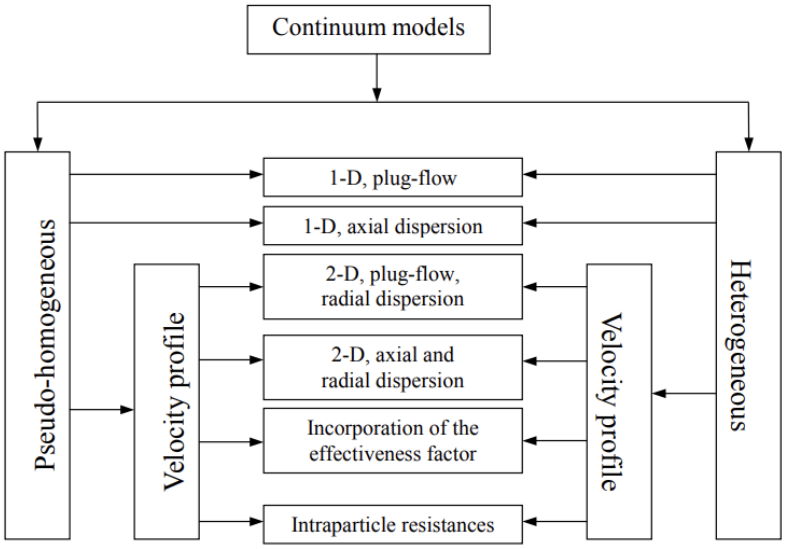

2.3.1 One-dimensional pseudo-homogeneous model

The simplest pseudo-homogeneous formulation considers only the axial profiles of radially averaged concentrations and temperatures. As convection is the only transport mechanism accounted for, this formulation is equivalent to a plug-flow representation. Furthermore, the fluid physical properties are assumed to be constant and uniform in the radial direction. Under steady-state conditions, the corresponding mass and energy conservation equations are therefore expressed as:

$$u_s \frac{dCi}{dz} = -R_i(C,T) \quad (2.1)$$

$$u_s \rho_f c_p \frac{dT}{dz} = R_T(C,T) - \frac{4U_w}{dt}(T - T_w) \quad (2.2)$$

where U_w represents the overall heat transfer coefficient. Similar to other heat and mass transfer coefficients used in more advanced continuum models, it is treated as an effective parameter and is typically obtained from semi-empirical or empirical correlations. The reliability of these correlations plays a decisive role in determining the predictive accuracy of packed bed reactor simulations. Besides the axial and radial distributions of temperature and concentration, the pressure drop across the reactor constitutes another key operating characteristic. Given the inherent uncertainties in kinetic rate expressions and in the estimation of transport properties, the effect of pressure drop on the global model accuracy is generally considered negligible. However, from an operational perspective, the pressure drop can become highly relevant when evaluating the energy requirements and overall economic performance of the reactor. The pressure loss is commonly quantified through the following equation:

$$-\frac{dP}{dz} = \frac{\rho u_s^2}{2}\frac{1}{d_h} 4f \quad (2.3)$$

Due to the complex and winding flow paths within packed beds, together with the uncertainties associated with defining their hydraulic radius, the friction factor *f* is generally determined using empirical correlations. Among these, the most established and frequently applied relationship is the Ergun equation:

$$f = \frac{(1-\varepsilon)}{2\varepsilon^3}\left[\frac{\alpha(1-\varepsilon)}{Re_h} + \beta\right] \quad (2.4)$$

MacDonald et al. [225] proposed higher values, namely α = 180 and β = 1.8 for smooth particles and β = 4.0 for rough particles. In contrast, Handley and Heggs [226] determined α = 368 with β = 1.24. A comparative analysis of these formulations, together with the well-known Ergun equation,

was presented by Hicks [227], who concluded that the applicability of the Ergun equation is constrained to the range $Re_h/(1 - \varepsilon) < 500$, whereas the Handley–Heggs correlation is valid in the interval $1000 < Re_h/(1 - \varepsilon) < 5000$. Earlier, Leva [228] carried out extensive investigations on pressure drop across packed beds containing particles of different shapes and, based on these studies, proposed specific correlations for the friction factor.

$$f = 100\frac{(1-\varepsilon)^2}{\varepsilon^3 Re_h} \qquad 2.5$$

The transition from laminar to turbulent flow in packed-bed reactors spans a relatively broad Reynolds number interval, typically between 10 and 1000. In this intermediate regime, the overall pressure drop is generally estimated as the sum of the laminar and turbulent contributions. Figure 2.1 presents several correlations for the friction factor in a packed bed with an average porosity of 0.4. The two curves labeled “laminar” and “turbulent” represent the respective terms of the Ergun equation. As illustrated, all correlations produce nearly identical results except for the one proposed by Handley and Hicks. In the laminar flow region, their correlation predicts a slightly higher friction factor, and thus greater pressure losses, whereas in the turbulent regime it yields the lowest estimated pressure drop across the reactor.

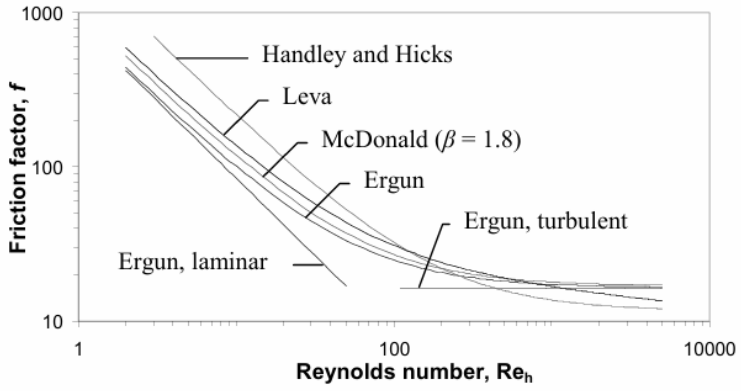

Figure 2.1 Friction factor according to various correlations for an average bed porosity ε = 0.4.

The one-dimensional pseudo-homogeneous model is widely used in chemical looping research [229,230].

The one-dimensional pseudo-homogeneous plug-flow model may only be used in case of negligible difference between the solid and fluid phase conditions and mild radial temperature and concentration profiles. If the differences between solid and fluid temperatures and concentrations are more pronounced heterogeneous model is needed.

2.3.2 One-dimensional heterogeneous model

The simplest one-dimensional heterogeneous model, taking into account temperature and concentration differences between the fluid bulk and catalyst surface reads:

Fluid phase:

$$u_s \frac{dCi}{dz} = k_f a_v (C_i^s - C_i) \quad 2.6$$

$$u_s \rho_f c_p \frac{dT}{dz} = h_f a_v (T_s - T) - \frac{4U_w}{dt}(T - T_w) \quad 2.7$$

Solid phase:

$$k_f a_v (C_i^s - C_i) = -R_i(C^s, T^s) \quad 2.8$$

$$h_f a_v (T_s - T) = R_T(C^s, T^s) \quad 2.9$$

Recent applications of heterogeneous models in methanation and biomass CLG have highlighted their ability to predict reactor stability, product selectivity and carbon deposition risks [231,233].

In addition to the inherent complexity of providing a rigorous mathematical description of packed-bed reactors, particular attention must be devoted to the formulation and handling of the governing model equations. The strong non-linearity of kinetic rate laws makes analytical solutions of the coupled differential–algebraic system rarely feasible. As a result, research efforts typically focus on approximate, numerical strategies for their resolution.

The assessment of any mathematical model is strongly linked to its mathematical tractability. On one side, a reliable model should incorporate as many of the relevant physico-chemical mechanisms as possible. On the other side, increasing the level of detail inevitably leads to more complex differential formulations, which are computationally demanding and not always manageable. The degree of model refinement is therefore largely constrained by the availability of accurate kinetic data and physical parameters, but it is equally influenced by the mathematical difficulties encountered during the solution process.

Equations arising in packed-bed reactor modelling span from simple algebraic relations to highly nonlinear, multidimensional partial differential equations. Only in very simplified cases can exact analytical solutions be derived, while in most realistic scenarios the focus is on advanced numerical treatment. Although similar classes of equations are well established in mathematical physics, the specific features of catalytic packed-bed systems introduce additional challenges that must be carefully addressed. The governing system can generally be described as a set of coupled reaction–convection–diffusion equations, which are notoriously prone to several numerical issues.

The main computational challenges include:

- pronounced stiffness due to large differences in characteristic times of the various reactions and transport processes;
- the high dimensionality of the system, often involving a very large number of equations;
- the possibility of obtaining apparently consistent but physically meaningless solutions;
- the strong interdependence between equations, resulting from the intrinsic coupling of chemical kinetics and transport phenomena.

All the numerical problems in this thesis are addressed in the computational routines included in

software COMSOL Multiphysics® employed as the primary simulation platform for modeling the chemical looping and power generation processes. COMSOL is a state-of-the-art multiphysics simulation software widely used in scientific research and engineering due to its capability to solve coupled physical phenomena using the finite element method (FEM).

In most cases, reactor models are expressed through systems of Partial Differential Equations (PDEs) that involve both temporal and spatial derivatives. Such models aim to represent the interplay of multiple chemical reactions and transport phenomena occurring simultaneously within the system. The intrinsic complexity of these coupled processes gives rise to significant challenges, both in their formal mathematical description and in the numerical resolution of the governing equations.

From a computational perspective, the solution of PDEs for chemical looping or related systems is complicated by several aspects. In this Thesis, COMSOL Multiphysics® has been used to simulate the various chemical looping processes. A significant advantage of COMSOL lies in its multiphysics coupling capabilities, which are essential for accurately capturing the complex interactions that characterize chemical looping processes. In these systems, gas–solid reactions, transient heat transfer and fluid flow occur simultaneously, necessitating an integrated modeling approach to predict reactor performance under realistic operating conditions. COMSOL's ability to combine the Chemical Reaction Engineering Module with the Computational Fluid Dynamics (CFD) and Heat Transfer Modules enables comprehensive simulation of the cyclic redox reactions, gas transport phenomena and thermal effects inherent to chemical looping reactors.

MATLAB was utilized for data analysis and the resolution of intricate heat integration problems. This software platform is widely recognized within the scientific and engineering communities for its extensive applications in data analysis, signal processing, digital communications, modeling

and optimization. It provides a broad array of tools and functions that facilitate numerical computations, simulations and data visualization.

The process simulation modeling methodology presented in this chapter offers a robust and adaptable framework to develop virtual representations of chemical looping processes. Using COMSOL Multiphysics®, this approach enables the integration of key physical phenomena, such as fluid dynamics, heat transfer and chemical reaction kinetics, into a comprehensive multiphysics model. This methodology has been applied in this Thesis to accurately simulate specific chemical looping configurations, facilitating the analysis, optimization and performance evaluation under various operational conditions.

Chapters 3, 4 and 5 present the process modelling of three advanced chemical looping systems: a two-stage CLC reactor network using Cu- and Ni-based carriers for methane combustion; an integrated process combining chemical looping gasification with methanation for renewable methane synthesis; and a detailed model of the methanation step for SNG production from biomass-derived syngas.

2.4 Conclusions

The use of multi-level modeling approaches is crucial for the robust assessment of chemical looping systems. Equilibrium models provide theoretical baselines, while 1D and pseudo-homogeneous models allow efficient screening of operational scenarios. Ultimately, heterogeneous reactor models are indispensable for the accurate design and scale-up of industrial processes.

The integrated use of these methodologies, as presented in this thesis, aligns with the latest trends in chemical engineering research, where hybrid strategies combining equilibrium, kinetic, and

CFD-based modeling are increasingly adopted to accelerate the transition of chemical looping technologies from laboratory to industrial scale.

Chapter 3 Chemical Looping Combustion in Packed-Bed Reactors: A Two-Carrier Reactor Design

3.1 Abstract

In this study, a numerical model has been developed and analyzed for a network of Chemical Looping Combustion (CLC) fixed bed reactors designed for CH_4 combustion. The configuration consists of parallel pairs of reactors connected in series. Within each pair, the first reactor contains a copper-based oxygen carrier (OC), while the second employs a nickel-based OC. The model enables assessment of the system's performance by examining both the thermal power output and the flow rate and composition of the resulting gas streams.

When maintaining the same bed length and cross-sectional area, the two-stage CLC reactor proposed here demonstrates comparable performance to a single-carrier reactor in terms of outlet gas temperature. However, it allows for shorter cycle durations and requires less active material than the single-carrier counterpart. Furthermore, the two-stage CLC network requires fewer units in total compared to the single-stage arrangement. The objective of the present chapter is to systematically assess, through detailed process modelling, the performance and potential advantages of a two-stage chemical looping combustion reactor configuration for methane-fuelled power generation, focusing on its applicability to turbine-based systems and its capacity to enhance efficiency, reduce cycle times and mitigate thermal stresses on reactor materials.

3.2 Introduction

It is widely recognized that carbon dioxide (CO_2) is the primary driver of global warming [234] and reducing its emissions represents a critical challenge for the energy industry. Given the improbability of abandoning fossil fuels in the near to medium term, it is anticipated that significant focus will be placed on Carbon Capture, Sequestration and Utilization (CCS and CCU) technologies aimed at mitigating CO_2 emissions from stationary sources in the upcoming years

[235]. Various CO_2 capture techniques, including post-combustion, oxy-combustion and pre-combustion methods, have been extensively examined within the realm of Carbon Capture processes [236,237]. While post-combustion capture is relatively mature technologically, pre-combustion capture based on chemical looping presents a promising thermodynamic advantage by lowering energy consumption. Chemical Looping Combustion (CLC) is a two-step power generation combustion process that inherently separates CO_2, thereby minimizing the typical energy penalties associated with conventional separation methods [238]. In CLC, the fuel and oxygen are not directly mixed; instead, they interact through an intermediate metal oxide, known as the Oxygen Carrier (OC), which undergoes cyclic oxidation and reduction. This arrangement avoids direct contact between fuel and combustion air, producing a nitrogen-free, CO_2-enriched gas stream. Furthermore, operating temperatures below 1300°C in CLC reduce NOx emissions, restricting them to those formed from fuel-bound nitrogen only [239]. CLC demonstrates notable adaptability to a variety of fuel types, enabling the use of gaseous, liquid and solid fuels. Although CLC remains at a pre-commercial stage, a substantial body of experimental and numerical research clearly demonstrates its excellent performance for CO_2 capture, storage (CCS) and utilization (CCU) [240]. Given the urgency of addressing climate change, a rise in commercial interest in CCS/CCU technologies is expected in the near future.

CLC systems are typically classified according to reactor design and oxygen carrier material. Most existing CLC configurations employ two interconnected fluidized beds, with one functioning as the fuel reactor and the other as the air reactor. Alternatively, packed bed reactor designs have also been proposed for CLC processes [241]. In packed beds, oxygen carrier particles remain stationary and are cyclically subjected to reducing and oxidizing atmospheres by periodically switching feed conditions. To maximize electrical efficiency, the flue gas supplied to the turbine system should be generated at pressures between 20–30 bar and temperatures near

1200°C [242,243]. However, the high operating pressure limits the use of fluidized beds due to the issue of oxygen carrier particle elutriation, which necessitates complex gas-solid separation systems downstream to protect turbines from ultra-fine particles. This challenge is inherently avoided in packed bed reactors, which additionally benefit from a more compact design compared to fluidized bed reactors [241,243]. On the other hand, because the key stages of the CLC cycle (Oxidation, Heat Removal, Purge and Reduction, OS/HR/PS/RS) happen sequentially and over different timescales in a packed bed, multiple reactors must operate in parallel to maintain a continuous supply of high-temperature gases for the turbine [242,245].

Selecting a suitable oxygen carrier for CLC involves several criteria. Since air and fuel need to be compressed to the power system operating pressure (typically 20–30 bar), the reactor inlet stream temperature is approximately 500°C. Given that the turbine inlet flue gas temperature is about 1200°C, the oxygen carrier must endure a temperature increase of roughly 700°C during cyclic operation. Therefore, the OC must be stable at high temperatures without melting or sintering, remain active at supply temperatures and withstand significant thermal cycling over many iterations. Additionally, to minimize the quantity of active solid required, the OC should exhibit a high oxygen capacity and strong selectivity towards H_2O and CO_2 to ensure complete fuel conversion. Cost-effectiveness and environmental compatibility are also crucial [246]. Various oxygen carriers have been proposed [247], but none satisfy all these requirements perfectly. Copper-based OCs offer excellent oxygen transport capacity, good durability and high reaction rates even at lower temperatures, yet their melting point restricts operation above 1050°C. Moreover, both oxidation and reduction reactions in copper carriers are exothermic, splitting the combustion heat between the two steps. As a result, while the flue gas from the oxidation stage exits the air reactor at high temperatures (~950°C) suitable for electricity generation via a combined cycle turbine, the fuel reactor's product gases only reach around 700°C,

commonly used to preheat inlet air or fuel [245]. Iron and manganese oxides generally exhibit slower reaction kinetics than copper in chemical looping combustion (CLC) [248]. Moreover, during repeated oxidation and reduction cycles, these oxides undergo significant phase transitions ($Mn_3O_4 \rightarrow MnO$ and $Fe_2O_3 \rightarrow Fe_3O_4$), which are accompanied by volume changes. Such expansion and contraction can induce mechanical stress, attrition and fragmentation of the oxygen carrier particles. This structural instability is particularly critical for manganese-based carriers, which require a high fraction of active material to sustain operation at 1200°C. Consequently, both the long-term reactivity and the mechanical durability of these carriers may be compromised, highlighting the need for careful material design and potential stabilizing strategies [249]. Abad et al. [250] demonstrated high conversion rates for Mn carriers using syngas, though their reactivity decreases with natural gas. Heat-treated manganese ores also show substantially reduced reactivity compared to fresh ores [251]. When methane is used as fuel, the reduction of Ni-, Fe-, and Mn-based oxygen carriers is endothermic, meaning that heat is absorbed during this step. However, during the subsequent reoxidation of the reduced carriers, the reactions are strongly exothermic, releasing significant heat, which can exceed the heat released by conventional combustion of the same fuel at high temperature [247,252]. These phenomena highlight the dual challenges of mechanical stability and thermal management in designing effective oxygen carriers for chemical looping processes. Nickel-based carriers are among the most widely used due to their high reactivity and excellent high-temperature performance [246], but they are costlier than other metal oxides [253], require safety precautions due to toxicity and are susceptible to carbon poisoning [254].

To address these challenges, Hammers et al. [243,255] proposed a two-stage CLC (TS-CLC) design when syngas is used as fuel. This approach splits the temperature rise between two reactors: the first reactor provides an initial temperature increase, while the second reactor raises

the flue gas temperature to the turbine inlet level. This reduces thermal cycling stress on each reactor. The choice of oxygen carriers depends on several factors, including their activity at lower temperatures and fuel type. For syngas, Hammers et al. [243, 255] recommended a copper-based carrier in the first reactor and a manganese-based one in the second. However, this configuration is suboptimal with methane fuel because both carriers show limited reactivity toward CH_4 under the studied conditions [256]. Kooiman et al. [256] experimentally investigated a pressurized two-stage CLC with a Cu-based OC in the first bed and a Ni-based OC in the second. They examined the influence of temperature, pressure and fuel composition on performance, concluding that fuel type strongly affects power generation. Despite copper's temperature limits, Kooiman et al. focused primarily on syngas but acknowledged the importance of adapting this system for methane fuel. Recently, we studied a Cu-based CLC using methane and found that flue gas temperatures cannot exceed 1000°C [245]. The TS-CLC configuration can help overcome this limitation by employing a second carrier to raise the temperature to the ~1200°C needed for efficient power production. In this study, we investigate a TS-CLC system with a Cu-based carrier in the first reactor and a Ni-based carrier in the second, using methane as fuel. The system consists of multiple pairs of fixed-bed reactors arranged in series and operated in parallel, cycling through oxidation and heat removal phases with air, purge with N_2 and reduction with methane. Employing nickel in the second stage introduces challenges due to the strongly endothermic nature of methane reduction; therefore, we developed an optimized switching strategy between phases to address this issue. The process feasibility is evaluated and compared to a single-stage copper-based reactor system.

3.2.1 Comparison Between Single and Dual Oxygen Carrier Systems in Chemical Looping Combustion

The development of chemical looping combustion (CLC) technologies has been strongly influenced by the choice of oxygen carrier (OC), as the redox properties, operating temperature windows, and long-term stability of the material directly determine process efficiency and feasibility. Among the wide range of OCs studied, nickel- and copper-based systems have been the most extensively investigated for methane CLC, each presenting distinctive advantages and limitations. A novel configuration employing two different OCs in series, specifically Cu and Ni, has been explored in this thesis. This dual arrangement allows the integration of the complementary properties of each carrier and deserves to be critically compared with the performance of single-carrier systems reported in the literature.

Nickel-based oxygen carriers (NiO/Ni) exhibit very high intrinsic reactivity with methane, enabling near-complete conversion to CO_2 and H_2O under suitable operating conditions. Their reduction is strongly endothermic, requiring external or internal heat supply to sustain reactor operation, but their oxidation is highly exothermic and provides robust energy recovery. Kinetic studies based on thermogravimetric analysis and packed-bed reactors have consistently reported fast reaction rates and well-defined kinetic parameters [257–259]. Pilot-scale demonstrations with methane and solid fuels also confirm the capacity of Ni-based carriers to achieve high conversions and effective CO_2 capture [260,261]. Nonetheless, their use is limited by the propensity for carbon deposition under oxygen-deficient conditions, their susceptibility to sulphur poisoning, and concerns over toxicity and cost [262,263].

In contrast, copper-based oxygen carriers (CuO/Cu_2O) display a distinctly different thermodynamic profile. The reduction of CuO is exothermic, allowing heat release already in the reduction stage, and the carriers are particularly reactive at intermediate temperatures. Studies on Cu-based carriers have shown stable performance in pilot plants up to 120 kW for gaseous fuels, with methane conversions exceeding 90% under optimized conditions [261,264,265]. Moreover, copper carriers

are less prone to carbon deposition than Ni. However, their utility is constrained by the relatively low melting and sintering temperature of copper oxides (~1079 °C), which limits the maximum operational temperature and raises risks of agglomeration at the high outlet temperatures required for efficient power generation. The effect of fuel gas composition, particularly the presence of sulphur compounds, has also been identified as a key challenge for CuO stability and regenerability [261].

Extensive comparative studies of Cu-, Ni-, Fe-, and Mn-based OCs [262,263,266] have clarified that Ni excels in high-temperature, high-reactivity scenarios, while Cu performs well at lower-to-intermediate temperatures but cannot provide the temperature levels needed for advanced combined-cycle applications. This complementarity has inspired research into mixed or combined carriers. Bimetallic Ni–Cu formulations, as well as dual-bed configurations, have been investigated to exploit synergies: nickel ensures complete methane conversion while copper contributes favorable thermal effects and reduces the risk of carbon deposition [262,264,266].

The dual-carrier configuration investigated in this thesis, in which methane sequentially contacts a Cu-based bed followed by a Ni-based bed, integrates these advantages at the process level. The exothermic reduction of CuO in the first stage preheats the system, partially compensating for the endothermicity of NiO reduction in the subsequent bed. This arrangement extends the effective operating temperature window, enabling higher outlet gas temperatures (1150–1200 °C) suitable for turbine expansion, a performance that cannot be achieved with Cu alone due to its thermal stability limits. Compared with a single-Cu configuration, the Cu→Ni system achieved not only higher thermal output but also an estimated increase of approximately 40% in net electrical power production for the same methane feed rate. Moreover, the dual-OC scheme reduced the total active material inventory required by more than half and lowered the number of parallel units needed for continuous operation [267–269].

These outcomes are consistent with literature observations on hybrid or dual-OC systems, where combinations of Cu- and Ni-based carriers have demonstrated widened operational windows, enhanced thermal efficiency, and reduced risk of deactivation [258,267,270,271]. The serial Cu→Ni arrangement therefore represents a significant step forward in reactor design, bridging the gap between the high reactivity but challenging thermal balance of Ni-only systems and the thermally favorable but temperature-limited Cu-only systems.

In summary, while Ni and Cu individually present well-defined strengths and weaknesses, their integration in a dual-carrier configuration enables synergistic exploitation of their properties, delivering superior performance in terms of methane conversion, thermal management, and power generation potential. This comparison strongly supports the relevance of the approach investigated in this chapter as a promising pathway toward the development of efficient and robust CLC systems for methane utilization and CO_2 capture.

3.3 Mathematical Model

Section 3.3.1 provides a concise description of the reaction kinetic models for Cu/CuO and Ni/NiO oxygen carriers supported on γ-Al_2O_3. The governing balance equations that describe the reactor dynamics are detailed in section 3.3.2.

3.3.1 Kinetic Scheme

The reaction mechanism for the copper oxide oxygen carrier on γ-Al_2O_3 is summarized in Table 3.1, which also lists the standard reaction enthalpies. In the oxidation phase, the oxygen carrier undergoes oxidation by air following reaction (R1). During the reduction phase, methane is converted into CO_2 and H_2O through reaction (R2) [272].

Table 3.1 Reactions scheme and associated standard enthalpies of reactions for the copper oxide oxygen carrier on γ-Al_2O_3

Reaction	ΔH° (kJ/mol)	
$2Cu + O_2 \rightarrow 2CuO$	-296	R1
$4CuO + CH_4 \rightarrow 4Cu + CO_2 + 2H_2O$	-176	R2

Following the approach described in [272], the shrinking-core model for a plate-like geometry under chemical reaction control has been employed to characterize the reaction rate of Cu-based oxygen carriers interacting with either fuel gas or air. This model is represented by the following equations (refer to the nomenclature section for symbol definitions):

$$\frac{dX_j}{dt} = \frac{1}{\bar{\tau}_j} \tag{3.1}$$

$$\bar{\tau}_j = \frac{\rho_{m,k}\bar{L}_k}{\xi_j K_{0j} C_j^m} \tag{3.2}$$

$$r_j = \frac{\varepsilon_s \varepsilon_p \rho_s w_{act}^0 \eta_j}{M_k} \frac{dX_j}{dt} \tag{3.3}$$

The kinetic parameters provided by Garcia-Labìano et al. [273] have been adopted, with further elaboration available in Diglio et al. [245]. For Ni-based oxygen carriers supported on γ-Al_2O_3, Iliuta et al. [274] proposed that methane conversion proceeds via intermediate formation of H_2 and CO, whereas the oxidation kinetics of the Ni oxygen carrier follow the framework suggested by Dueso et al. [275]. The overall reaction network is detailed in Table 3.2.

Reaction (R3) represents the oxidation of the oxygen carrier during the oxidation step. The reactions from (R4) to (R10) encompass the main chemical-looping reduction processes,

including partial oxidations of methane (R4 and R7), oxidations of H_2 and CO (R5 and R6 respectively). These are complemented by Ni-catalyzed reduction reactions such as Steam Methane Reforming (R8), Dry Reforming (R9) and the Water Gas Shift Reaction (R10). The rates for the oxidation (R3) and non-catalytic gas-solid reductions (R4-R7) are modeled based on volumetric particle theory as described in [274]. Kinetic data related to catalyzed reaction rates, equilibrium constants and adsorption parameters are available for Cu-based oxygen carriers in [245] and for Ni-based carriers in [276-277].

Table 3.2 Reactions scheme and associated standard enthalpies of reactions for Ni-based oxygen carriers supported on γ-Al_2O_3.

Reaction	**ΔH°**	
$2Ni + O_2 \rightarrow 2NiO$	-479	R3
Non Catalytic Reactions		
$CH_4 + 2NiO \leftrightarrow 2Ni + CO_2 + 2H_2$	161	R4
$H_2 + NiO \leftrightarrow Ni + H_2O$	-2	R5
$CO + NiO \leftrightarrow Ni + CO_2$	-43	R6
$CH_4 + NiO \leftrightarrow Ni + CO + 2H_2$	203	R7
Catalytic Reduction reactions		
$CH_4 + H_2O \overset{Ni}{\leftrightarrow} 3H_2 + CO$	206	R8
$CH_4 + CO_2 \overset{Ni}{\leftrightarrow} 2H_2 + 2CO$	247	R9
$CO + H_2O \overset{Ni}{\leftrightarrow} CO_2 + H_2$	-41	R10

In the kinetic scheme outlined in Table 3.2, methane decomposition, carbon gasification by steam (R12), the Boudouard reaction and carbon oxidation are omitted. This choice is justified by the small nickel content in the two-stage system, which leads to minimal carbon deposition. Hence, at this stage of the study, carbon deposition effects are considered negligible. Furthermore, Diglio et al. [254] demonstrated that any deposited carbon would be rapidly and spontaneously oxidized during the oxidation phase, affecting primarily the overall process duration and CO_2 capture efficiency. This assumption aligns with the findings of Hammers et al. [255].

The consumption or generation rate of each species r_i (i=X, NiO, Ni, Cu, CuO, CH_4, H_2, H_2O, CO, CO_2, O_2, N_2) is calculated by summing the contributions of that species across all reactions R_j (j=1,2…10, see Tables 3.1 and 3.2). Thus, the reaction rate for each species in the Cu-based oxygen carrier system can be formulated as:

$$\begin{cases} r_{CH_4} = -r_{R2} \\ r_{H_2O} = 2r_{R2} \\ r_{CO_2} = r_{R2} \\ r_{O_2} = r_{R1} \\ r_{N_2} = 0 \\ r_{CuO} = 2r_{R1} - 4r_{R2} \\ r_{Cu} = -r_{CuO} \end{cases} \tag{3.4}$$

And for Ni-based carrier:

$$\begin{cases} r_X = 2r_{R4} + r_{R5} + r_{R6} - 2r_{R3} \\ r_{NiO} = -M_{NiO} r_X \\ r_{Ni} = M_{Ni} r_X \\ r_{CH_4} = -r_{R4} - r_{R7} - C_{Ni}\left(r_{R8} + r_{R9}\right) \\ r_{H_2} = 2r_{R4} - r_{R5} + 2r_{R7} + C_{Ni}\left(3r_{R8} + 2r_{R9} + r_{R10}\right) \\ r_{H_2O} = r_{R5} - C_{Ni}\left(r_{R8} + r_{R10}\right) \\ r_{CO_2} = r_{R4} + r_{R6} - C_{Ni}\left(r_{R9} + r_{R10}\right) \\ r_{CO} = -r_{R6} + C_{Ni}\left(r_{R8} + 2r_{R9} - r_{R10}\right) \\ r_{N_2} = 0 \end{cases} \quad (3.5)$$

Reactions (R8-R10) are catalysed by nickel and can only occur when Ni is present and the overall N_2 reaction is zero.

3.3.2 Governing Equations

A 1D pseudo-homogeneous model was employed to characterize the dynamic behavior of the adiabatic packed bed reactors. The absence of radial gradients in concentration and temperature, as well as the lack of interphase and intra-particle gradients in these variables, has been confirmed; further information is available in [245, 278].

The governing equations for both reactors are summarized in Table 3.3, along with their corresponding boundary conditions. In simulations of TS-CLC, the outlet temperature and concentration from the first reactor serve as the inlet conditions for the second reactor. The axial dispersion coefficient (D_{ax}) was calculated using the correlation developed by Edwards and Richardson [279], whereas the effective axial heat dispersion coefficient (λ_ax) was determined following the formulation by Yagi and Wakao [280].

During the reduction step (RS), the gas phase included CH_4, H_2O, CO, CO_2 and H_2, while only O_2 and N_2 were considered during the oxidation step (OS) and the heating regeneration (HR)

step. In the purge step (PS), a pure N_2 stream was introduced. The rates of gas species formation or consumption (r_i) and of solid species (r_k) were computed by summing the reaction rates of species involved in the reactions R_j, as described by Eqs. (3.4) and (3.5), respectively. It is important to note that no reactions occur during HR and PS. The system of equations given in Table 3 is complemented by a set of initial conditions; initial values for each stage after the first were taken as the final computed values from the previous stage, reflecting the cyclic operation of the CLC process. Additional details on the mathematical representation of cyclic initial conditions can be found in [278].

To account for the dependence of reaction enthalpies, transport coefficients and gas properties on temperature, pressure and composition, the model utilized advanced correlations and assumptions reported by Han et al. [281] and associated references.

The mathematical model was implemented and solved using the commercial software COMSOL Multiphysics®. The reactor length (L) was discretized into 500 nodes and mesh refinement studies confirmed that further spatial discretization did not significantly affect the computed temperature and concentration profiles. Validation of this mathematical model against literature data has been addressed in previous works [241, 254, 278].

Table 3.3 1D pseudo-homogeneous mathematical model of TS-CLC configuration

Gas phase mass balance	$\varepsilon_g \frac{\partial C_i}{\partial t} + u_g \frac{\partial C_i}{\partial z} = \varepsilon_g \frac{\partial}{\partial z}\left(D_{ax} \frac{\partial C_i}{\partial z}\right) + \varepsilon_g r_i$
Solid phase mass balance	$\frac{\partial C_k}{\partial t} = r_k$
Energy balance	$\left[\left(\varepsilon\rho c_p\right)_g + \left(\varepsilon\rho c_p\right)_s\right] \frac{\partial T}{\partial t} + \left(\varepsilon\rho c_p\right)_g u_g \frac{\partial T}{\partial z} = \varepsilon_g \frac{\partial}{\partial z}\left(\lambda_{ax} \frac{\partial T}{\partial z}\right) + \varepsilon_g r_j\left(-\Delta H_j\right)$
Momentum balance	$-\frac{dP}{dz} = 150 \frac{\mu_g u_g}{d_p^2} \frac{\left(1-\varepsilon_g\right)^2}{\varepsilon_g} + 1.75 \frac{\rho_g u_g^2}{d_p} \frac{\left(1-\varepsilon_g\right)}{\varepsilon_g^3}$
Boundary conditions	$\frac{\partial C_i(0,t)}{\partial z} = \frac{u_g}{\varepsilon_g D_{ax}}\left(C_i(0,t) - C_{i,in}\right),\ \frac{\partial C_i(L,t)}{\partial z} = 0$ $\frac{\partial T(0,t)}{\partial z} = \frac{u_g c_{pg} \rho_g}{\varepsilon_g \lambda_{ax}}\left(T(0,t) - T_{in}\right),\ \frac{\partial T(L,t)}{\partial z} = 0$ $P(0,t) = P_{in}$
Additional equations	$D_{ax} = \left(\frac{0.73}{Re \cdot Sc} + \frac{0.5}{\varepsilon_g + \frac{9.7\varepsilon_g^2}{Re \cdot Sc}}\right) u_g d_p$ $\lambda_{ax} = \lambda_e^0 + 0.\,tPr \cdot Re \cdot \lambda_g$

3.4 Results and Discussion

When incorporating a Chemical Looping Combustion (CLC) process into a power system, establishing an effective heat management strategy (HMS) is critically important. Generally, two primary HMS approaches can be implemented [283], depending on whether heat stored within the reactor is extracted after the oxidation phase (HR-MeO) or following the reduction phase (HR-Me). In the former approach, heat removal is achieved by supplying air to the reactor until the entire bed returns to its initial temperature. This strategy is particularly suitable when the oxygen carrier (OC) maintains high reactivity even at lower temperatures, as the solid begins the reduction reaction at a relatively low temperature. Conversely, in the latter case, since the carrier is in its reduced state, heat extraction cannot be performed by air feeding; instead, an

inert gas such as N_2 must be used. This HMS has been suggested for OCs exhibiting lower reactivity [283]. There are, however, OCs like copper-based ones where both the oxidation and reduction reactions of the carrier release heat (exothermic). To prevent the carrier from reaching its melting point, it is necessary to remove heat after both oxidation and reduction phases, even if the temperature achieved at the end of reduction is not suitable for power generation [245]. For nickel-based oxygen carriers, the oxidation reactions are highly exothermic, whereas the reduction reactions are endothermic. Heat removal is therefore conducted after the oxidation step, but not all the generated heat can be extracted. Consequently, the temperature of the feed entering the reduction phase must be increased to compensate for the endothermic nature of the reduction reactions.

3.4.1 One-Stage Chemical Looping Combustion with Cu/CuO as Oxygen Carrier

This section presents the spatial profiles of temperature, solid conversion and gas composition for the one-stage CLC system utilizing a copper-based carrier. The analysis provides crucial insights into how the heat and reaction fronts develop within the reactor. Following this, the cyclical steady-state behavior is discussed to explain how the control strategy governs the switching between the operational phases in CLC. Model parameters for the one-stage CLC with Cu as the oxygen carrier are provided in Table 3.4, while the boundary conditions are reported in Table 3.5.

Table 3.4 Model parameters for single Cu Carrier

Parameter	Value
P_{in}, MPa	2.0
T_{in}, K	850
T_0, K	850
L, m	2.0
d_r, m	0.7
ρ_{CU}, kg·m^{-3}	8950
ρ_{Al2O3}, kg·m^{-3}	3965
$C_{Cu,max}$, mol·m^{-3}	5200
ε_s	0.4
w_{act}^0	0.23
m_{Cu}, kg	281

Table 3.5 Detailed boundary conditions

	OS	HROS	PS	RS	HRRS
T_{in}, K	850	850	850	850	850
P_{in},bar	20	20	20	20	20
$C_{i,in}$	$C_{O2,in}=0.21(P_{in}/R/T_{in})$ $C_{N2,in}=0.79(P_{in}/R/T_{in})$	$C_{O2,in}=0.21(P_{in}/R/T_{in})$ $C_{N2,in}=0.79(P_{in}/R/T_{in})$	$C_{N2,in}=(P_{in}/R/T_{in})$	$C_{CH4,in}=(P_{in}/R/T_{in})$	$C_{N2,in}=(P_{in}/R/T_{in})$
$Gs_{,in}$	2.0	2.0	6.0	2/15	2.0

In Figure 3.1 the spatial profiles for temperature, gas composition and carrier conversion degree are reported during oxidation stage for several time instants.

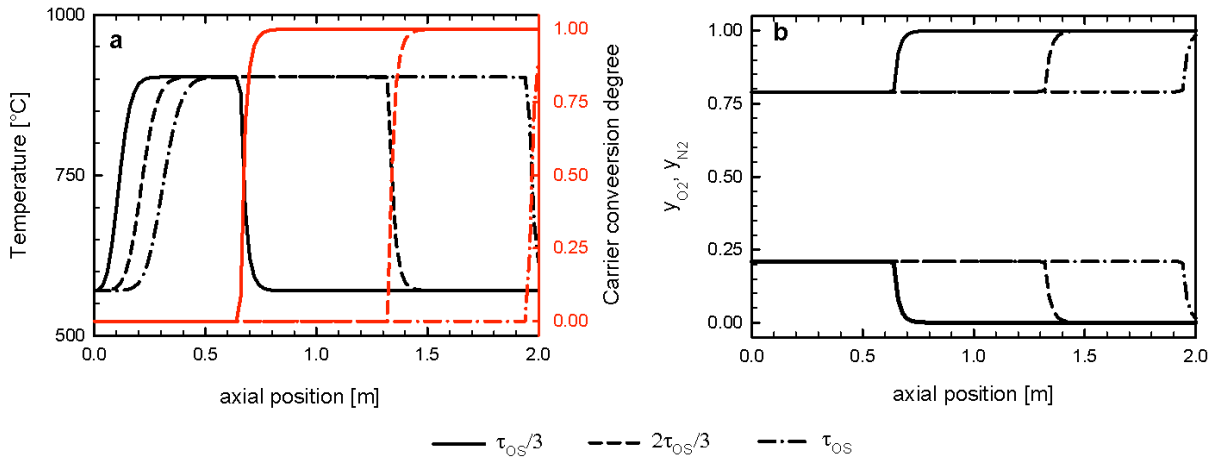

Figure 3.1 Axial temperature, carrier degree conversion (red lines) (a) and gas composition (b) profiles during OS for several time instants according to the legend, $\tau_{OS} = 320\,s$

The chosen initial temperature T_0 is sufficiently close to the reduction reaction threshold temperature (approximately 873 K [273] when air is supplied). The reduced oxygen carrier (OC) subsequently reacts with O_2 to form CuO following reaction R1. Given that this reaction is exothermic, the temperature rises during the oxidation step (see Figure 3.1a). Notably, a sharp temperature increase is observed at the site of the oxidation reaction and the temperature profile along the reactor exhibits the typical characteristics of a reaction front. Concurrently, the gas composition along the reactor axis changes, with oxygen nearly depleted downstream of the reaction front (Figure 3.1b). Due to the difference between the air feed temperature and the bed temperature, the temperature profile assumes a bell-shaped distribution.

The thermal front velocity, V_{th}, corresponds to the speed at which the cooler zone downstream of the peak temperature advances towards the reactor outlet. Conversely, the oxidation reaction front velocity, V_{fr}, is the speed at which the hot region upstream of the peak temperature moves towards the reactor exit. Following Noorman et al. [241], these velocities are defined as follows:

$$V_{th} = \frac{\rho_g u_g c_{pg}}{\rho_{OC}(1-\varepsilon_g)c_{ps}}$$
$$V_{fr} = \frac{\rho_g u_g w_{g,i,in} M_{act}}{\rho_{OC}(1-\varepsilon_g) w_{act} M_i \xi} \quad (3.7)$$

Because the oxygen carrier contains a substantial amount of inert solid, V_{fr} is always higher than V_{th} [241]. Under the parameter values used in this simulation, the reaction front velocity significantly exceeds that of the thermal front, a highly advantageous condition for Chemical Looping Combustion (CLC) processes. This velocity difference ensures that, by the end of the oxidation step (OS), nearly all generated heat remains within the reactor (Figure 3.1a) and can be subsequently recovered for turbine power generation. According to Noorman et al. [241], when the reaction front progresses faster than the thermal front, the gas approaches the reaction zone preheated by the solid and the maximum adiabatic temperature increase is estimated by:

$$\Delta T = \frac{-\Delta H}{\frac{c_{ps} M_{act}}{w_{act}^0 \xi} + \frac{c_{pg} M_g}{w_g}} \quad (3.8)$$

Furthermore, the maximum attainable temperature, T_{max}, can be computed from the temperature rise ΔT and the initial solid temperature as follows [283]:

$$T_{max} = T_0 + \Delta T \quad (3.9)$$

Since copper's reduction reaction is also exothermic, a similar behavior occurs during the reduction phase (Figure 3.2a). Initially, the bed contains only CuO; as methane (CH_4) is introduced, fuel oxidation reactions commence (R2), producing H_2O and CO_2 while simultaneously reducing the carrier to Cu (Figure 3.2b). The thermal front velocity is strongly dependent on the gas density and velocity product $\rho_g u_g$ (Eq. 3.7). Given that this term is roughly one-fifteenth of its oxidation phase value (Table 3.5), the thermal front remains localized near the

reactor inlet. Consequently, at the end of the reduction step, the temperature profile within the bed is nearly uniform.

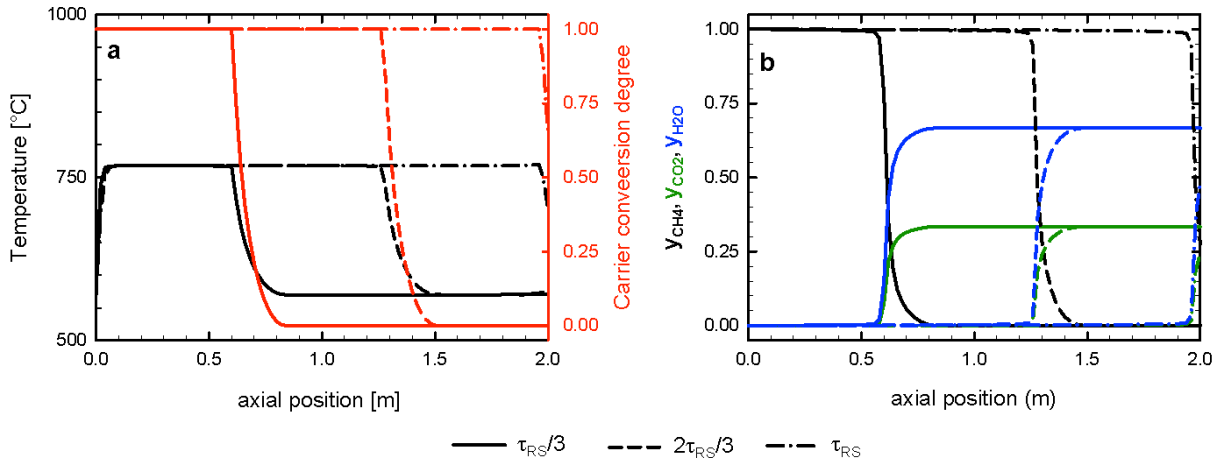

Figure 3.2 Axial temperature and carrier conversion degree (red lines) (a) and gas composition profiles (black: CH_4, blue: H_2O, green: CO_2) (b) at various times during RS, as indicated in the legend.

In Figure 3.3, a typical sequence of spatial temperature profiles during heat removal after the oxidation step (HROS) is presented. Here, a thermal front moves steadily along the reactor at constant velocity.

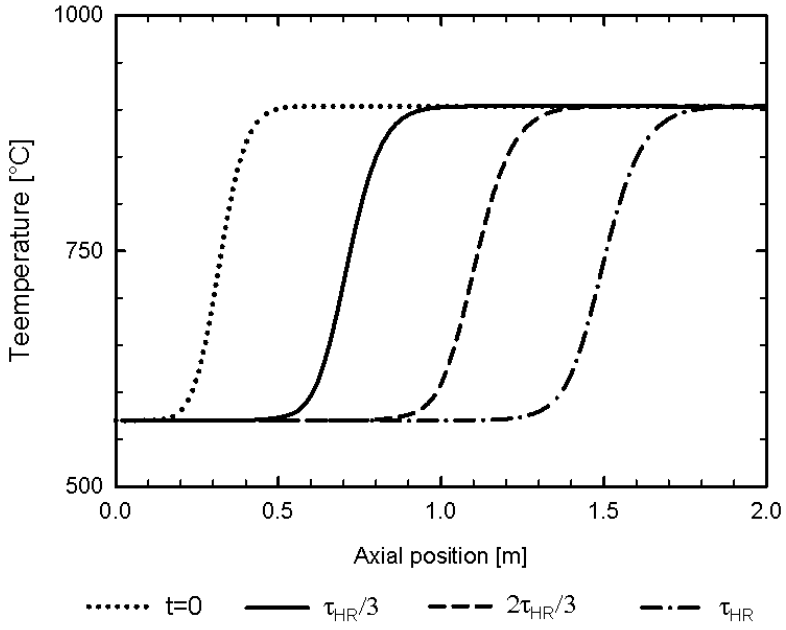

Figure 3.3 Axial temperature profiles during HROS at different time instants.

It should be emphasized that to prevent the formation of explosive mixtures, a purge stage is mandatory when transitioning between air and methane feeds and vice versa. Therefore, single-stage Cu-based CLC systems must incorporate this purge phase into their design. The full CLC process under study involves the following five-step cyclic sequence:

1. **Oxidation of carrier (OS):** Air is introduced, oxidizing the carrier and generating heat at elevated temperatures.
2. **Heat Removal after Oxidation (HROS):** Most of the heat generated during OS remains inside the reactor and air continues to flow to produce a high-temperature gas stream for power generation.
3. **Purge (PS):** To avoid explosive mixtures, a purge phase separates the oxidation and reduction stages, during which methane is subsequently fed.

4. **Reduction (RS):** Methane is oxidized exothermically via carrier reduction, generating a hot, concentrated CO_2 stream suitable for storage.
5. **Heat Removal after Reduction (HRRS):** Heat produced during RS is removed using an inert gas such as N_2, as the carrier is in its reduced state.

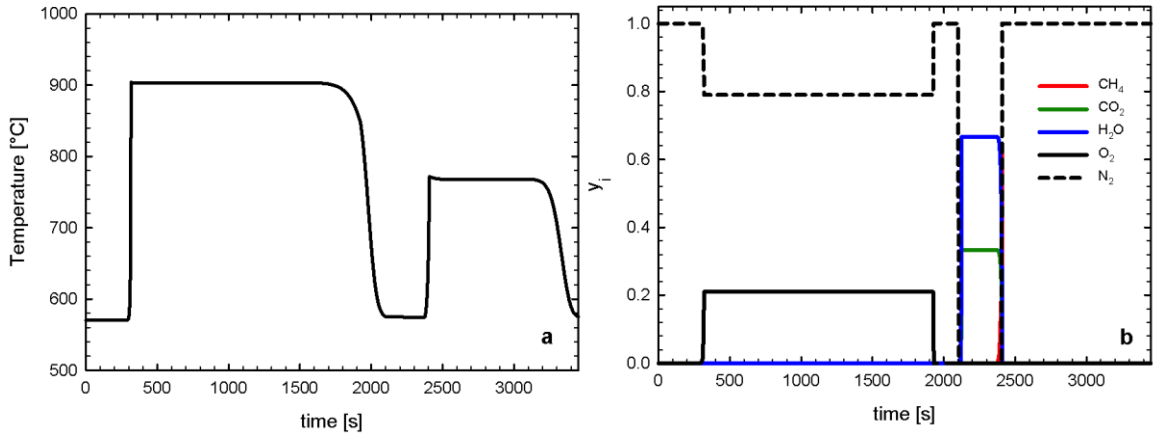

Figure 3.4 Outlet temperature (a) and gas concentrations (b) monitored during the first CLC cycle.

Figure 3.4 shows the monitored outlet temperature and gas concentrations during the initial CLC cycle. The duration of each phase is not fixed beforehand but dynamically controlled by an automated system. This controller ensures complete oxidation and reduction of the carrier in their respective phases, maintains a nearly constant temperature gas feed for the turbine and removes excess heat from the reactor to protect the carrier during the subsequent oxidation step. Further details on the control strategy are available in Diglio et al. [245].

Table 3.6 Period of each stage in Chemical Looping Combustion with Cu/CuO

Stage	Periods
OS	320
HROS	1610
PS	170
RS	230
HRRS	1050

The total CLC cycle period is $\bar{\bar{T}}$ = 3380 s, with individual stage durations summarized in Table 3.6. This data indicates that multiple reactors operating in parallel are required to provide a continuous hot gas stream at roughly constant temperature during heat removal. A minimum of four parallel reactors ($N_r = N_{min}$) was selected for the target process, ensuring that at least one reactor operates in the HRRS phase. This number increases only if the pressure drop in any stage exceeds the inlet value by 15% [245]. Hence, four reactors in parallel were adopted, generating two constant-temperature streams, the hottest of which feeds the power generation system.

3.4.2 Two-stage CLC with Cu/CuO and Ni/NiO oxygen carriers

The fundamental principle of the two-stage CLC (TS-CLC) process is that the heat released in each stage of the first reactor is transferred to the second reactor, facilitating the desired temperature increase. Figure 3.5 provides a schematic representation of the TS-CLC system utilizing Cu and Ni carriers. Initially, the two reactors have different temperatures (see Table 3.7), with the process described starting at the reduction stage. Because Cu reduction (R2) is mildly exothermic and Ni reduction (R4–R10) is endothermic, the first reactor experiences a temperature increase while the second sees a decrease (Figure 3.5). The heat generated during RS in the Cu-based reactor is stored and subsequently used to raise the temperature during the following OS (Eq. 3.9). This heat is transferred to the Ni-based second reactor to offset temperature drops caused by the preceding RS. After OS, heat removal (HR) occurs.

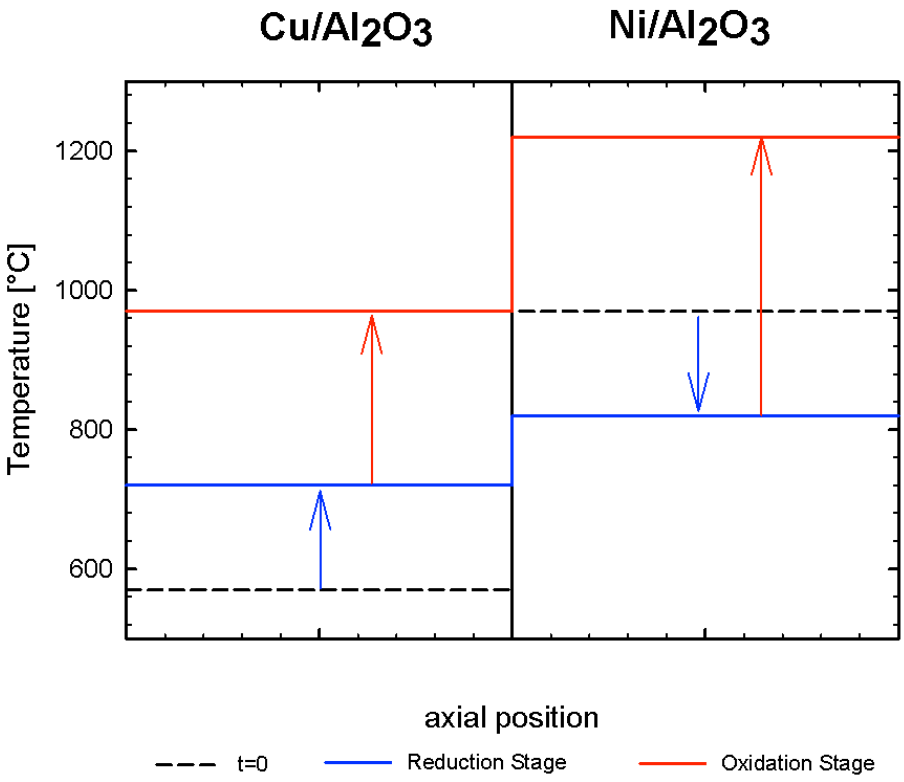

Figure 3.5 Schematic layout of the TS-CLC configuration and axial temperature profiles.

Numerical simulation results for the two-reactor system in series are presented, using parameters listed in Table 3.7. The active phase percentages are 13% for Cu (compared to 23% in the single-stage reactor) and 10% for Ni, both supported on Al_2O_3. Since the second reactor operates at higher temperatures, its initial temperature is set at 1000 °C, while the first reactor begins at 570 °C [243]. Boundary conditions align with those in Table 3.5, except the HRRS phase is omitted in TS-CLC.

Table 3.7 Model parameters for TS-reactor

Parameter	Value
P_{in}, MPa	2.0
T_{in}, K	850
T_{0Cu}, K	850
T_{0Ni}, K	1270
L_{Cu}, m	1.0
L_{Ni}, m	1.0
d_r, m	0.7
ρ_{Ni}, kg·m^{-3}	7785
ρ_{Cu}, kg·m^{-3}	8950
ε_s	0.4
w_{actCu}^0	0.13
$C_{Cu,max}$, mol·m^{-3}	2943
m_{Cu}, kg	72
w_{actNi}^0	0.1
$C°_{NiO}$, mol·m^{-3}	2330
m_{Ni}, kg	52

Figures 3.6 and 3.8 depict spatial temperature and gas molar fraction profiles during RS at various times. After 190 s (τ_{red}), both reactors are fully reduced, with reduction times roughly equal due to the chosen active phase percentages. The initial temperature of the first reactor aligns closely with the activation temperature of R2 (Table 3.1), resulting in a smoother reaction front (t=τ_{RS}/2: see Figs.3.6 and 3.7a). Because methane concentration is non-zero beyond the reaction front, reduction begins in the second reactor before full CuO reduction completes in the first (t=τ_{RS}/4: see Figures 3.6 and 3.7b). As discussed earlier, the reaction front outpaces the thermal front; thus, during the time required for full reduction of the first reactor, the thermal front remains near its inlet, barely penetrating the second reactor. Consequently, by Eq. 3.9, reduction in the initial layers of the second reactor begins at a temperature below its initial 1000 °C, approximately 740 °C, as reached in the first reactor post-reduction, causing a non-monotonic spatial temperature profile. This behavior also influences gas concentration (Figures 3.7b-c). During reduction in the

first reactor alone, H_2O, CO_2 and unreacted CH_4 are detected at the outlet. When RS nears completion in the first reactor, reduction starts in the Ni-based reactor, producing H_2 and CO alongside CH_4, H_2O and CO_2 per Table 3.1.

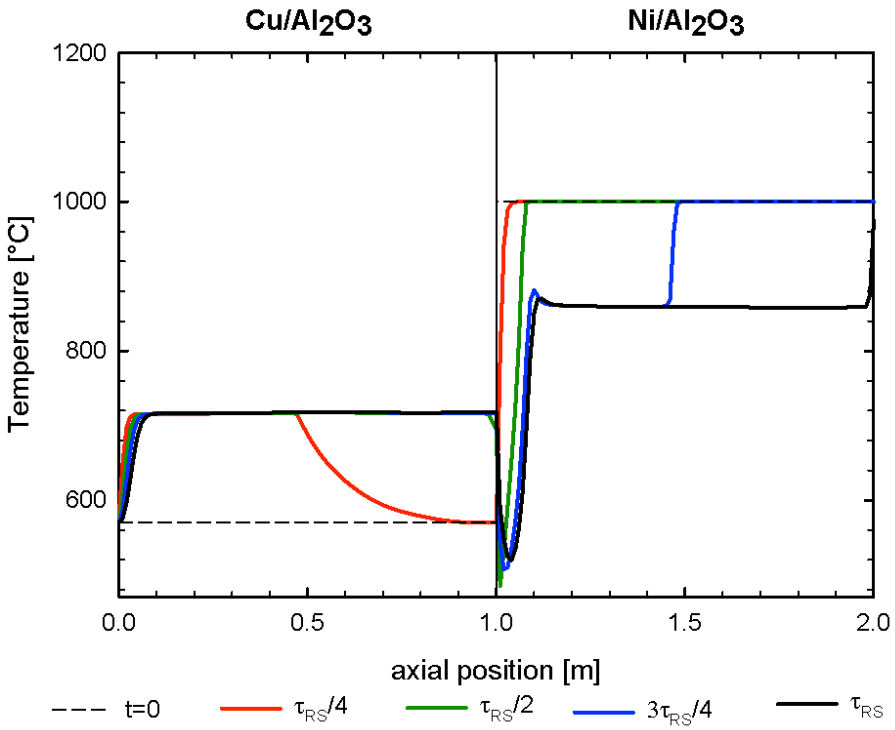

Figure 3.6 Spatial temperature profiles during RS at multiple time points (τ_{RS}=190 s).

H_2 and CO form near the reaction front, as nickel downstream remains oxidized, rapidly consuming these species (R5 and R6). The heat generated during Cu reduction is retained for the subsequent OS, eliminating the need for HRRS. Following RS, a brief purge with nitrogen occurs ($\tau_{PS} \approx 30\ s$) at a higher flow rate than during reduction (see Table 3.5). Purge duration corresponds to the total reactor void volume [255].

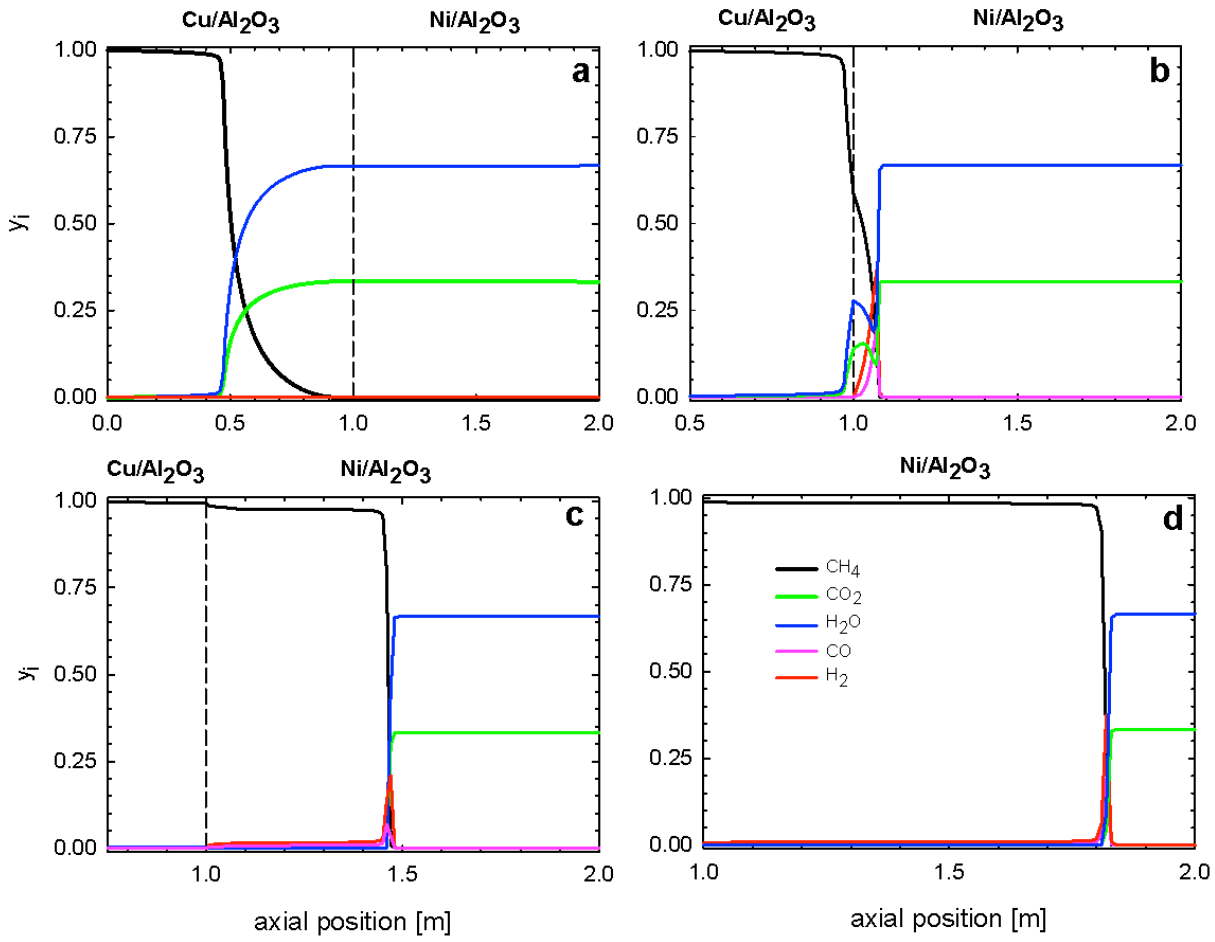

Figure 3.7 Gas composition profiles during RS at: a) $\tau_{RS}/4$; b) $\tau_{RS}/2$; c) $3\tau_{RS}/4$ and d) at τ_{RS}=190 s.

Figure 3.8 presents temperature profiles during OS at various times. The dashed line marks temperature distribution at purge completion. For the chosen gas flow and active phase percentages, the OS duration ($\tau_{OS} = 195\ s$) closely matches RS. The Cu-based carrier fully oxidizes in about 100 s, similar to Ni-based oxidation. Higher OS temperatures produce classic stepped reaction fronts, with oxidation in the second reactor commencing only after complete oxidation of the first. Two distinct temperature plateaus appear at OS completion: approximately 970 °C in the first reactor and 1220 °C in the second.

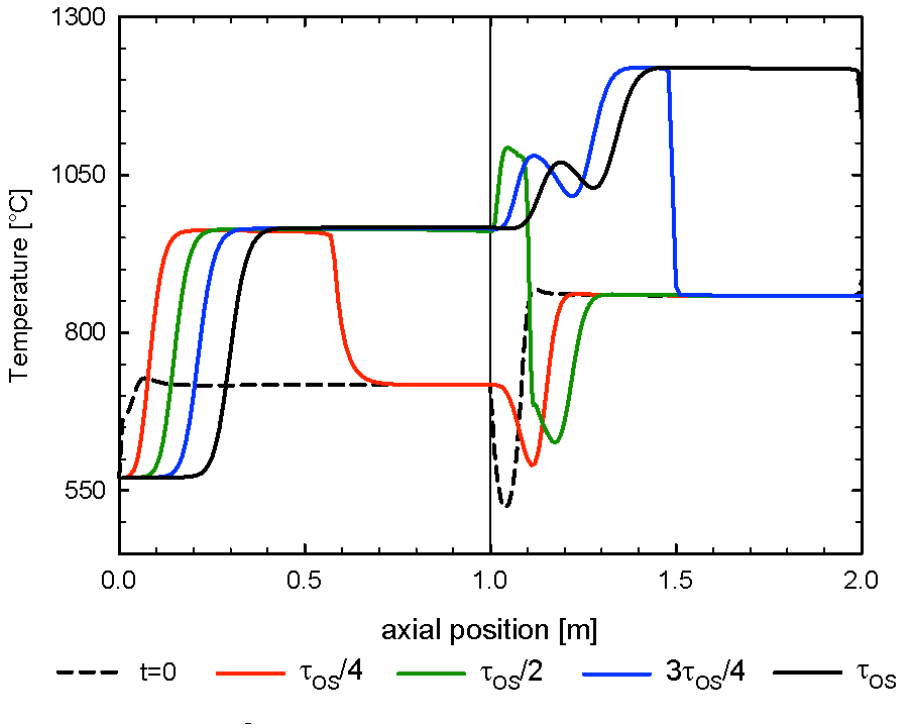

Figure 3.8 Spatial temperature profiles during OS at various times (τ_{OS}=195 s).

During the subsequent heat removal step, air is fed despite fully oxidized carriers. Figure 3.10 displays axial temperature profiles during HROS, with the dashed line showing temperatures at OS completion. HROS continues until outlet gas temperature falls below 1175 °C to maintain a stable gas temperature for downstream units. The heat removal duration is similar for both Ni and Cu oxidation heat. By the end of this phase, the second bed cools to about 970 °C. A quick purge at increased flow follows.

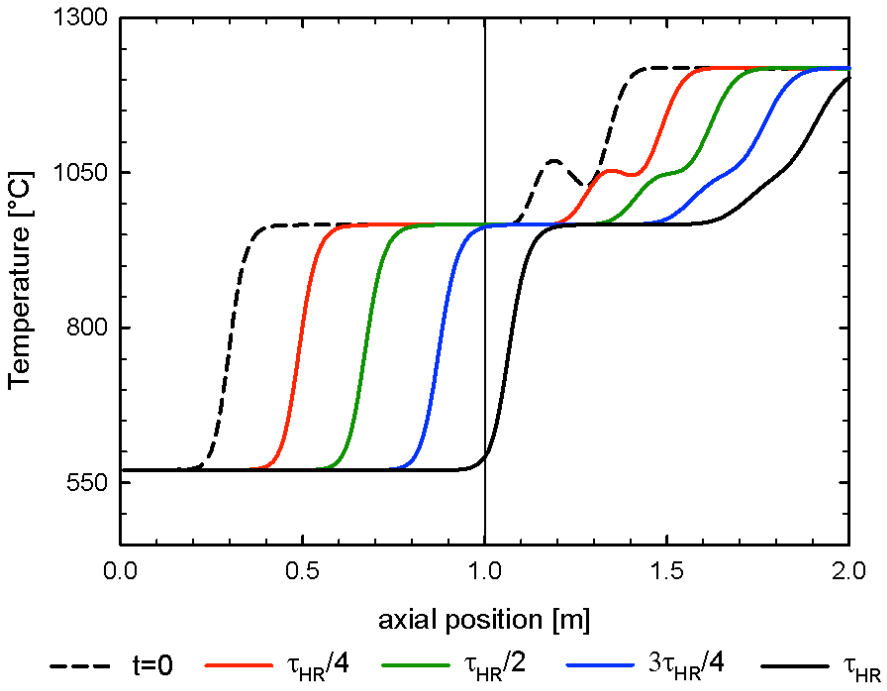

Figure 3.9 Spatial temperature profiles during HR at multiple times (τ_{HR}=485 s).

As before, stage durations are governed by a controller rather than preset. Figure 10 shows outlet gas concentrations (a) and temperature (b) during the first TS-CLC cycle starting at RS. The control logic is as follows: i) switch from RS to PS when CH_4 outlet concentration reaches ~90% of inlet to ensure full carrier reduction; ii) PS duration is set to 15% of prior RS length; iii) The transition from OS to HROS occurs when the oxygen concentration at the reactor outlet attains 95% of its inlet level, ensuring complete oxidation of the oxygen carrier within the reactor. iv) HROS operation proceeds until the temperature of the outlet gas falls below 1150 °C, thereby supplying a gas stream with an approximately stable temperature to the downstream process unit. v) A brief purge is carried out prior to switching to RS.

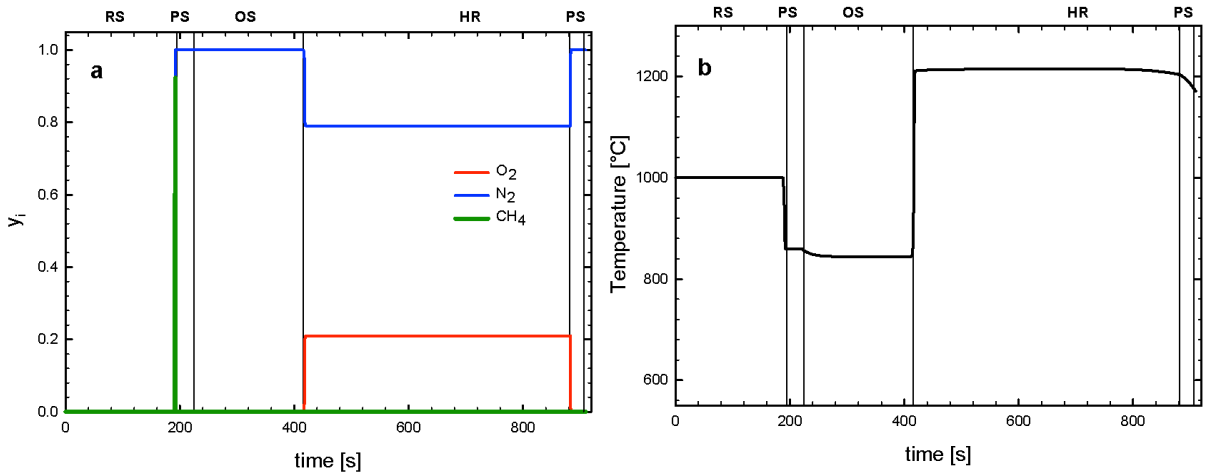

Figure 3.10 Evolution of outlet gas concentrations (a) and temperatures (b) during the initial TS-CLC cycle. The vertical lines indicate the completion of each process stage.

From this data, it can be deduced that the overall TS-CLC cycle duration is approximately 910 seconds. Table 3.8 presents the time allocated to each stage. It is evident that each stage in the two-stage configuration lasts for a shorter duration compared to those observed in the one-stage Cu-based reactor (see Table 3.5). This is attributable to several factors: unlike the prior case involving a single 2-meter reactor, the current system divides the same total length across two reactors. Furthermore, the amount of active oxygen carrier is lower in this setup. As previously discussed (refer to Figure 3.9), heat removal is constrained to only two-thirds of each reactor's length, which impacts thermal management and reaction time.

Table 3.8 Period of each stage in Two-stage CLC with Cu/CuO and Ni/NiO

Stage	Periods
OS	195
HROS	470
PS	30
RS	190
HRRS	30

Typically, only a few complete cycles are needed to approach cyclic steady-state operation. Figure 3.11 presents spatial temperature profiles across the reactor bed after four full cycles, specifically during RS, OS and HROS stages. Figure 3.12 shows how outlet gas temperatures evolve over multiple cycles.

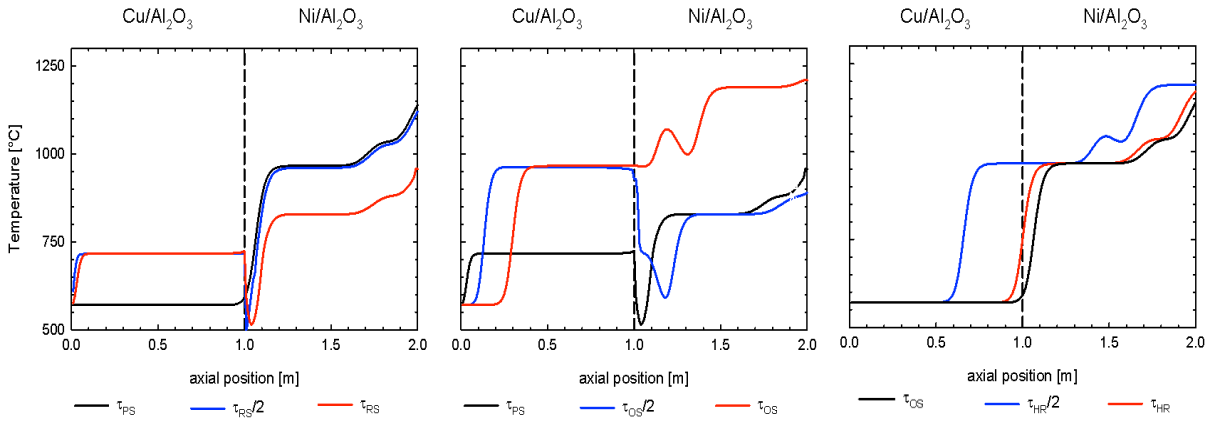

Figure 3.11 Spatial temperature profiles during RS (a), OS (b) and HROS (c) under steady-state cyclic operation.

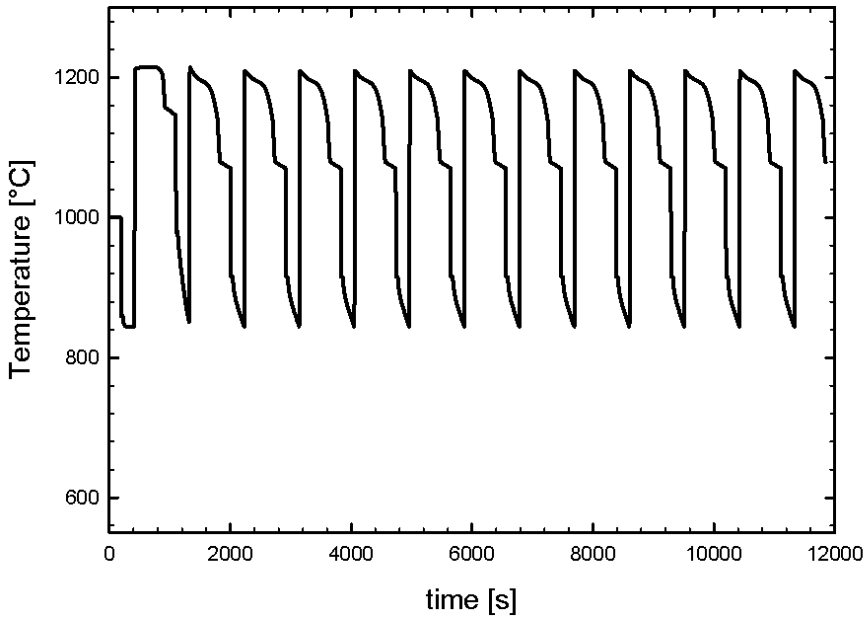

Figure 3.12 Monitored outlet gas temperatures over multiple cycles.

Notably, the maximum temperatures achieved at the outlet exceed those recorded for the one-stage reactor. Analyzing the timing information in Table 3.7, it becomes apparent that operating just two parallel reactors in this two-stage configuration is sufficient to ensure continuous production of high-temperature gas suitable for turbine expansion. This arrangement also maintains a pressure drop across each stage that is at least 15% lower than the inlet value [245]. Figure 3.13 shows the outlet temperatures obtained by mixing gas streams exiting reactors in HROS stage during steady-state operation. Importantly, operating two reactors in parallel under TS-CLC conditions yields two hot gas streams at nearly constant temperature (~1200 °C), suitable for turbine expansion. In addition, a stream rich in CO_2 can be produced after the condensation process.

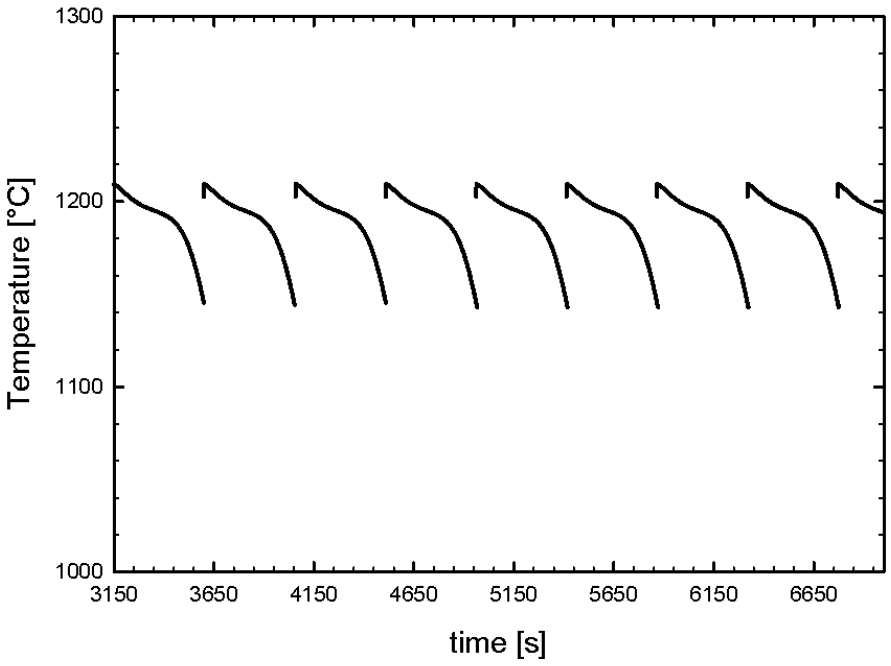

Figure 3.13 Outlet temperatures of mixed gas streams from reactors operating in HROS and RS stages.

To assess the performance of single- versus two-stage CLC systems, the electric power output via turbine expansion was computed following the approach in [249]:

$$P_{el} = \left(G_s A_r\right)\left(h_{in,HROS} - h_{out,HROS}\right)e_{tur} \tag{3.10}$$

Here e_{tur} = 0.87 [12] and the terms "in" and "out" represent the inlet (i.e., the outlet of the reactor network) and outlet states of the turbine system. Assuming an adiabatic, irreversible expansion down to atmospheric pressure, the outlet gas temperature was calculated using the following expression from [249]:

$$\left(\frac{T_{out}}{T_{in}}\right) = \left(\frac{P_{amb}}{P_{in}}\right)^{\frac{\gamma-1}{\gamma}} \tag{3.11}$$

In Equation (3.11), T_{in} is the average temperature during HROS, with values of 900 °C and 1170 °C used for the one-stage and TS-CLC systems, respectively. Pin values are reported in Tables 3.4 and 3.7. Based on Equation (3.10), with a methane flow rate of 0.072 $Nm^3 s^{-1}$, the electrical power output is 0.48 MW for the single-stage system and 0.68 MW for the TS-CLC system. This corresponds to a 40% increase in electrical power generation using TS-CLC under identical operating and geometric conditions.

Additionally, beyond the power improvement and reduced thermal cycling stress on the oxygen carriers, the required quantity of active material is significantly reduced. A comparison of Tables 3.4 and 3.7 reveals a reduction in active phase mass from 281 kg to 124 kg, more than halving the required amount.

3.5 Conclusions

This study introduces a numerical model simulating a fixed-bed Chemical Looping Combustion (CLC) reactor network for methane oxidation. The configuration includes a pair of reactors in series, each composed of two stages. The initial stage contains a Cu-based oxygen carrier, effective at relatively low temperatures, while the latter stage uses a Ni-based material, suited for high-temperature operation.

System performance was evaluated in terms of gas output composition and flow rate, cycle durations and power generation potential.

For equivalent reactor dimensions, the two-stage CLC system demonstrates comparable output flow rate and temperature to the single-stage design, while offering shorter cycle durations and requiring less active oxygen carrier material.

Moreover, fewer reactor units are needed in the two-stage network to continuously supply a turbine system. Due to the slightly higher outlet gas temperature from the TS-CLC setup, a 40% increase in generated electric power is achievable.

Finally, the two-stage configuration contributes to extended reactor lifespan, as the temperature fluctuations experienced by the bed material are less severe than those in single-stage systems.

Chapter 4 Innovative Pathways for Methane Production: Coupling Solar-Derived Hydrogen with Chemical Looping Gasification

4.1 Abstract

This study presents and numerically analyzes a novel process configuration aimed at enhancing the chemical storage of renewable energy. The approach relies on integrating hydrogen generation via water electrolysis with chemical looping gasification. At the heart of the system lies a fixed-bed chemical looping gasifier, which operates using various blends of biomass and Plastic Solid Waste (PSW), employing Fe_2O_3 as the oxygen carrier. Coupled to this is a methanation section composed of multiple adiabatic fixed-bed reactors arranged in series, each equipped with inter-stage cooling, condensation of water at the reactor outlets and product recycling. The methanation performance was assessed by assuming that the syngas produced in the gasification stage, after being purified and blended with hydrogen from an electrolysis cell (EC) array, reacts over a Ni/Al_2O_3 catalyst. The number of EC units required for hydrogen production was determined to maintain a steady H_2 output sufficient to achieve a 7:1:1 H_2:CO:CO_2 molar ratio at the methanation reactor inlet. Furthermore, the feasibility of employing this process as a renewable energy storage solution was evaluated under the assumption that all the input energy originates from sustainable sources such as solar panels or wind turbines.

4.2 Introduction

Gasification represents a highly efficient thermochemical pathway for converting biomass and various waste streams into a gaseous fuel, typically a hydrogen-rich synthesis gas (syngas) [285]. Among thermochemical technologies, gasification stands out for its flexibility, offering a syngas that can serve multiple applications, including combined heat and power (CHP) generation, liquid fuel production via the Fischer–Tropsch process and synthesis of gaseous fuels such as hydrogen

or synthetic natural gas (SNG) [286]. In contrast to biochemical methods, gasification also allows for the processing of inorganic and polymeric residues.

Each potential application of the resulting syngas demands a specific level of purification and a precise gas composition, particularly regarding the H_2:CO:CO_2 ratio [287]. Co-gasifying biomass with plastic waste is drawing increasing interest due to its ability to mitigate certain drawbacks inherent to biomass, such as seasonal supply variability and low energy density. Moreover, this strategy addresses common issues encountered during plastic-only gasification, including feeding difficulties and the excessive formation of solid carbonaceous residues [288].

Key to maximizing process efficiency are pre-treatment steps, optimal operating parameters and the integration of tar-reducing catalysts. Ramos et al. [289], for example, investigated catalytic co-gasification of biomass and plastic pellet blends in a fluidized bed reactor using air and steam with a Ni-based catalyst. Their findings highlighted that pelletizing enhances fuel uniformity and feeding stability. Although a hydrogen-rich syngas (approx. 32 vol% H_2) can be achieved, the process also results in increased tar formation and higher fines elutriation. They further reported that incorporating plastic into the biomass feed enhances hydrogen production while lowering CO concentration, effectively raising the H_2/CO ratio above 2, an ideal condition for Fischer–Tropsch synthesis.

Oxygen-enriched air and steam co-gasification of olive pits with synthetic polymers like PET or used tires has been shown to effectively tailor the composition of syngas for subsequent methanol synthesis [290]. To eliminate nitrogen dilution in the syngas, either steam or a steam–oxygen blend must be used. While steam-only gasification requires external heat input, using oxygen and steam allows partial oxidation, rendering the process autothermal [285].

To circumvent the challenges and costs linked to pure oxygen supply, Chemical Looping Gasification (CLG) has emerged as a promising alternative. In this configuration, two reactors,

the fuel reactor (FR) and air reactor (AR), operate in a cyclic mode. A metal oxide (MexOy), known as the oxygen carrier (OC), is reduced to MexOy-1 in the FR, releasing lattice oxygen to gasify the fuel and generate syngas. The reduced OC is subsequently regenerated in the AR by reoxidation with air [291]. This method eliminates the need for external oxygen by supplying oxygen via the OC lattice, while also facilitating tar cracking and increasing the H_2/CO ratio due to the OC's catalytic and oxidizing properties [291]. Furthermore, nitrogen dilution is entirely avoided, improving syngas quality for downstream synthesis processes.

Recent attention has focused on iron-based oxygen carriers, particularly CaO/Fe_2O_3 systems, due to their affordability, thermal resilience and favorable catalytic behavior, making them viable alternatives to nickel oxides for in-bed tar reforming [292,293].

One promising application of CLG is its integration with methanation units for synthetic methane production. Methanation has regained relevance due to its roles in biogas upgrading and power-to-gas systems. In the latter, excess renewable electricity is used to produce hydrogen, which is then combined with CO/CO_2 (from sources such as gasifiers, power plants, or industrial waste gases) to form methane. This synthetic methane can be injected into the existing natural gas grid for storage and distribution [294].

Various reactor designs for methanation have been explored in literature [295], including fixed-bed systems with multiple adiabatic stages, inter-stage cooling and product recycling (e.g., TREMP, Lurgi processes), as well as fluidized bed reactors (e.g., COMFLUX process) designed to mitigate the exothermic temperature spike of the Sabatier reaction and prevent catalyst deactivation [296]. The system analyzed in this study employs three adiabatic fixed-bed reactors in series, each with gas recycling and intercooling, to maintain optimal conditions for equilibrium conversion.

System performance was assessed using feedstock combinations of pine wood and Plastic Solid Waste (PSW), along with Fe_2O_3 as the oxygen carrier. After cleaning, the produced syngas is blended with high-purity hydrogen from an array of electrolysis cells (ECs) and directed to a methanation unit. The methanation reaction is catalyzed by Ni supported on alumina. Assuming all the electricity used in the process originates from renewable sources (e.g., photovoltaics or wind energy), the system demonstrates potential for functioning as an energy storage solution.

4.3 Mathematical Model

The conceptual representation of the proposed process flow, including the main reaction routes and the associated inlet and outlet streams, is illustrated in Figure 4.1. A more detailed depiction of the methanation reactor system (MR) is provided in Figure 4.2.

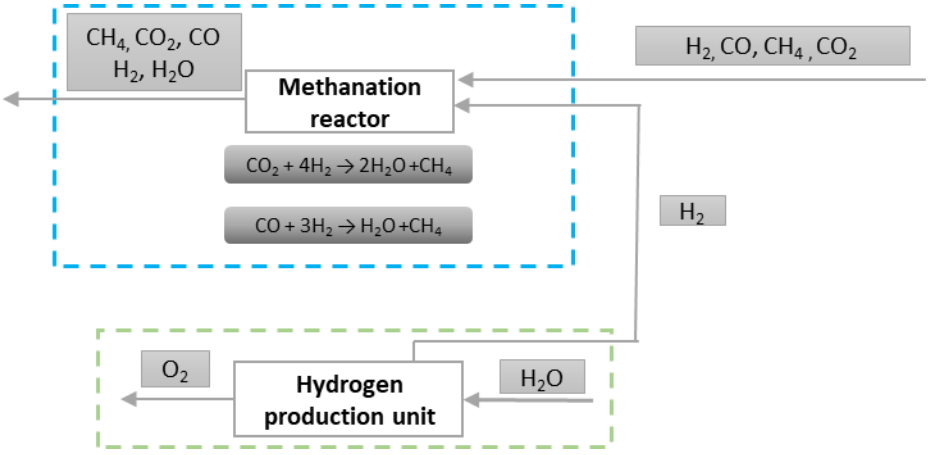

Figure 4.1 Conceptual diagram of the Solar-Derived Hydrogen with Chemical Looping Gasification process

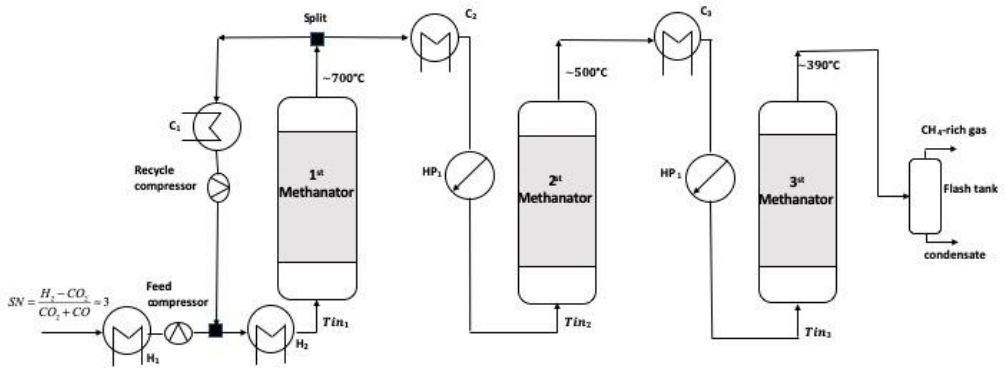

Figure 4.2 Adiabatic fixed-bed methanation layout with intermediate cooling and gas recycling; H1–H2: heaters, C1–C4: coolers, HP1–HP2: high-pressure boilers and three adiabatic methanation reactors. Further details are available in [259].

In order to achieve high reactant conversion efficiency, the pressure at the inlet of the methanation unit was fixed at 20 bar, as suggested in [295]. The recycle ratio was tuned between 1.5 and 2.0, favoring methane production while maintaining the reactor temperature below 650 °C, thus preventing catalyst sintering and carbon deposition [274,297].

A one-dimensional numerical model was employed to simulate the axial profiles of temperature and species concentration across each reactor [298]. The model assumes adiabatic operation and treats the reactor as pseudo-homogeneous, thereby disregarding inter- and intra-phase heat and mass transfer resistances. Compared to heterogeneous models, this approach simplifies the computations significantly [296]. Homogeneous properties are applied throughout and the catalyst surface is fully exposed to the bulk flow, further justifying the omission of particle-level heat/mass transfer resistances.

4.3.1 Kinetic Scheme

The material balances for each gas components (i=CH_4, CO, CO_2, H_2, H_2O) was written as:

$$\epsilon_g \frac{\partial c_i}{\partial t} = -u_{sg} \frac{\partial c_i}{\partial x} - \left(1 - \epsilon_g\right)\rho_c r_i \quad (4.1)$$

Here, x denotes the axial coordinate (m), ε_g the bed porosity, c the gas-phase concentration and ρ_c the catalyst density in the packed bed (kg_{cat}/m^3). The reaction rate r_i ($kmol/(kg_{cat}\, s)$) is determined by summing up the reaction rates of that species in all the reactions R_j (see Table 4.1) according to the stochiometric coefficients as follow:

$$r_i = \sum_{j=1}^{3} v_{i,j} R_j \quad (4.2)$$

The gas superficial velocity (u_{sg} m/s) has been calculated as follow:

$$u_{sg}(x,t) = \frac{PM_{in}}{PM} T(x,t) u_{sg,in} \quad (4.3)$$

where PM is the molecular weight ($kg/kmol$) and the subscript in represents inlet conditions.

Finally, the energy balances were written as:

$$\left(\epsilon_g \rho_g c_{pg} + \rho_c c_{pc}\left(1 - \epsilon_g\right)\right)\frac{\partial T}{\partial t} = -\rho_g c_{pg} u_{sg} \frac{\partial T}{\partial t} + \rho_c \sum_{j=1}^{3}\left(-\Delta H_{Rj}\right) r_i \quad (4.4)$$

where ρ and c_p ($J\, kg^{-1}\, K^{-1}$) represents the density and heat capacity for gas (g) and solid (c), respectively, while ΔH_j ($kJ{\cdot}mol^{-1}$) is the reaction enthalpy for j reaction.

4.3.2 Governing Equations

The full methanation reaction network is listed in Table 4.1.

Table 4.1 Methanation Reactions and Enthalpies

	Reaction	**ΔH (kJ/mol)**
R1	$CO + 3H_2 \rightleftharpoons CH_4 + H_2O$	–206
R2	$CO_2 + H_2 \rightleftharpoons CO + H_2O$	+41
R3	$CO_2 + 4H_2 \rightleftharpoons CH_4 + 2H_2O$	–165

Xu and Froment [299] suggested that kinetic rate models for syngas methanation over Ni-based catalyst can be expressed as described in Eqs. (4.5)–(4.8) in Table 4.2:

Table 4.2 Kinetic rate models for syngas methanation over Ni-based catalyst

Kinetic expression	Reaction	Equation
$R_1 = \frac{\frac{k_1}{P_{H2}^{2.5}}\left[P_{CH4}P_{H2O} - \frac{P_{CO}P_{H2}^3}{K_{eq,1}}\right]}{DEN^2}$	CO methanation	(4.5)
$R_2 = \frac{\frac{k_2}{P_{H2}}\left[P_{CO}P_{H2O} - \frac{P_{CO2}P_{H2}}{K_{eq,2}}\right]}{DEN^2}$	Water Gas Shift (WGS)	(4.6)
$R_3 = \frac{\frac{k_3}{P_{H2}^{3.5}}\left[P_{CH4}P_{H2}^2 - \frac{P_{CO2}P_{H2}^4}{K_{eq,3}}\right]}{DEN^2}$	CO_2 methanation	(4.7)

Where:

$$DEN = 1 + K_{CH4}P_{CH4} + K_{CO}P_{CO} + K_{H2}P_{H2} + K_{H2O}\frac{P_{H2O}}{P_{H2}} \quad (4.8)$$

In Eqs (4.5)-(4.8) R_i, $K_{eq,i}$ and k_i are the reaction rate, equilibrium constant and kinetic rate constant of reaction i (i = 1, 2, 3), respectively [264] while p_j and K_j are the partial pressure and adsorption constant of species j (j = CH_4, CO, H_2, H_2O), respectively. All the above kinetic parameters, depending on temperature, are given in Arrhenius-function form in Table 4.3.

Table 4.3 Kinetic parameters to calculate the reaction rates [264]

j	K_j	E_j	i	k_i	E_i
CH_4	$8.15 \cdot 10^{-4}$ bar^{-1}	-38.28 kJmol^{-1}	1	$5.17 \cdot 10^{15}\ \frac{\text{kmol bar}^{0.5}}{\text{kgcat h}}$	240.1 kJ mol^{-1}
CO	$10.1 \cdot 10^{-5}$ bar^{-1}	-70.65 kJmol^{-1}	2	$2.39 \cdot 10^{6}\ \frac{\text{kmol bar}^{0.5}}{\text{kgcat h}}$	67.13 kJ mol^{-1}
H_2	$7.5 \cdot 10^{-9}$ bar^{-1}	-82.9 kJmol^{-1}	3	$1.25 \cdot 10^{15}\ \frac{\text{kmol bar}^{0.5}}{\text{kgcat h}}$	243.9 kJ mol^{-1}
H_2O	2.1745 bar^{-1}	88.68 kJmol^{-1}			

The mathematical model Eqs (4.1)-(4.4) has been completed with the following boundary and initial conditions:

$$c_i(0,t) = c_{i,in}, c_i(x,0) = 0$$
$$T(0,t) = T_{in}, \;\; T(x,0) = T_0 \tag{4.9}$$

Inlet compositions for Eq. (4.9) are derived from the CLG output, summarized in Table 4.5, while operational parameters are listed in Table 4.4.

Table 4.4 Parameters used in the simulations

Parameter	**Value**
P bar	20.0
T_{in1}, °C	300
T_{in2}, °C	300
T_{in3}, °C	300
T_0 °C	400
V_1, m^3	7
V_2, m^3	16
V_3, m^3	35
c_{pc}, $J(kg\ K)^{-1}$	1100
ρ_c $kg\ m^{-3}$	2350
ε_g	0.4
u_{sg0}, $m \cdot s^{-1}$	1
R	[1.5-2]

The Method of Lines (MOL) was employed to solve the PDEs, using spatial discretization followed by time-domain integration [300].

Both reactions R1 and R3 are exothermic and involve significant volumetric shrinkage. Their high enthalpies of reaction (Table 4.1) pose a risk of excessive temperature rise under adiabatic

conditions, potentially resulting in catalyst degradation or carbon formation. To avoid catalyst loss and carbon deposition is therefore recommended to operate at temperature below 650° [286]. Therefore, in adiabatic methanation reactors operated under steady-state conditions, it is standard practice to implement product recirculation for cooling purposes [296]. For such systems, the recycle ratio, defined as the molar gas flow rate of the recycle stream relative to the reactor outlet, is commonly set between 0.5 and 3.0 [301]. The hydrogen production unit was modeled as a high-pressure polymer electrolyte membrane (HP-PEM) array. The number of cells was determined to ensure sufficient H_2 for full conversion of the CO/CO_2 stream exiting the gasifier.

The system's energy storage capability was evaluated via its the electric energy conversion efficiency (η_{ec}), defined as the ratio between the electric energy output and input of the system, was evaluated, according to:

$$\eta_{ec} = \frac{Q_{CH_4} \cdot LHV_{CH_4} \cdot CF \cdot \eta_e}{Electric\ energy\ input} \tag{4.10}$$

Where Q_{CH_4} is the methane flowrate, *LHV* its low heating value, *CF* the capacity factor (annual operation hours) and η_e is thermal-to-electric conversion efficiency.

The input data were taken from [291], who investigated co-gasification of pine wood and polyethylene using a CaO/Fe_2O_3 oxygen carrier. They observed a synergistic increase in hydrogen and syngas yields. Their gasification conditions were fixed: 850 °C, steam/fuel ratio of 1:4 and OC/fuel ratio of 1:4, with plastic content varying from 0–100%. Plastic content in the feed varies from 0% in Test 1 to 100% in Test 5.

Table 4.5 Gasification of PW and PE results

	1	2	3	4	5
% mol.	PW	PW-PE	PW-PE	PW-PE	PE
	(100 %wt)	(75-25 %wt)	(50-50 %wt)	(25-75 %wt)	(100 %wt)
H_2 (Nm^3/kg)	0.62	1.06	1.40	1.60	1.70
CO (Nm^3/kg)	0.34	0.5	0.6	0.63	0.61
CO_2 (Nm^3/kg)	0.20	0.13	0.11	0.08	0.05
CH_4 (Nm^3/kg)	0.09	0.09	0.08	0.15	0.15

The obtained syngas composition shows H_2:CO and H_2:CO_2 ratios below stoichiometric requirements (3:1 and 4:1, respectively) for the synthesis of methane, indicating a deficiency of hydrogen. In the proposed configuration, the additional hydrogen required for the methanation process comes from the array of high-pressure polymer electrolyte membrane cells (HP-PEM).

For system design, commercially available units with a nominal output of 100 Nm^3/h and an energy consumption of 46.6 kWh/kg H_2 were considered [296].

Operating parameters for the methanation unit were set to 20 bar and 673 K, aligned with the thermodynamic requirement to achieve >95% CO/CO_2 conversion, which is only feasible at high pressures and moderate temperatures (300–500 °C). To estimate system power output, η_e = 25% and CF = 6132.78 h/year were adopted.

4.4 Results and Discussion

Table 4.5 presents the evaluated data for five distinct scenarios, including cases with solely biomass or plastic as feedstocks for the gasification process. It is evident that decreasing the proportion of polyethylene (PE) in the feed leads to a reduction in the $CO:CO_2$ ratio at the inlet of the methanation section. Specifically, this ratio varies from 1.70 for 100% plastic waste (PW) to 12.20 for pure PE feed.

Based on the stoichiometries of reactions R1 and R3 in Table 4.1, the stoichiometric number (SN) for the input gas composition is defined as follows:

$$SN = \frac{mol_{H2} - mol_{CO2}}{mol_{CO} + mol_{CO2}} \tag{4.11}$$

For methane synthesis, an SN value of 3 is considered optimal [295] and the hydrogen requirement from the hydrogen production unit (HPU) has been calculated accordingly. The gas mixture exiting the CLG is blended with hydrogen produced by the HPU to achieve an SN of 3 before being directed to the methanation section, as illustrated in Figure 4.2. Figure 4.3 displays time-series data of gas molar fractions at the reactor outlets for a case where the CLG is fed entirely with PW (refer to column 1 in Table 4.5).

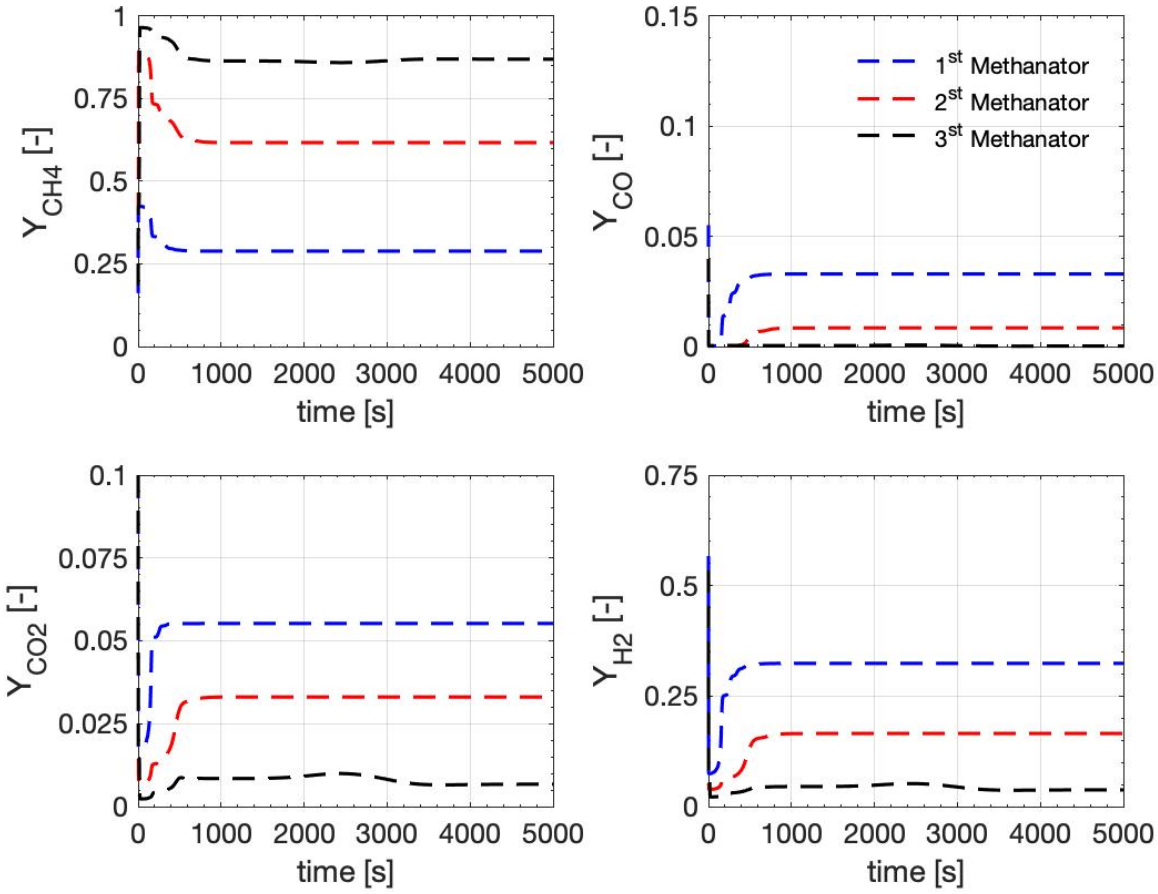

Figure 4.3 Gas molar fraction vs time at the exit of each reactor according to the legend for y_{CH4in}=0.037, y_{COin}=0.138, y_{CO2in}=0.086 and y_{H2in}=3y_{COin}+ 4y_{CO2in}, the other parameters are those reported in Table 4.4.

As expected, methane molar fraction increases progressively through the reactor series, while concentrations of all reactants decrease. At the outlet of the MRH_2 reactor, conversion levels of 0.97 for CO, 0.995 for CO_2 and 0.96 for H_2 are observed, yielding a methane molar fraction of 0.96 on a dry basis. The corresponding reactor exit temperatures under identical operating conditions are depicted in Figure 4.4. The adiabatic temperature rises for the first, second and final reactors are 380 °C, 250 °C and 80 °C, respectively.

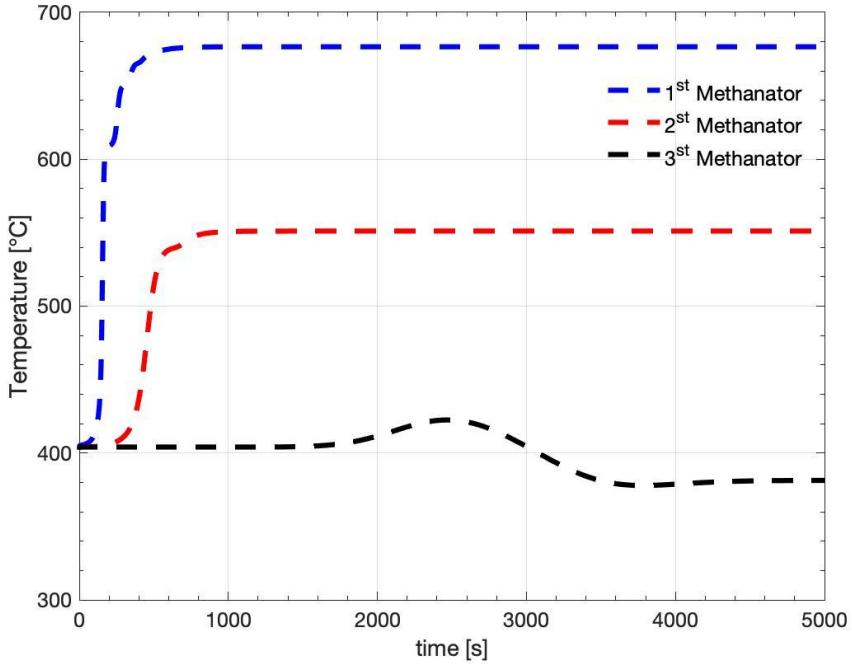

Figure 4.4 Gas temperatures at the outlet of each reactor, under the same initial gas compositions and operational parameters as in Figure 4.3.

To gain insight about the effectiveness of the displace of gas temperature in the direction of higher equilibrium conversion by intermediate cooling (Figure 4.2), the evolution of the H_2 conversion is illustrated in Figure 4.5 for 3 methanation reactors as well as the adiabatic temperature effect. Each diagonal line represents an adiabatic reactor (inlet and outlet conditions) and each horizontal line represents an intermediate cooling.

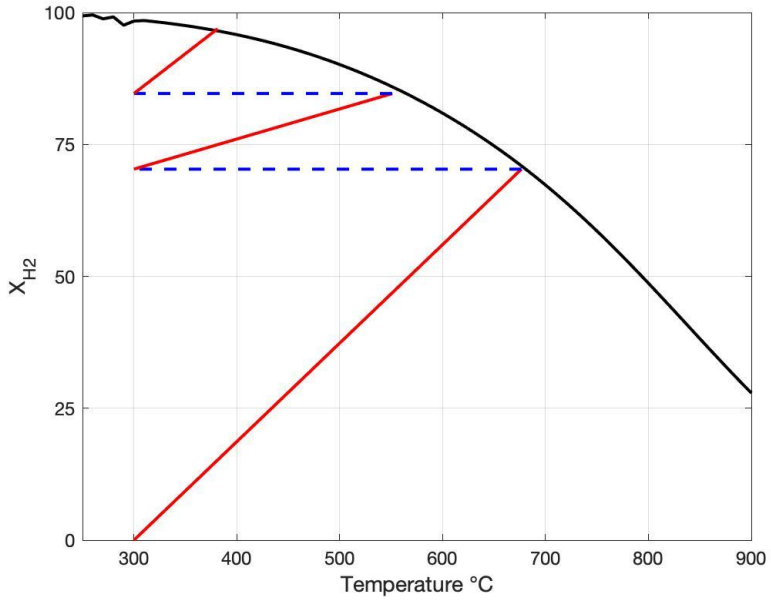

Figure 4.5 H_2 conversion as a function of temperature.

The equilibrium conversion curve in Figure 4.5 was determined by minimizing the Gibbs free energy [302]. Table 4.6 summarizes the methanation performance for various feed gas compositions derived from the CLG process (as presented in Table 4.5). Notably, water vapor concentrations remain low in the outlet stream due to condensation and removal after the first two reactors, which favors methane production. Methane concentrations range from 45% to 52.2% mol, translating to 94.7–95.6% on a dry basis.

The trends observed are mainly attributed to low CO concentrations and near-complete conversion of CO and H_2 [302]. CO_2 conversion is not complete and tends to decrease with increasing plastic content in the feed.

Table 4.6 Methanation unit results

	1	2	3	4	5
% mol	PW (100 %wt)	PW-PE (75-25 %wt)	PW-PE (50-50 %wt)	PW-PE (25-75 %wt)	PE (100 %wt)
CO	0.02	0.005	0.0065	0.022	0
CO_2	0.67	0.59	0.61	0.842	0.84
H_2	3.7	2.46	2.4	3.375	3.49
CH_4	86.9	85.53	86.9	87.50	87.3
H_2O	8.55	11.39	9.94	8.260	8.36
Dry basis					
CO	0.022	0.006	0.008	0.024	0
CO_2	0.73	0.67	0.83	0.918	0.92
H_2	4.12	2.78	3.4	3.67	3.75
CH_4	95.1	96.53	95.7	95.37	95.320
X_{H2}	97.42	98.8	98.37	98.	98.1
X_{CO2}	95.81	93.87	91.91	76.1	76
X_{CO}	99.92	99.85	99.984	99.95	100
$kmol_{H2}$ from HP-PEM	0.0535	0.0428	0.0375	0.0272	0.0147
R	1.5	1.5	1.8	1.8	2

As the CO/CO_2 ratio increases, the peak temperature attainable in the reactor also rises. To prevent surpassing the 700 °C limit, higher recycle ratios (R) are necessary: for the first two gas outputs in Table 4, R = 1.5; for outputs 3 and 4, R = 1.8; and for the final case, R = 2.

It is essential to note that the dry methane content achieved under this scheme is sufficient for injection into the natural gas grid in all cases except for pure biomass gasification. Some nations require a minimum methane content of over 95% for biogas injection into the grid [303].

Furthermore, the hydrogen requirement from the HP-PEM unit decreases as the proportion of plastic in the gasification feed increases.

4.5 Conclusions

This study introduces and analyzes a novel process configuration that integrates chemical looping co-gasification of biomass and plastic waste with solar hydrogen production and syngas methanation. The methanation section consists of a series of adiabatic fixed-bed reactors filled with Ni/Al_2O_3 catalyst, featuring inter-stage cooling, intermediate water removal and product recycling.

A range of recycle ratios were assessed to optimize conversion while mitigating thermal risks such as catalyst sintering or carbon deposition. Five syngas compositions, resulting from CLG-based co-gasification using a Ca-Fe oxygen carrier (from literature), were evaluated. Results demonstrate that, in all examined scenarios, the methane content on a dry basis meets or exceeds the thresholds for injection into natural gas distribution networks, thus avoiding the need for further upgrading.

Additionally, an increase in the plastic fraction of the feedstock correlates with a reduction in the amount of supplemental hydrogen needed from the HP-PEM system.

Chapter 5 Modelling and Parametric Evaluation of Reactors for CO_2 Methanation

5.1 Abstract

Methane production represents the core process step in the production of synthetic natural gas (SNG) from biomass. In this study, methanation is modeled as occurring in a series of adiabatic fixed-bed reactors, featuring intermediate cooling stages and partial recycling of the product stream. A comprehensive mathematical model has been established for this reactor configuration, designed to accurately reflect the key dynamics of the methanation process and support the identification of optimal strategies for industrial-scale application. Specifically, the model was used to investigate the effects of various CO/CO_2 feed ratios and different recycle fractions.

5.2 Introduction

The production of synthetic methane constitutes a pivotal step within the Power-to-Methane (PtM) paradigm, which couples renewable electricity with chemical energy storage through hydrogen and CO_2 conversion [304]. Methane, being fully compatible with the existing natural gas infrastructure, offers a practical medium for long-term energy storage and distribution, while also enabling the valorization of CO_2 from biogenic or industrial sources. This dual function of energy storage and carbon recycling makes PtM a particularly attractive solution in the context of renewable energy systems and climate mitigation strategies.

In this thesis, the methanation stage is implemented through a series of three adiabatic fixed-bed reactors arranged in series, equipped with inter-stage cooling and partial gas recycling, directly integrated with an upstream Chemical Looping Gasification (CLG) unit. The CLG-derived syngas is nitrogen-free, enriched in hydrogen and carbon monoxide and largely devoid of tar compounds. This composition is highly favorable for subsequent methanation, as it enhances equilibrium conversion and minimizes potential operational complications associated with nitrogen dilution or

tar-induced catalyst deactivation. Hydrogen supplementation is provided via high-pressure polymer electrolyte membrane (HP-PEM) electrolysis powered by renewable electricity, allowing fine-tuning of the feed stoichiometry to maintain optimal reaction conditions [291].

The purpose of this chapter is not to replicate the detailed numerical or kinetic modeling described in Chapter 4, but rather to provide a comprehensive discussion of reactor behavior, process integration and operational considerations. This work emphasizes how reactor configuration, feed composition, thermal management and gas recycling interact to achieve efficient methane synthesis, providing a bridge between the CLG unit and the downstream methanation system.

5.3 Methanation Reactor Configuration

The methanation process is implemented in a three-stage, adiabatic fixed-bed configuration, where inter-stage cooling and partial gas recycling are crucial to ensuring optimal thermal profiles, as described in Chapter 4. The exothermic Sabatier reaction generates significant heat, which, if not properly managed, can lead to catalyst sintering or carbon deposition [296]. By introducing intermediate cooling and recycling a fraction of the reactor effluent, the gas temperature is modulated along the reactor series, maintaining it within a safe operational range while simultaneously promoting chemical equilibrium conversion. This configuration allows the process to leverage both kinetic and thermodynamic advantages, achieving high methane yield without compromising catalyst longevity [296].

Integration with the CLG unit provides syngas with favorable H_2/CO ratios, free from nitrogen dilution, which is particularly beneficial for downstream methanation. The CLG unit converts biomass and plastic waste into a hydrogen-rich, tar-minimized syngas, with the oxygen supplied via a cyclically regenerated solid carrier (Fe_2O_3). The nitrogen-free nature of this syngas allows the reactors to operate closer to ideal stoichiometric ratios, reducing the need for excessive

hydrogen supplementation. Furthermore, hydrogen from renewable-powered electrolysis can be dynamically adjusted to compensate for variations in syngas composition, maintaining an optimal H_2:CO:CO_2 molar ratio for methane synthesis.

5.4 Technical and Scientific Considerations

The performance of methanation reactors depends on the combined effects of chemical kinetics, heat management, mass transfer and process integration. A staged configuration enables controlled temperature increases and promotes high reactant conversion. Gas recycling acts as both a temperature moderator and a means of maintaining feed composition uniformity across reactor stages. By carefully controlling the recycle fraction, the process can achieve near-complete conversion of CO and H_2, ensuring high methane yields without exceeding the critical temperature for Ni-based catalysts.

From a scientific perspective, this configuration illustrates several important principles. First, the adiabatic design coupled with inter-stage cooling effectively manages the exothermicity of the Sabatier reaction, which is essential to prevent hot spots that could accelerate catalyst deactivation. Second, the use of CLG syngas maximizes methane yield by providing a feed already enriched in hydrogen and carbon monoxide, thus enhancing equilibrium conversion and minimizing nitrogen dilution effects. Third, the dynamic integration with hydrogen electrolysis introduces flexibility, allowing the system to respond to fluctuations in renewable electricity availability and variations in feedstock composition. This integration demonstrates the potential of PtM systems to operate efficiently under variable and intermittent energy inputs, which is critical for large-scale renewable energy deployment.

Additionally, the interactions between feed composition, recycle ratios and operating conditions influence the temperature profile, equilibrium conversion and overall process efficiency. By

understanding these relationships, engineers can design industrial-scale methanation units that are both resilient and capable of maintaining high methane yields under varying operational scenarios.

5.5 Results and Discussion

In line with the chemical looping gasification framework established in Chapter 4, the methanation performance was analyzed considering feed gases that reflect different scenarios of carbon conversion and renewable energy integration. The first stream consisted of nearly pure CO_2 produced from a Chemical Looping Combustion (CLC) process [245], whereas the other two streams were syngas mixtures derived from the co-gasification of pinewood (PW) and polyethylene (PE) via the CLG process [291]. This approach ensures continuity between the gasification and methanation stages, demonstrating how the syngas quality and H_2/CO ratios generated in CLG directly influence downstream methane synthesis.

To achieve complete conversion of CO and CO_2 into methane, additional hydrogen is supplied by a high-pressure polymer electrolyte membrane (HP-PEM) electrolyzer [304], integrating renewable electricity into the Power-to-Methane (PtM) pathway. The hydrogen input is calibrated according to the stoichiometric requirements of the methanation reactions, expressed through the stoichiometric number (SN = 3). This ensures that the H_2 content in the feed matches the carbon oxide composition, enabling near-complete reaction while maintaining optimal thermal conditions.

The temporal evolution of methane formation and temperature along the three adiabatic fixed-bed methanation reactors illustrates the critical role of temperature management, a principle already highlighted in Chapter 4. Methane concentration increases progressively along the reactor sequence, while CO_2 and H_2 are simultaneously depleted. The configuration of inter-stage cooling

and partial gas recycling effectively moderates the exothermic reaction, preventing excessive temperature spikes and potential catalyst deactivation. This operational strategy allows the reactors to maintain thermal profiles that facilitate high equilibrium conversion and maximize methane yield.

Inter-stage cooling not only controls peak temperatures but also shifts the gas mixture toward favorable equilibrium conversion by removing water vapor and reducing the reaction enthalpy accumulation. Figure 5.1 shows H_2 conversion as a function of temperature, with adiabatic segments corresponding to the reaction paths and horizontal segments reflecting the cooling stages.

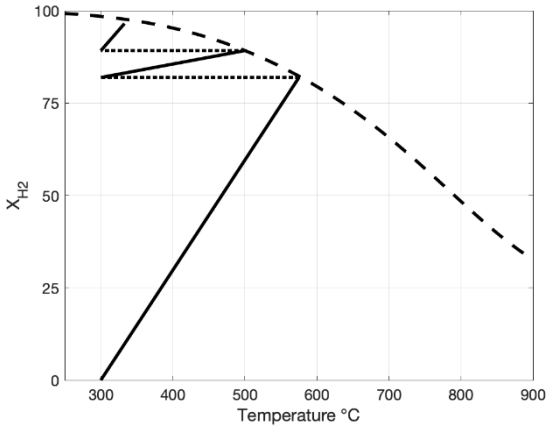

Figure 5.1 H_2 conversion vs. temperature profiles across three adiabatic reactors with intermediate cooling.

This approach mirrors the strategies applied in Chapter 4 for the CLG-based syngas, emphasizing the direct correlation between feed gas characteristics and methanation dynamics.

For syngas streams derived from CLG, inlet compositions were yCO = 0.247, yCO_2 = 0.1 and yH_2 = 0.637 for both PW and PE cases. The higher CO/CO_2 ratio in the PE feed leads to a more pronounced adiabatic temperature rise, requiring an increased recycle ratio to maintain reactor temperatures below 700 °C. Specifically, R = 2 is sufficient for PW syngas, while R = 2.5 is

required for PE syngas. These adjustments highlight the importance of feed composition and thermal management in PtM systems, confirming that the insights from CLG operation—such as oxygen carrier circulation, syngas conditioning and heat management—directly inform methanation reactor design.

Overall, this integrated approach demonstrates that coupling chemical looping gasification with renewable hydrogen production, inter-stage cooling and partial gas recycling allows near-complete conversion of CO and CO_2 into high-purity methane. Table 5.1 summarizes the dry-basis performance for the PW and PE feeds, confirming that the methane concentration meets or exceeds the 95% threshold required for natural gas grid injection, consistent with regulatory standards.

Table 5.1 Dry-basis results for the methanation unit

	PW	**PE**
CH_4	95.1	95.320
X_{H2}	97.42	98.1
X_{CO2}	95.81	76

5.6 Conlusions

A central aspect of this study is the seamless integration between the upstream CLG unit and the methanation reactors. The CLG unit delivers a syngas tailored for methanation: it is free from nitrogen dilution, rich in hydrogen and carbon monoxide and has low tar content. The nitrogen-free syngas improves the reactor's thermodynamic efficiency, while the hydrogen supplementation from electrolysis ensures the stoichiometric balance needed for high methane production. This integration exemplifies the broader PtM concept, where chemical looping gasification not only converts solid feedstocks into a usable gaseous stream but also creates a highly compatible interface for downstream energy storage applications.

By describing the methanation reactors in this context, Chapter 5 emphasizes process-level optimization and operational flexibility, linking technical reactor design with the upstream syngas characteristics and the overarching PtM strategy.

By directly linking the CLG-derived syngas characteristics from Chapter 4 with the methanation stage, it is evident that the reactor series can achieve high methane purity, near-complete H_2 and CO_2 conversion and stable adiabatic temperature profiles. The combined use of inter-stage cooling and gas recycling ensures operation within optimal thermal windows, minimizing risks of catalyst deactivation and carbon formation. These results demonstrate the technical feasibility of a fully integrated chemical looping gasification–methanation system powered by renewable hydrogen. The study highlights how insights from CLG operation—including syngas composition control, thermal management and oxygen carrier dynamics—provide a solid foundation for designing PtM systems capable of producing high-quality synthetic methane for energy storage and distribution.

Chapter 6 Conclusion and future direction

6.1 Conclusion

This thesis has presented a comprehensive investigation of advanced chemical looping systems and their integration into innovative energy and fuel production processes, with the overarching goal of improving efficiency, enhancing flexibility and enabling near-zero CO_2 emissions. The work is structured around three core studies, each addressing a specific technological challenge in the field of chemical looping and process integration.

In the first study, a novel two-stage fixed-bed Chemical Looping Combustion (CLC) reactor network was numerically modelled and analyzed for methane combustion. The proposed design employs a Cu-based oxygen carrier (OC) in the first stage, active at lower temperatures, followed by a Ni-based OC in the second stage, which is stable at higher temperatures. This arrangement strategically exploits the thermal reactivity profiles of the two carriers to enhance overall performance. Results showed that the two-stage configuration achieves comparable outlet temperatures and gas flow rates to a conventional single-stage reactor, but with shorter cycle times, lower total OC inventory and reduced thermal stress on materials, thereby extending reactor lifetime. Moreover, by operating at slightly higher average outlet temperatures, the system enables a 40% increase in electrical power output, making it particularly attractive for integration with turbine-based power generation systems. Additionally, fewer reactor units are required in parallel to guarantee continuous hot gas supply, which simplifies system complexity and lowers capital investment.

The second part of the thesis focused on the conceptual design and simulation of an integrated system that combines chemical looping co-gasification (CLC-G) of biomass and plastic waste with photovoltaic (PV)-driven hydrogen production and methanation of syngas. The system

addresses critical environmental and energy issues, such as plastic waste valorization, bioenergy conversion and synthetic natural gas (SNG) production. The methanation step was modelled as a network of adiabatic fixed-bed reactors filled with Ni-based catalysts, equipped with inter-cooling, product condensation and syngas recycle to optimize temperature profiles and prevent catalyst deactivation. Simulations demonstrated that high methane concentrations ($yCH_4 > 0.9$ on a dry basis) can be achieved across various syngas compositions obtained from biomass-plastic co-gasification, making the final product suitable for injection into the natural gas grid without the need for further upgrading. Notably, increasing the plastic fraction in the feedstock leads to a reduced demand for external hydrogen supply from high-pressure PEM electrolysis units, enhancing the overall energy efficiency and sustainability of the process.

In the third and final study, a detailed analysis of the methanation reactor train was conducted, examining both temperature evolution and conversion efficiency across each reactor stage. The model revealed excellent performance, with final H_2, CO and CO_2 conversions reaching 0.97, 0.995 and 0.96, respectively and methane concentrations exceeding 96% on a dry basis. These high conversion values indicate the effectiveness of the chosen design and operating conditions. The successful validation of the methanation process under various conditions confirms its potential for flexible synthetic methane production, especially when coupled with renewable hydrogen sources.

Overall, this thesis provides compelling evidence for the feasibility and effectiveness of advanced chemical looping systems in multiple decarbonization pathways. From efficient methane combustion and CO_2-free power generation to waste valorization and renewable fuel synthesis, the proposed solutions address several of the pressing challenges in sustainable energy. Furthermore, the research emphasizes the role of multi-functional reactors, smart

process integration and material-performance coupling in achieving energy efficiency and environmental goals.

6.2 Future Directions

Building upon the findings of this thesis, several avenues for future research are identified to further enhance the efficiency and applicability of chemical looping technologies.

Based on the results obtained, future research activities could focus on several complementary directions to enable the technological advancement, experimental validation and potential industrial scale-up of the proposed systems.

First, the promising performance of the two-stage CLC reactor in terms of thermal efficiency and operational flexibility calls for experimental validation at both laboratory and pilot scales. In this context, it will be essential to characterize the thermal behavior and cyclic stability of Cu- and Ni-based oxygen carriers, with particular attention to degradation mechanisms such as sintering and loss of activity over multiple redox cycles. Additionally, realistic operating conditions must be investigated to assess pressure drops, heat transfer efficiency and gas-solid contact dynamics. These studies will form the foundation for developing robust scale-up strategies and modular integration into reactor networks capable of ensuring continuous hot gas supply to power generation units.

Another key avenue for future work concerns the dynamic operation of the entire system in response to the increasing penetration of variable renewable energy sources. In particular, the methanation unit, which relies on hydrogen produced from photovoltaics or wind-powered electrolysis, must be designed to operate in a flexible, load-following mode. This necessitates transient simulations to model system behavior during start-up, shut-down and partial-load conditions, as well as techno-economic optimization of the electrolyzer-methanation coupling.

Advanced control strategies will be required to manage system inertia and ensure thermal stability under variable input conditions.

Regarding materials development, the performance of chemical looping systems is inherently linked to the properties of the oxygen carriers. Future studies could explore the synthesis and testing of doped mixed-metal oxides with enhanced redox kinetics, higher mechanical integrity and improved resistance to contaminants such as sulfur. In particular, perovskite-type and spinel-type structures, as well as dual-function materials capable of simultaneously facilitating gas separation and redox reactions, merit further attention. Characterization techniques (e.g., XRD, TGA, SEM) will be crucial for understanding the structural evolution and sintering behavior of these materials during long-term operation.

Although this work has focused on fixed-bed reactors, the implementation of fluidized bed technologies could offer significant advantages in terms of heat and mass transfer, temperature control and scalability. Future research could therefore include the development of detailed computational fluid dynamics (CFD) models to simulate the fluid-dynamic behavior and solid circulation, complemented by laboratory-scale experiments to measure reactivity, attrition resistance and kinetic parameters under realistic operating conditions.

Finally, the broader deployment of chemical looping systems must be supported by rigorous system-level analyses that consider both economic viability and environmental impact. Cost-benefit assessments comparing the capital and operational expenditures of the proposed configurations with competing technologies, such as post-combustion capture or electrolytic hydrogen, are essential. Furthermore, life cycle assessments should be performed to evaluate CO_2 abatement costs, energy return on investment (EROI) and overall greenhouse gas emissions. These findings could guide policy and regulatory frameworks, particularly in the

context of waste valorization and renewable synthetic methane production, aligning technological development with current decarbonization goals.

References

[1] D. Archer, "Fate of fossil fuel CO_2 in geologic time," *Journal of Geophysical Research: Oceans*, vol. 110, no. C9, 2005.

[2] H. Ritchie and M. Roser, "CO_2 and greenhouse gas emissions," *Our World in Data*, 2020. Available: https://ourworldindata.org/co2-and-greenhouse-gas-emissions

[3] International Energy Agency (IEA), *Global energy-related CO_2 emissions, 1900–2020*, 2020.

[4] C. Shearer, N. Mathew-Shah, L. Myllyvirta, A. Yu and T. Nace, *Boom and Bust 2019: Tracking the Global Coal Plant Pipeline*, Global Energy Monitor, 2019.

[5] B. Dudley, *BP Statistical Review of World Energy*, BP p.l.c., 2018.

[6] R. Malischek, *Tracking Clean Energy Progress*, International Energy Agency, 2019.

[7] M. Bui, C. S. Adjiman, A. Bardow, E. J. Anthony, A. Boston, S. Brown *et al*., "Carbon capture and storage (CCS): The way forward," *Energy & Environmental Science*, vol. 11, no. 5, pp. 1062–1176, 2018.

[8] T. Lockwood, "A comparative review of next-generation carbon capture technologies for coal-fired power plant," *Energy Procedia*, vol. 114, pp. 2658–2670, 2017.

[9] T. Wilberforce, A. Baroutaji, B. Soudan, A. Al Makky and A. G. Olabi, "Outlook of carbon capture technology and challenges," *Science of The Total Environment*, vol. 657, pp. 56–72, 2019.

[10] D. Y. C. Leung, G. Caramanna and M. M. Maroto-Valer, "An overview of current status of carbon dioxide capture and storage technologies," *Renewable and Sustainable Energy Reviews*, vol. 39, pp. 426–443, 2014.

[11] A. A. Olajire, "CO_2 capture and separation technologies for end-of-pipe applications – A review," *Energy*, vol. 35, no. 6, pp. 2610–2628, 2010.

[12] Global CCS Institute, *The Global Status of CCS: 2019*, 2019.

[13] B. P. Spigarelli and S. K. Kawatra, "Opportunities and challenges in carbon dioxide capture," *Journal of CO_2 Utilization*, vol. 1, pp. 69–87, 2013.

[14] Intergovernmental Panel on Climate Change (IPCC), *Carbon Dioxide Capture and Storage*. Cambridge, UK: Cambridge University Press, 2005.

[15] M. Schnellmann *et al.*, "Chemical looping technologies for CCS," in *Carbon Capture and Storage*, 2019, pp. 189–237.

[16] L.-S. Fan and F. Li, "Chemical looping technology and its fossil energy conversion applications," *Ind. Eng. Chem. Res.*, vol. 49, no. 21, pp. 10200–10211, 2010.

[17] B. Moghtaderi, "Application of chemical looping concept for air separation at high temperatures," *Energy Fuels*, vol. 24, no. 1, pp. 190–198, 2010.

[18] F.-X. Chiron and G. S. Patience, "Kinetics of mixed copper–iron based oxygen carriers for hydrogen production by chemical looping water splitting," *Int. J. Hydrogen Energy*, vol. 37, no. 14, pp. 10526–10538, 2012.

[19] X. Zhu *et al.*, "Chemical looping beyond combustion – A perspective," *Energy Environ. Sci.*, vol. 13, no. 3, pp. 772–804, 2020.

[20] S. Saqline, Z. Y. Chua and W. Liu, "Coupling chemical looping combustion of solid fuels with advanced steam cycles for CO_2 capture: A process modelling study," *Energy Convers. Manag.*, vol. 244, p. 114455, 2021.

[21] T. Mattison *et al.*, “Negative emissions of carbon dioxide through chemical-looping combustion (CLC) and gasification (CLG) using oxygen carriers based on manganese and iron,” *Mitig. Adapt. Strateg. Glob. Change*, vol. 25, pp. 497–517, 2020.

[22] T. Pröll and F. Zerobin, “Biomass-based negative emission technology options with combined heat and power generation,” *Mitig. Adapt. Strateg. Glob. Change*, vol. 24, pp. 1307–1324, 2019.

[23] B. Erlach, M. Schmidt and G. Tsatsaronis, “Comparison of carbon capture IGCC with pre-combustion decarbonisation and with chemical-looping combustion,” *Energy*, vol. 36, no. 6, pp. 3804–3815, 2011.

[24] S. Mukherjee, *et al.*, "Energy and exergy analysis of chemical looping combustion technology and comparison with pre-combustion and oxy-fuel combustion technologies for CO_2 capture," *J. Environ. Chem. Eng.*, vol. 3, no. 3, pp. 2104–2114, 2015.

[25] L. Zhu, P. Jiang and J. Fan, "Comparison of carbon capture IGCC with chemical-looping combustion and with calcium-looping process driven by coal for power generation," *Chem. Eng. Res. Des.*, vol. 104, pp. 110–124, 2015.

[26] G. D. Surywanshi, *et al.*, "4-E analyses of chemical looping combustion based subcritical, supercritical and ultra-supercritical coal-fired power plants," *Energy Convers. Manag.*, vol. 200, p. 112050, 2019.

[27] J. Adánez, *et al.*, "Progress in chemical-looping combustion and reforming technologies," *Prog. Energy Combust. Sci.*, vol. 38, no. 2, pp. 215–282, 2012.

[28] F. Emun, *et al.*, "Integrated gasification combined cycle (IGCC) process simulation and optimization," *Comput. Chem. Eng.*, vol. 34, no. 3, pp. 331–338, 2010.

[29] K. M. Merrett and K. J. Whitty, "Evaluation of coal conversion pathways in fluidized bed chemical looping combustion with oxygen uncoupling (CLOU)," *Fuel*, vol. 258, p. 116157, 2019.

[30] H. Jin and M. Ishida, "A new advanced IGCC power plant with chemical-looping combustion," in *Proc. of TAIES*, 1997.

[31] J. Adánez, *et al.*, "Use of Chemical-Looping processes for coal combustion with CO_2 capture," *Energy Procedia*, vol. 37, pp. 540–549, 2013.

[32] V. Spallina, *et al.*, "Reactor design and operation strategies for a large-scale packed-bed CLC power plant with coal syngas," *Int. J. Greenh. Gas Control*, vol. 36, pp. 34–50, 2015.

[33] T. Song and L. Shen, "Review of reactor for chemical looping combustion of solid fuels," *Int. J. Greenh. Gas Control*, vol. 76, pp. 92–110, 2018.

[34] H. Gu, *et al.*, "Chemical looping combustion of biomass/coal with natural iron ore as oxygen carrier in a continuous reactor," *Energy Fuels*, vol. 25, no. 1, pp. 446–455, 2011.

[35] S. Li and Y. Shen, "Numerical study of gas-solid flow behaviors in the air reactor of coal-direct chemical looping combustion with Geldart D particles," *Powder Technol.*, vol. 361, pp. 74–86, 2020.

[36] J. Adánez, *et al.*, "Selection of oxygen carriers for chemical-looping combustion," *Energy Fuels*, vol. 18, no. 2, pp. 371–377, 2004.

[37] L. Shen, *et al.*, "Chemical looping combustion of coal in interconnected fluidized beds," *Sci. China Ser. E: Technol. Sci.*, vol. 50, no. 2, pp. 230–236, 2007.

[38] M. Sorgenfrei and G. Tsatsaronis, "Design and evaluation of an IGCC power plant using iron-based syngas chemical-looping (SCL) combustion," *Appl. Energy*, vol. 113, pp. 1958–1964, 2014.

[39] D. Keairns, *et al.*, *Guidance for NETL's Oxycombustion R&D Program: Chemical Looping Combustion Reference Plant Designs and Sensitivity Studies*, NETL, 2014.

[40] J. Adánez, *et al.*, "Chemical looping combustion of solid fuels," *Prog. Energy Combust. Sci.*, vol. 65, pp. 6–66, 2018.

[41] C.-C. Cormos, A.-M. Cormos and L. Petrescu, "Assessment of chemical looping-based conceptual designs for high efficient hydrogen and power co-generation applied to gasification processes," *Chem. Eng. Res. Des.*, vol. 92, no. 4, pp. 741–751, 2014.

[42] H. Shijaz, *et al.*, "Analysis of integrated gasification combined cycle power plant incorporating chemical looping combustion for environment-friendly utilization of Indian coal," *Energy Convers. Manag.*, vol. 151, pp. 414–425, 2017.

[43] V. Spallina *et al.*, "Integration of coal gasification and packed bed CLC for high efficiency and near-zero emission power generation," *International Journal of Greenhouse Gas Control*, vol. 27, pp. 28–41, 2014.

[44] V. Spallina *et al.*, "Integration of coal gasification and packed bed CLC process for high efficiency and near-zero emission power generation," *Energy Procedia*, vol. 37, pp. 662–670, 2013.

[45] O. Authier and Y. Le Moullec, "Coal chemical-looping combustion for electricity generation: investigation for a 250 MWe power plant," *Energy Procedia*, vol. 37, pp. 588–597, 2013.

[46] M. Spinelli *et al.*, "Process integration of chemical looping combustion with oxygen uncoupling in a coal-fired power plant," *Energy*, vol. 103, pp. 646–659, 2016.

[47] S. Luo, L. Zeng and L. S. Fan, "Chemical looping technology: Oxygen carrier characteristics," *Annual Review of Chemical and Biomolecular Engineering*, vol. 6, pp. 53–75, 2015.

[48] Q. Fan *et al.*, "Breaking the stoichiometric limit in oxygen-carrying capacity of Fe-based oxygen carriers for chemical looping combustion using the Mg-Fe-O solid solution system," *ACS Sustainable Chemistry & Engineering*, vol. 10, no. 22, pp. 7242–7252, 2022.

[49] H. Zhao *et al.*, "Sol–gel-derived NiO/NiAl2O4 oxygen carriers for chemical-looping combustion by coal char," *Energy & Fuels*, vol. 22, no. 2, pp. 898–905, 2008.

[50] Q. Imtiaz *et al.*, "Synthesis of Cu-rich, Al2O3-stabilized oxygen carriers using a coprecipitation technique: redox and carbon formation characteristics," *Environmental Science & Technology*, vol. 46, no. 6, pp. 3561–3566, 2012.

[51] I. Adánez-Rubio *et al.*, "Evaluation of a spray-dried CuO/MgAl2O4 oxygen carrier for the chemical looping with oxygen uncoupling process," *Energy & Fuels*, vol. 26, no. 5, pp. 3069–3081, 2012.

[52] J. Huang *et al.*, "Phase interactions in Ni-Cu-Al2O3 mixed oxide oxygen carriers for chemical looping applications," *Applied Energy*, vol. 236, pp. 635–647, 2019.

[53] X. Chen *et al.*, "Flame spray pyrolysis synthesized Ni-doped Fe/Ce oxygen carriers for chemical looping dry reforming of methane," *Fuel*, vol. 343, p. 127913, 2023.

[54] A. Lyngfelt, "Oxygen carriers for chemical-looping combustion," in *Calcium and Chemical Looping Technology for Power Generation and Carbon Dioxide (CO2) Capture*, Elsevier, pp. 221–254, 2015.

[55] F. Liu *et al.*, "Bauxite waste with low Fe2O3 and high Na concentration as a promising oxygen carrier in chemical looping combustion," *International Journal of Energy Research*, vol. 44, no. 5, pp. 3790–3800, 2020.

[56] A. Lyngfelt *et al.*, "11,000 h of chemical-looping combustion operation—Where are we and where do we want to go?," *International Journal of Greenhouse Gas Control*, vol. 88, pp. 38–56, 2019.

[57] A. Lyngfelt, "Chemical looping combustion: Status and development challenges," *Energy & Fuels*, vol. 34, no. 8, pp. 9077–9093, 2020.

[58] M. Qasim *et al.*, "Recent advances and development of various oxygen carriers for the chemical looping combustion process: A review," *Industrial & Engineering Chemistry Research*, vol. 60, no. 24, pp. 8621–8641, 2021.

[59] S. Luo, L. Zeng and L.-S. Fan, "Chemical looping technology: Oxygen carrier characteristics," *Annual Review of Chemical and Biomolecular Engineering*, vol. 6, pp. 53–75, 2015.

[60] T. Mattisson, A. Järdnäs and A. Lyngfelt, "Reactivity of some metal oxides supported on alumina with alternating methane and oxygen application for chemical-looping combustion," *Energy & Fuels*, vol. 17, no. 3, pp. 643–651, 2003.

[61] P. Gayán *et al.*, "Effect of support on reactivity and selectivity of Ni-based oxygen carriers for chemical-looping combustion," *Fuel*, vol. 87, no. 12, pp. 2641–2650, 2008.

[62] C. Chung *et al.*, "Chemically and physically robust, commercially-viable iron-based composite oxygen carriers sustainable over 3000 redox cycles at high temperatures for chemical looping applications," *Energy & Environmental Science*, vol. 10, no. 11, pp. 2318–2323, 2017.

[63] T. Mattisson, M. Johansson and A. Lyngfelt, "The use of NiO as an oxygen carrier in chemical-looping combustion," *Fuel*, vol. 85, no. 5–6, pp. 736–747, 2006.

[64] C. Linderholm *et al.*, "160 h of chemical-looping combustion in a 10 kW reactor system with a NiO-based oxygen carrier," *International Journal of Greenhouse Gas Control*, vol. 2, no. 4, pp. 520–530, 2008.

[65] K. Idziak *et al.*, "Safety and environmental reasons for the use of Ni-, Co-, Cu-, Mn- and Fe-based oxygen carriers in CLC/CLOU applications: An overview," *Fuel*, vol. 268, p. 117245, 2020.

[66] P. Gayán *et al.*, "Effect of support on the behavior of Cu-based oxygen carriers during long-term CLC operation at temperatures above 1073 K," *Energy & Fuels*, vol. 25, no. 3, pp. 1316–1326, 2011.

[67] S. Penthor *et al.*, "Chemical-looping combustion of raw syngas from biomass steam gasification–Coupled operation of two dual fluidized bed pilot plants," *Fuel*, vol. 127, pp. 178–185, 2014.

[68] A. Abad *et al.*, "Chemical-looping combustion in a 300 W continuously operating reactor system using a manganese-based oxygen carrier," *Fuel*, vol. 85, no. 9, pp. 1174–1185, 2006.

[69] M. Rydén, A. Lyngfelt and T. Mattisson, "Combined manganese/iron oxides as oxygen carrier for chemical looping combustion with oxygen uncoupling (CLOU) in a circulating fluidized bed reactor system," *Energy Procedia*, vol. 4, pp. 341–348, 2011.

[70] H.-J. Ryu *et al.*, "Continuous operation of a 50 kWth chemical-looping combustor: long-term operation with Ni- and Co-based oxygen carrier particles," in *5th China-Korea Joint Workshop on Clean Energy Technology*, Qingdao University, China, 2004.

[71] Z.-P. Gao *et al.*, "Analysis of reactivity of Fe-based oxygen carrier with coal during chemical-looping combustion," *Journal of Fuel Chemistry and Technology*, vol. 37, no. 5, pp. 513–520, 2009.

[72] T. Mattisson *et al.*, "Innovative oxygen carriers uplifting chemical-looping combustion," *Energy Procedia*, vol. 63, pp. 113–130, 2014.

[73] Z. Di *et al.*, "Studies on steel slag as an oxygen carrier for chemical looping combustion," *Fuel*, vol. 226, pp. 618–626, 2018.

[74] C. Zhou *et al.*, "Integration options and economic analysis of an integrated chemical looping air separation process for oxy-fuel combustion," *Energy & Fuels*, vol. 30, no. 3, pp. 1741–1755, 2016.

[75] C. Y. Lau *et al.*, "Large scale in silico screening of materials for carbon capture through chemical looping," *Energy & Environmental Science*, vol. 10, no. 3, pp. 818–831, 2017.

[76] G. Luongo, F. Donat and C. R. Müller, "Structural and thermodynamic study of Ca A- or Co B-site substituted $SrFeO_{3-\delta}$ perovskites for low temperature chemical looping applications," *Physical Chemistry Chemical Physics*, vol. 22, no. 17, pp. 9272–9282, 2020.

[77] E. Marek *et al.*, "The use of strontium ferrite in chemical looping systems," *Applied Energy*, vol. 223, pp. 369–382, 2018.

[78] E. Krzystowczyk *et al.*, "Substituted $SrFeO_3$ as robust oxygen sorbents for thermochemical air separation: correlating redox performance with compositional and structural properties," *Physical Chemistry Chemical Physics*, vol. 22, no. 16, pp. 8924–8932, 2020.

[79] L. P. Teh, H. D. Setiabudi, S. N. Timmiati, M. A. A. Aziz, N. H. R. Annuar and N. N. Ruslan, "Recent progress in ceria-based catalysts for the dry reforming of methane: a review," *Chem. Eng. Sci.*, vol. 242, p. 116606, 2021.

[80] S. Alam, J. P. Kumar, K. Y. Rani and C. Sumana, "Comparative assessment of performances of different oxygen carriers in a chemical looping combustion coupled intensified reforming process through simulation study," *J. Clean. Prod.*, vol. 262, p. 121146, 2020.

[81] G. Hu, N. J. Nicholas, K. H. Smith, K. A. Mumford, S. E. Kentish and G. W. Stevens, "Carbon dioxide absorption into promoted potassium carbonate solutions: a review," *Int. J. Greenh. Gas Control*, vol. 53, pp. 28–40, 2016.

[82] S. A. Wassie, F. Gallucci, A. Zaabout, S. Cloete, S. Amini and M. van Sint Annaland, "Hydrogen production with integrated CO_2 capture in a novel gas switching reforming reactor: proof-of-concept," *Int. J. Hydrog. Energy*, vol. 42, pp. 14367–14379, 2017.

[83] S. van Renssen, “The hydrogen solution?,” *Nat. Clim. Change*, vol. 10, pp. 799–801, 2020.

[84] R. Chaubey, S. Sahu, O. O. James and S. Maity, “A review on development of industrial processes and emerging techniques for production of hydrogen from renewable and sustainable sources,” *Renew. Sustain. Energy Rev.*, vol. 23, pp. 443–462, 2013.

[85] N. A. Roslan, S. Z. Abidin, A. Ideris and D.-V. N. Vo, “A review on glycerol reforming processes over Ni-based catalyst for hydrogen and syngas productions,” *Int. J. Hydrog. Energy*, vol. 45, pp. 18466–18489, 2020.

[86] L. Barreto, A. Makihira and K. Riahi, “The hydrogen economy in the 21st century: a sustainable development scenario,” *Int. J. Hydrog. Energy*, vol. 28, pp. 267–284, 2003.

[87] S. Atilhan, S. Park, M. M. El-Halwagi, M. Atilhan, M. Moore and R. B. Nielsen, “Green hydrogen as an alternative fuel for the shipping industry,” *Curr. Opin. Chem. Eng.*, vol. 31, p. 100668, 2021.

[88] S. Z. Baykara, “Hydrogen: a brief overview on its sources, production and environmental impact,” *Int. J. Hydrog. Energy*, vol. 43, pp. 10605–10614, 2018.

[89] A. Iriondo, V. L. Barrio, J. F. Cambra, P. L. Arias, M. B. Güemez, R. M. Navarro, M. C. Sánchez-Sánchez and J. L. G. Fierro, “Hydrogen production from glycerol over nickel catalysts supported on Al_2O_3 modified by Mg, Zr, Ce or La,” *Top. Catal.*, vol. 49, pp. 46–58, 2008.

[90] M. Ji and J. Wang, “Review and comparison of various hydrogen production methods based on costs and life cycle impact assessment indicators,” *Int. J. Hydrog. Energy*, vol. 46, pp. 38612–38635, 2021.

[91] P. Wang, N. Means, D. Shekhawat, D. Berry and M. Massoudi, “Chemical-looping combustion and gasification of coals and oxygen carrier development: a brief review,” *Energies*, vol. 8, pp. 10605–10635, 2015.

[92] D. Lee, H. Nam, H. Kim, B. Hwang, J.-I. Baek and H.-J. Ryu, "Experimental screening of oxygen carrier for a pressurized chemical looping combustion," *Fuel Process. Technol.*, vol. 218, p. 106860, 2021.

[93] L.-S. Fan, L. Zeng and S. Luo, "Chemical-looping technology platform," *AIChE J.*, vol. 61, pp. 2–22, 2015.

[94] M. Osman, M. N. Khan, A. Zaabout, S. Cloete and S. Amini, "Review of pressurized chemical looping processes for power generation and chemical production with integrated CO_2 capture," *Fuel Process. Technol.*, vol. 214, p. 106684, 2021.

[95] L.-S. Fan, L. Zeng, W. Wang and S. Luo, "Chemical looping processes for CO_2 capture and carbonaceous fuel conversion—prospect and opportunity," *Energy Environ. Sci.*, vol. 5, pp. 7254–7280, 2012.

[96] L. F. de Diego, M. Ortiz, F. García-Labiano, J. Adánez, A. Abad and P. Gayán, "Hydrogen production by chemical-looping reforming in a circulating fluidized bed reactor using Ni-based oxygen carriers," *J. Power Sources*, vol. 192, pp. 27–34, 2009.

[97] E. García-Díez, F. García-Labiano, L. F. de Diego, A. Abad, P. Gayán and J. Adánez, "Autothermal chemical looping reforming process of different fossil liquid fuels," *Int. J. Hydrog. Energy*, vol. 42, pp. 13633–13640, 2017.

[98] D. Sastre, D. P. Serrano, P. Pizarro and J. M. Coronado, "Chemical insights on the activity of $La_{1-x}Sr_xFeO_3$ perovskites for chemical looping reforming of methane coupled with CO_2-splitting," *J. CO_2 Util.*, vol. 31, pp. 16–26, 2019.

[99] M. Meshksar, S. Daneshmand-Jahromi and M. R. Rahimpour, “Synthesis and characterization of cerium promoted Ni/SBA-16 oxygen carrier in cyclic chemical looping steam methane reforming,” *J. Taiwan Inst. Chem. Eng.*, vol. 76, pp. 73–82, 2017.

[100] I. Alirezaei, A. Hafizi and M. R. Rahimpour, “Syngas production in chemical looping reforming process over ZrO_2 promoted Mn-based catalyst,” *J. CO_2 Util.*, vol. 23, pp. 105–116, 2018.

[101] F. García-Labiano, E. García-Díez, L. F. de Diego, A. Serrano, A. Abad, P. Gayán, J. Adánez and J. A. C. Ruíz, “Syngas/H_2 production from bioethanol in a continuous chemical-looping reforming prototype,” *Fuel Process. Technol.*, vol. 137, pp. 24–30, 2015.

[102] A. J. Vizcaíno, P. Arena, G. Baronetti, A. Carrero, J. A. Calles, M. A. Laborde and N. Amadeo, “Ethanol steam reforming on Ni/Al_2O_3 catalysts: effect of Mg addition,” *Int. J. Hydrog. Energy*, vol. 33, pp. 3489–3492, 2008.

[103] Y. Ni, C. Wang, Y. Chen, X. Cai, B. Dou, H. Chen, Y. Xu, B. Jiang and K. Wang, “High purity hydrogen production from sorption enhanced chemical looping glycerol reforming: application of NiO-based oxygen transfer materials and potassium promoted Li_2ZrO_3 as CO_2 sorbent,” *Appl. Therm. Eng.*, vol. 124, pp. 454–465, 2017.

[104] Y. de Vos, M. Jacobs, P. van der Voort, I. van Driessche, F. Snijkers and A. Verberckmoes, “Development of stable oxygen carrier materials for chemical looping processes—a review,” *Catalysts*, vol. 10, p. 926, 2020.

[105] R. Porrazzo, G. White and R. Ocone, “Aspen plus simulations of fluidised beds for chemical looping combustion,” *Fuel*, vol. 136, pp. 46–56, 2014.

[106] X. Yin, L. Shen, S. Wang, B. Wang and C. Shen, “Double adjustment of Co and Sr in $LaMnO_{3+\delta}$ perovskite oxygen carriers for chemical looping steam methane reforming,” *Appl. Catal. B*, vol. 301, p. 120816, 2022.

[107] J. Adanez, A. Abad, F. Garcia-Labiano, P. Gayan and L. F. de Diego, “Progress in chemical-looping combustion and reforming technologies,” *Prog. Energy Combust. Sci.*, vol. 38, pp. 215–282, 2012.

[108] Y. Sun, J. Li and H. Li, “Core-shell-like Fe_2O_3/MgO oxygen carriers matched with fluidized bed reactor for chemical looping reforming,” *Chem. Eng. J.*, vol. 431, p. 134173, 2022.

[109] P. A. Argyris, C. de Leeuwe, S. Z. Abbas, A. Amieiro, S. Poultson, D. Wails and V. Spallina, “Chemical looping reforming for syngas generation at real process conditions in packed bed reactors: an experimental demonstration,” *Chem. Eng. J.*, vol. 435, p. 134883, 2022.

[110] Z. Sun, D. Y. Lu, R. T. Symonds and R. W. Hughes, “Chemical looping reforming of CH_4 in the presence of CO_2 using ilmenite ore and NiO-modified ilmenite ore oxygen carriers,” *Chem. Eng. J.*, vol. 401, p. 123481, 2020.

[111] T. Nimmas, S. Wongsakulphasatch, C. K. Cheng and S. Assabumrungrat, “Bi-metallic CuO-NiO based multifunctional material for hydrogen production from sorption-enhanced chemical looping autothermal reforming of ethanol,” *Chem. Eng. J.*, vol. 398, p. 125543, 2020.

[112] B. Dou, H. Zhang, G. Cui, Z. Wang, B. Jiang, K. Wang, H. Chen and Y. Xu, “Hydrogen production by sorption-enhanced chemical looping steam reforming of ethanol in an alternating fixed-bed reactor: sorbent to catalyst ratio dependencies,” *Energy Convers. Manage.*, vol. 155, pp. 243–252, 2018.

[113] J. Saupsor, C. Pei, H. Li, S. Wongsakulphasatch, P. Kim-Lohsoontorn, S. Ratchahat, W. Kiatkittipong, S. Assabumrungrat and J. Gong, “Bifunctional catalyst NiFe-MgAl for hydrogen production from chemical looping ethanol reforming,” *Energy Fuels*, vol. 35, pp. 11580–11592, 2021.

[114] Q. Zhang, B. Jiang, L. Li, K. Liu, N. He, J. Ma, X. Zhang and D. Tang, “Multifunctional Ni-based oxygen carrier for H_2 production by sorption enhanced chemical looping reforming of ethanol,” *Fuel Process. Technol.*, vol. 221, p. 106953, 2021.

[115] K. Wang, B. Dou, B. Jiang, Q. Zhang, M. Li, H. Chen and Y. Xu, “Effect of support on hydrogen production from chemical looping steam reforming of ethanol over Ni-based oxygen carriers,” *Int. J. Hydrog. Energy*, vol. 41, pp. 17334–17347, 2016.

[116] A. López Ortiz, M. Meléndez Zaragoza and V. Collins-Martínez, “Thermodynamic analysis of the ethanol chemical looping autothermal reforming with CO_2 capture,” *Int. J. Hydrog. Energy*, vol. 40, pp. 17180–17191, 2015.

[117] Q. Zhang, L. Li, B. Jiang, K. Wang, D. Tang and B. Dou, “An intelligent oxygen carrier of $La_2{-}xSrxNiO_4{-}\lambda$ for hydrogen production by chemical looping reforming of ethanol,” *Int. J. Hydrog. Energy*, vol. 42, pp. 17102–17111, 2017.

[118] K. Wang, B. Dou, B. Jiang, Y. Song, C. Zhang, Q. Zhang, H. Chen and Y. Xu, “Renewable hydrogen production from chemical looping steam reforming of ethanol using xCeNi/SBA-15 oxygen carriers in a fixed-bed reactor,” *Int. J. Hydrog. Energy*, vol. 41, pp. 12899–12909, 2016.

[119] C. Trevisanut, M. Mari, J. M. Millet and F. Cavani, “Chemical-loop reforming of ethanol over metal ferrites: an analysis of structural features affecting reactivity,” *Int. J. Hydrog. Energy*, vol. 40, pp. 5264–5271, 2015.

[120] S. Isarapakdeetham et al., “Hydrogen production via chemical looping steam reforming of ethanol by Ni-based oxygen carriers supported on CeO_2 and La_2O_3 promoted Al_2O_3,” *Int. J. Hydrog. Energy*, vol. 45, pp. 1477–1491, 2020.

[121] W. Wang, L. Fan and G. Wang, “Study on chemical looping reforming of ethanol (CLRE) for hydrogen production using $NiMn_2O_4$ spinel as oxygen carrier,” *J. Energy Inst.*, vol. 90, pp. 884–892, 2017.

[122] L. Li, Y. Song, B. Jiang, K. Wang and Q. Zhang, “A novel oxygen carrier for chemical looping reforming: laNiO_3 perovskite supported on montmorillonite,” *Energy*, vol. 131, pp. 58–66, 2017.

[123] D. Li et al., “Hydrotalcite-derived Co/Mg(Al)O as a stable and coke-resistant catalyst for low-temperature carbon dioxide reforming of methane,” *Appl. Catal. A*, vol. 552, pp. 21–29, 2018.

[124] B. Jiang et al., “Hydrogen production by chemical looping steam reforming of ethanol using NiO/montmorillonite oxygen carriers in a fixed-bed reactor,” *Chem. Eng. J.*, vol. 298, pp. 96–106, 2016.

[125] G. Yang, H. Yu, F. Peng, H. Wang, J. Yang and D. Xie, “Thermodynamic analysis of hydrogen generation via oxidative steam reforming of glycerol,” *Renew. Energy*, vol. 36, pp. 2120–2127, 2011.

[126] K. F. M. Elias, A. F. Lucrédio and E. M. Assaf, “Effect of CaO addition on acid properties of Ni–Ca/Al_2O_3 catalysts applied to ethanol steam reforming,” *Int. J. Hydrog. Energy*, vol. 38, pp. 4407–4417, 2013.

[127] C. Luo et al., “Hydrogen and syngas co-production by coupling of chemical looping water splitting and glycerol oxidation reforming using Ce–Ni modified Fe-based oxygen carriers,” *J. Clean. Prod.*, vol. 335, p. 130299, 2022.

[128] A. Delparish, S. Koc, B. S. Caglayan and A. K. Avci, “Oxidative steam reforming of glycerol to synthesis gas in a microchannel reactor,” *Catal. Today*, vol. 323, pp. 200–208, 2019.

[129] I. Adánez-Rubio, J. A. C. Ruiz, F. García-Labiano, L. F. de Diego and J. Adánez, "Use of bio-glycerol for the production of synthesis gas by chemical looping reforming," *Fuel*, vol. 288, p. 119578, 2021.

[130] J. C. de la Rosa, R. García, J. J. Delgado, J. L. Valverde and F. Dorado, "Hydrogen production by glycerol steam reforming over Cu–Ni supported catalysts," *Appl. Catal. B*, vol. 140–141, pp. 523–533, 2013.

[131] A. Uzun, M. S. Durap and H. Erdem-Senatalar, "Effects of MgO addition on Ni-based mesoporous catalysts in oxidative steam reforming of glycerol," *Appl. Catal. B*, vol. 180, pp. 586–596, 2016.

[132] D. R. Palo, R. A. Dagle and J. D. Holladay, "Methanol steam reforming for hydrogen production," *Appl. Catal. A*, vol. 271, pp. 35–45, 2004.

[133] Y. Matsumura et al., "Steam reforming of biomass: recent advances and future prospects," *Biomass Bioenergy*, vol. 29, pp. 245–266, 2005.

[134] S. S. R. Putra, A. J. E. Rettie and T. S. Miller, "Transition metal and metal oxide nanostructures for syngas generation by chemical looping reforming of methanol," *J. Energy Chem.*, vol. 78, pp. 327–345, 2023.

[135] A. J. Tasić, T. A. M. Kravanja, M. M. Novaković and A. D. Janković, "Methanol as an energy carrier: a review of the thermochemical conversion for hydrogen production," *Renew. Sustain. Energy Rev.*, vol. 139, p. 110711, 2021.

[136] S. S. R. Putra, A. J. E. Rettie and T. S. Miller, "Perovskite-based redox catalysts for chemical looping hydrogen production from methanol: the role of Sr substitution in $LaFeO_3$," *J. Energy Chem.*, vol. 73, pp. 544–553, 2022.

[137] S. M. A. Hosseini, M. H. Ahmadi, E. Sadeghzadeh and M. B. Shafii, “Hydrogen production by methanol steam reforming: a review,” *Int. J. Hydrog. Energy*, vol. 47, pp. 19999–20026, 2022.

[138] Y. Zhang, Q. Xia, Y. Xie and C. Tang, “Hydrogen production from chemical looping steam reforming of methanol over perovskite oxides,” *Appl. Catal. B*, vol. 256, p. 117864, 2019.

[139] A. Iulianelli, T. Longo, A. Basile and D. A. Pacheco Tanaka, “Methanol steam reforming for hydrogen generation via chemical looping membrane reactor: A comparison between packed and fluidized beds,” *Fuel Process. Technol.*, vol. 205, p. 106435, 2020.

[140] M. Irfan, M. A. H. F. Shaikh, M. T. Afzal and S. Sultana, “Chemical looping reforming of methanol for hydrogen production: a comprehensive review,” *Int. J. Hydrog. Energy*, vol. 48, pp. 33750–33771, 2023.

[141] C. Tang, Y. Zhang, Y. Xie, Q. Xia and X. Zhu, “Hydrogen production via chemical-looping steam reforming of methanol using perovskite-type $LaFeO_3$-based oxygen carriers,” *Int. J. Hydrog. Energy*, vol. 44, pp. 29343–29353, 2019.

[142] A. Basile, A. Iulianelli and F. Gallucci, Eds., *Current Trends and Future Developments on (Bio-) Membranes: Hydrogen Production and Purification*, Elsevier, 2020.

[143] M. A. G. Vallespir, L. M. Madeira and A. Mendes, “Water–gas shift reaction over $Cu–CeO_2/Al_2O_3$ catalysts: the effect of doping ceria with transition metals,” *Appl. Catal. B*, vol. 218, pp. 949–963, 2017.

[144] R. A. Dagle, A. D. Kovarik and Y. Wang, “A review on non-precious metal catalysts for low temperature water gas shift reaction,” *Catalysts*, vol. 7, no. 10, p. 312, 2017.

[145] A. Züttel, A. Remhof, A. Borgschulte and O. Friedrichs, “Hydrogen: the future energy carrier,” *Philos. Trans. R. Soc. A*, vol. 368, pp. 3329–3342, 2010.

[146] C. Song, “Global challenges and strategies for control, conversion and utilization of CO_2 for sustainable development involving energy, catalysis, adsorption and chemical processing,” *Catal. Today*, vol. 115, pp. 2–32, 2006.

[147] A. Freni, G. Calabrese and G. Cavallaro, “Production of hydrogen from ethanol by oxidative steam reforming over Co–Ni/ZrO_2 catalyst,” *Int. J. Hydrog. Energy*, vol. 35, pp. 12038–12045, 2010.

[148] D. Wang, A. Iulianelli, M. S. Irfan and A. Basile, “Methanol steam reforming for hydrogen production using Cu/ZnO/Al_2O_3 catalyst: from lab to industrial scale,” *Membranes*, vol. 10, no. 10, p. 285, 2020.

[149] S. M. A. Hosseini et al., “Chemical looping reforming of ethanol for hydrogen production over Cu–Ni/ZrO_2 catalysts,” *Int. J. Hydrog. Energy*, vol. 45, pp. 14447–14460, 2020.

[150] M. Rydén and M. Lyngfelt, “Hydrogen production with CO_2 capture by using chemical-looping reforming in a continuously operating packed-bed reactor,” *Fuel*, vol. 90, pp. 2716–2725, 2011.

[151] P. G. Smirniotis, “Hydrogen production via the water–gas shift reaction,” in *Comprehensive Renewable Energy*, vol. 5, Elsevier, pp. 153–178, 2012.

[152] J. Adánez, A. Abad, F. García-Labiano, P. Gayán and L. F. de Diego, “Progress in chemical-looping combustion and reforming technologies,” *Prog. Energy Combust. Sci.*, vol. 38, pp. 215–282, 2012.

[153] D. P. Serrano, J. Aguado and J. M. Escola, “Catalytic upgrading of bioethanol and other biomass-derived oxygenates to fuels and chemicals,” *Green Chem.*, vol. 15, pp. 2820–2839, 2013.

[154] M. M. Etim and A. A. Alhassan, “Catalytic reforming of bio-alcohols for hydrogen production: a review,” *Renew. Sustain. Energy Rev.*, vol. 116, p. 109404, 2019.

[155] D. Pakhare and J. Spivey, “A review of dry (CO_2) reforming of methane over noble metal catalysts,” *Chem. Soc. Rev.*, vol. 43, pp. 7813–7837, 2014.

[156] S. T. Oyama, Ed., *Mechanisms in Homogeneous and Heterogeneous Epoxidation Catalysis*, Elsevier, 2008.

[157] C. Wen and L. D. Hsiung, “Reaction mechanisms and kinetics for methane partial oxidation over Ni/Al_2O_3 catalyst,” *Ind. Eng. Chem. Res.*, vol. 37, pp. 3753–3760, 1998.

[158] K. Huang, J. B. Goodenough and Y. S. Meng, *Solid Oxide Fuel Cell Technology: Principles, Performance and Operations*, Elsevier, 2009.

[159] A. B. Stambouli and E. Traversa, “Solid oxide fuel cells (SOFCs): a review of an environmentally clean and efficient source of energy,” *Renew. Sustain. Energy Rev.*, vol. 6, pp. 433–455, 2002.

[160] Y. J. Leng, S. H. Chan, K. A. Khor and S. P. Jiang, “Development of Ni–YSZ cermet anode materials for solid oxide fuel cells,” *J. Power Sources*, vol. 122, pp. 173–180, 2003.

[161] B. C. H. Steele and A. Heinzel, “Materials for fuel-cell technologies,” *Nature*, vol. 414, pp. 345–352, 2001.

[162] S. McIntosh and R. J. Gorte, “Direct hydrocarbon solid oxide fuel cells,” *Chem. Rev.*, vol. 104, pp. 4845–4866, 2004.

[163] A. Orera and P. R. Slater, “New chemical systems for solid oxide fuel cells,” *Chem. Mater.*, vol. 22, pp. 675–690, 2010.

[164] P. A. Argyris, C. de Leeuwe, S. Z. Abbas, A. Amieiro, S. Poultson, D. Wails, e V. Spallina, "Chemical looping reforming for syngas generation at real process conditions in packed bed reactors: an experimental demonstration," *Chem. Eng. J.*, vol. 435, p. 134883, 2022.

[165] M. Martini, M. Druiff, M. van Sint Annaland, e F. Gallucci, "Experimental demonstration of the Ca-Cu looping process," *Chem. Eng. J.*, vol. 418, p. 129505, 2021.

[166] J. A. Medrano, I. Potdar, J. Melendez, V. Spallina, D. A. Pacheco-Tanaka, M. van Sint Annaland, e F. Gallucci, "The membrane-assisted chemical looping reforming concept for efficient H2 production with inherent CO2 capture: experimental demonstration and model validation," *Appl. Energy*, vol. 215, pp. 75–86, 2018.

[167] I. Iglesias, G. Baronetti, e F. Marino, "Ni/$Ce_{0.95}M_{0.05}O_{2-\delta}$ (M = Zr, Pr, La) for methane steam reforming at mild conditions," *Int. J. Hydrog. Energy*, vol. 42, pp. 29735–29744, 2017.

[168] L. Neal, A. Shafiefarhood, e F. Li, "Effect of core and shell compositions on MeOx@$LaySr_{1-y}FeO_3$ core–shell redox catalysts for chemical looping reforming of methane," *Appl. Energy*, vol. 157, pp. 391–398, 2015.

[169] L. Qin, M. Guo, Y. Liu, Z. Cheng, J. A. Fan, e L.-S. Fan, "Enhanced methane conversion in chemical looping partial oxidation systems using a copper doping modification," *Appl. Catal. B*, vol. 235, pp. 143–149, 2018.

[170] M. Usman, W. M. A. Wan Daud, e H. F. Abbas, "Dry reforming of methane: influence of process parameters—a review," *Renew. Sustain. Energy Rev.*, vol. 45, pp. 710–744, 2015.

[171] S. J. Hassani Rad, M. Haghighi, A. Alizadeh Eslami, F. Rahmani, e N. Rahemi, "Sol–gel vs. impregnation preparation of MgO and CeO_2 doped Ni/Al_2O_3 nanocatalysts used in dry reforming of methane: effect of process conditions, synthesis method and support composition," *Int. J. Hydrog. Energy*, vol. 41, pp. 5335–5350, 2016.

[172] R.-Y. Chein e W.-Y. Fung, "Syngas production via dry reforming of methane over CeO_2 modified Ni/Al_2O_3 catalysts," *Int. J. Hydrog. Energy*, vol. 44, pp. 14303–14315, 2019.

[173] M. Johansson, T. Mattisson, A. Lyngfelt, e A. Abad, "Using continuous and pulse experiments to compare two promising nickel-based oxygen carriers for use in chemical-looping technologies," *Fuel*, vol. 87, pp. 988–1001, 2008.

[174] M. K. Nikoo e N. A. S. Amin, "Thermodynamic analysis of carbon dioxide reforming of methane in view of solid carbon formation," *Fuel Process. Technol.*, vol. 92, pp. 678–691, 2011.

[175] J. Blamey et al., "The calcium looping cycle for large-scale CO_2 capture," *Prog. Energy Combust. Sci.*, vol. 36, no. 2, pp. 260–279, 2010.

[176] V. Manovic e E. J. Anthony, "Integration of calcium and chemical looping combustion using composite CaO/CuO-based materials," *Environ. Sci. Technol.*, vol. 45, no. 24, pp. 10750–10756, 2011.

[177] R. Chacartegui et al., "Thermochemical energy storage of concentrated solar power by integration of the calcium looping process and a CO_2 power cycle," *Appl. Energy*, vol. 173, pp. 589–605, 2016.

[178] R. Chang et al., "Synthetic solid oxide sorbents for CO_2 capture: state-of-the art and future perspectives," *J. Mater. Chem. A*, vol. 10, no. 4, pp. 1682–1705, 2022.

[179] B. Dou et al., "Solid sorbents for in-situ CO_2 removal during sorption-enhanced steam reforming process: A review," *Renew. Sustain. Energy Rev.*, vol. 53, pp. 536–546, 2016.

[180] C. S. Martavaltzi e A. A. Lemonidou, "Hydrogen production via sorption enhanced reforming of methane: Development of a novel hybrid material—reforming catalyst and CO_2 sorbent," *Chem. Eng. Sci.*, vol. 65, no. 14, pp. 4134–4140, 2010.

[181] M. Bhagiyalakshmi, J. Y. Lee, e H. T. Jang, "Synthesis of mesoporous magnesium oxide: its application to CO_2 chemisorption," *Int. J. Greenh. Gas Control*, vol. 4, no. 1, pp. 51–56, 2010.

[182] N. Rodríguez, M. Alonso, e J. Abanades, "Average activity of CaO particles in a calcium looping system," *Chem. Eng. J.*, vol. 156, no. 2, pp. 388–394, 2010.

[183] A. MacKenzie et al., "Economics of CO_2 capture using the calcium cycle with a pressurized fluidized bed combustor," *Energy Fuels*, vol. 21, no. 2, pp. 920–926, 2007.

[184] N. Wang et al., "Effects of preparation methods on the structure and property of Al-stabilized CaO-based sorbents for CO_2 capture," *Fuel Process. Technol.*, vol. 173, pp. 276–284, 2018.

[185] G. S. Grasa e J. C. Abanades, "CO_2 capture capacity of CaO in long series of carbonation/calcination cycles," *Ind. Eng. Chem. Res.*, vol. 45, no. 26, pp. 8846–8851, 2006.

[186] Z.-H. Li et al., "Effect of steam on CaO regeneration, carbonation and hydration reactions for CO_2 capture," *Fuel Process. Technol.*, vol. 151, pp. 101–106, 2016.

[187] V. Manovic et al., "Influence of calcination conditions on carrying capacity of CaO-based sorbent in CO_2 looping cycles," *Fuel*, vol. 88, no. 10, pp. 1893–1900, 2009.

[188] Y.-J. Heo e S.-J. Park, "Facile synthesis of MgO-modified carbon adsorbents with microwave-assisted methods: effect of MgO particles and porosities on CO_2 capture," *Sci. Rep.*, vol. 7, no. 1, p. 5653, 2017.

[189] M. T. Dunstan et al., "Reversible CO_2 absorption by the 6H Perovskite $Ba_4Sb_2O_9$," *Chem. Mater.*, vol. 25, no. 24, pp. 4881–4891, 2013.

[190] K. Wang et al., "Synthesis of highly effective stabilized CaO sorbents via a sacrificial N-doped carbon nanosheet template," *J. Mater. Chem. A*, vol. 7, no. 15, pp. 9173–9182, 2019.

[191] C. Luo et al., "Development and performance of CaO/La_2O_3 sorbents during calcium looping cycles for CO_2 capture," *Ind. Eng. Chem. Res.*, vol. 49, no. 22, pp. 11778–11784, 2010.

[192] J. Phromprasit, J. Powell, e S. Assabumrungrat, "Metals (Mg, Sr and Al) modified CaO based sorbent for CO_2 sorption/desorption stability in fixed bed reactor for high temperature application," *Chem. Eng. J.*, vol. 284, pp. 1212–1223, 2016.

[193] A. Dal Pozzo et al., "CO_2 uptake and cyclic stability of MgO-based CO_2 sorbents promoted with alkali metal nitrates and their eutectic mixtures," *ACS Appl. Energy Mater.*, vol. 2, no. 2, pp. 1295–1307, 2019.

[194] L. Li et al., "CO_2 capture over $K_2CO_3/MgO/Al_2O_3$ dry sorbent in a fluidized bed," *Energy Fuels*, vol. 25, no. 8, pp. 3835–3842, 2011.

[195] A. H. Soleimanisalim et al., "Pelletizing and coating of synthetic zirconia stabilized calcium-based sorbents for application in calcium looping CO_2 capture," *Ind. Eng. Chem. Res.*, vol. 56, no. 18, pp. 5395–5402, 2017.

[196] J. Chen et al., "Metal-oxide stabilized CaO/CuO composites for the integrated Ca/Cu looping process," *Chem. Eng. J.*, vol. 403, p. 126330, 2021.

[197] J. Yu et al., "CO_2 capture and separations using MOFs: computational and experimental studies," *Chem. Rev.*, vol. 117, no. 14, pp. 9674–9754, 2017.

[198] S. Kumar, R. Srivastava, e J. Koh, "Utilization of zeolites as CO_2 capturing agents: Advances and future perspectives," *J. CO_2 Util.*, vol. 41, p. 101251, 2020.

[199] Y. Gao et al., "Comprehensive investigation of CO_2 adsorption on Mg–Al–CO_3 LDH-derived mixed metal oxides," *J. Mater. Chem. A*, vol. 1, no. 41, pp. 12782–12790, 2013.

[200] M. T. Dunstan et al., "Large scale computational screening and experimental discovery of novel materials for high temperature CO_2 capture," *Energy Environ. Sci.*, vol. 9, no. 4, pp. 1346–1360, 2016.

[201] M. W. Gaultois et al., "Screening and characterization of ternary oxides for high-temperature carbon capture," *Chem. Mater.*, vol. 30, no. 8, pp. 2535–2543, 2018.

[202] D. Peltzer et al., "Characterization of potassium doped Li_2ZrO_3 based CO_2 sorbents: Stability properties and CO_2 desorption kinetics," *Chem. Eng. J.*, vol. 336, pp. 1–11, 2018.

[203] K. Gupta, S. Singh, e M. R. Rao, "Fast, reversible CO_2 capture in nanostructured Brownmillerite $CaFeO_{2.5}$," *Nano Energy*, vol. 11, pp. 146–153, 2015.

[204] S. Kumar e S. K. Saxena, "A comparative study of CO_2 sorption properties for different oxides," *Mater. Renew. Sustain. Energy*, vol. 3, p. 1–15, 2014.

[205] H. Gu et al., "Sr_2CeO_4 as a robust high temperature sorbent for CO_2 capture with near 100% sorbent conversion efficiency," *Chem. Eng. J.*, vol. 441, p. 135942, 2022.

[206] M. Zhao et al., "A novel calcium looping absorbent incorporated with polymorphic spacers for hydrogen production and CO_2 capture," *Energy Environ. Sci.*, vol. 7, no. 10, pp. 3291–3295, 2014.

[207] Y. Zhang et al., "Recent advances in lithium containing ceramic based sorbents for high-temperature CO_2 capture," *J. Mater. Chem. A*, vol. 7, no. 14, pp. 7962–8005, 2019.

[208] G. Ji et al., "Experimental study on CO_2 capture mechanisms using Na_2ZrO_3 sorbents synthesized by soft chemistry method," *Chem. Eng. J.*, vol. 313, pp. 646–654, 2017.

[209] I. Dincer, *Comprehensive Energy Systems*, Elsevier, 2018.

[210] A. Ohji and M. Haraguchi, "Steam turbine cycles and cycle design optimization: the Rankine cycle, thermal power cycles and IGCC power plants," in *Advances in Steam Turbines for Modern Power Plants*, Elsevier, pp. 11–40, 2017.

[211] M. T. Dunham and B. D. Iverson, "High-efficiency thermodynamic power cycles for concentrated solar power systems," *Renewable and Sustainable Energy Reviews*, vol. 30, pp. 758–770, 2014.

[212] B. Cuenot, "Gas turbines and engine simulations," in *Advances in Chemical Engineering*, Elsevier, pp. 273–385, 2016.

[213] J. Miller, "The combined cycle and variations that use HRSGs," in *Heat Recovery Steam Generator Technology*, Elsevier, pp. 17–43, 2017.

[214] J. Qi, H. Li, G. Chen, B. Yan, e J. Yao, “Thermodynamic modeling and performance analysis of chemical looping gasification combined with steam reforming for municipal solid waste: An Aspen Plus approach,” *Energy Convers. Manag.*, vol. 314, 118655, 2024.

[215] J. López van der Horst, M. F. Volpe Giangiordano, F. Suarez, F. M. Perez, M. N. Gatti, G. F. Santori, e F. Pompeo, “Influence of oxygen carrier on the autothermicity of a chemical-looping reforming process for hydrogen production,” *Reactions*, vol. 6, no. 1, p. 5, 2025.

[216] J. Cai, Y. Tang, J. Yang, F. Qin, Q. Liang, M. Fang, e S. Yao, “Simulation of thermodynamic systems in calcium-based chemical looping gasification of municipal solid waste for hydrogen-rich syngas production,” *Process Saf. Environ. Prot*., vol. 2024, pp. 335–352, 2024.

[217] A. Abdalla, A. Farooqui, M. Mohamedali e N. Mahinpey, “Copper-based chemical looping air separation process: Thermodynamics, kinetic modeling, and simulation of the fluidized beds,” *Sep. Purif. Technol.*, vol. 335, 126149, 2024.

[218] Damköhler, G., *Über den Einfluß der Dissipation der Reaktionswärme auf den Verlauf chemischer Reaktionen in Rohrreaktoren*. *Z. Elektrochem.*, 42, 846–860, 1936.

[219] P. V. Danckwerts, “Continuous flow systems. Distribution of residence times,” *Chem. Eng. Sci.*, vol. 1, pp. 1–13, 1953.

[220] V. Hlavacek e J. Vortuba, “Steady-state operation of fixed-bed reactors and monolithic structures,” in *Chemical Reaction Engineering, Advances in Chemistry Series*, American Chemical Society, New York, p. 314, 1977.

[221] G. F. Froment e K. B. Bischoff, *Chemical Reaction Analysis and Design*, John Wiley, 1979.

[222] H. A. Deans e L. Lapidus, “A computational model for predicting and correlating the behavior of fixed-bed reactors: I. Derivation of model for nonreactive systems,” *AIChE J.*, vol. 6, pp. 657–663, 1960.

[223] M. L. McGuire e L. Lapidus, “On the stability of a detailed packed-bed reactor,” *AIChE J.*, vol. 11, pp. 84–95, 1965.

[224] J. W. Vanderveen, D. Luss e N. R. Amundson, “Stability of adiabatic packed bed reactors: effect of flow variations and coupling between the particles,” *AIChE J.*, vol. 14, pp. 636–643, 1968.

[225] Macdonald, I. F., El-Sayed, M. S., Mow, K. and Duillien, F. A. L., Flow through porous media-the ergun equation revised. *Ind. Eng. Chem. Fundam.*, vol. 18, 199-208, 1979

[226] Handley, D. and Heggs, P.J ., Momentum and heat transfer mechanisms in regular shaped packings. Trans. Instn. Chem. Engrs., 46-T251, 1968,

[227] Hicks, R.E., Pressure drop in packed beds of spheres. *Ind. Eng. Chem. Fund.*, 9, 500-502, 1970.

[228] Leva, M.,Weintraub, M., Grummer, M. and Clark, E. L., Cooling of gases through packed tubes. *Ind. Eng Chem.*, 40(4), 747-752, 1948.

[229] Pan, C., Zhang, L., Yang, J., Hu, H., Numerical model of methanol synthesis process by CO_2 hydrogenation in compact reactor with microchannels. *SSRN*, January 2025.

[230] M. Dai, T. Guo, X. Hu, J. Ma, e Q. Guo, "Simulation of a 1MWth biomass chemical looping gasification process based on kinetic and pyrolysis models," *Int. J. Hydrogen Energy*, vol. 80, pp. 298–307, 2024.

[231] G. Chen, K. Yang, X. Sun, X. Zhu, W. Chen, D. Hou, Z. Cheng, e B. Yan, "Advances in biomass chemical looping combustion technology: Process control and comprehensive evaluation," *J. Environ. Chem. Eng*., vol. 13, 118142, 2025.

[232] Z. Gao, D. Wu, F. Yin, L. Sun, D. Zeng, R. Xiao, "Thermodynamic and kinetic analysis on the biomass syngas fueled chemical looping hydrogen generation process in fixed bed reactor," *Energy*, vol. 298, 120710, 2024.

[233] L. Qin, S. Zhu, W. Qin, B. Zhao, W. Chen, E. N. Asamoah, e J. Han, "H2-rich syngas generated from forestry waste gasification by recycling hot blast furnace gas," *J. Clean. Prod.*, vol. 448, 141671, 2024.

[234] J. Rogelj et al., "Paris Agreement climate proposal need a boost to keep warming well below 2 °C," *Nature*, vol. 534, no. 7609, pp. 631–639, 2016.

[235] International Energy Agency (IEA), *CO_2 Emissions from Fuel Combustion: Overview*, OECD Publishing, Paris, 2017.

[236] M. M. Hossain and H. I. de Lasa, "Chemical-looping combustion (CLC) for inherent CO_2 separations—a review," *Chemical Engineering Science*, vol. 63, pp. 4433–4451, 2008.

[237] J. Adánez and A. Abad, "Chemical-looping combustion: Status and research needs," *Proceedings of the Combustion Institute*, vol. 37, no. 4, pp. 1–15, 2018.

[238] C. A. del Pozo et al., "The potential of chemical looping combustion using the gas switching concept to eliminate the energy penalty of CO_2 capture," *Journal of Greenhouse Gas Control*, vol. 83, pp. 265–278, 2019.

[239] T. Song et al., "Nitrogen transfer of fuel-N in chemical looping combustion," *Combustion and Flame*, vol. 159, pp. 1286–1295, 2012.

[240] J. Li et al., "CO_2 capture with chemical looping combustion of gaseous fuels: An overview," *Energy & Fuels*, vol. 31, no. 4, pp. 3475–3524, 2017.

[241] S. Noorman, M. V. S. Annaland and H. Kuipers, "Packed bed reactor technology for chemical-looping combustion," *Industrial & Engineering Chemistry Research*, vol. 46, no. 12, pp. 4212–4220, 2007.

[242] J. R. Fernández, J. C. Abanades, R. Murillo and G. Grasa, "Conceptual design of a hydrogen production process from natural gas with CO_2 capture using a Ca–Cu chemical loop," *International Journal of Greenhouse Gas Control*, vol. 6, pp. 126–141, 2012.

[243] H. P. Hamers et al., "Energy analysis of two stage packed-bed chemical looping combustion configurations for integrated gasification combined cycles," *Energy*, vol. 85, pp. 489–502, 2015.

[244] S. Noorman, M. M. van Sint Annaland and J. A. M. Huipers, "Experimental validation of packed bed chemical-looping combustion," *Chemical Engineering Science*, vol. 65, pp. 92–97, 2010.

[245] G. Diglio, P. Bareschino, E. Mancusi and F. Pepe, "Techno-economic evaluation of a small-scale power generation unit based on a chemical looping combustion process in fixed bed reactor network," *Industrial & Engineering Chemistry Research*, vol. 57, no. 33, pp. 11299–11311, 2018.

[246] A. Adánez, F. Garcia-Labiano, P. Gayan and L. De Diego, "Progress in chemical looping combustion and reforming technologies," *Progress in Energy and Combustion Science*, vol. 38, no. 2, pp. 215–282, 2012.

[247] E. Jerndal, T. Mattisson and A. Lyngfelt, "Thermal analysis of chemical-looping combustion," *Chemical Engineering Research and Design*, vol. 84, no. A9, pp. 795–806, 2006.

[248] M. Johansson, T. Mattisson and A. Lyngfelt, "Investigation of Mn_3O_4 with stabilized ZrO_2 for chemical-looping combustion," *Chemical Engineering Research and Design*, vol. 84, no. A9, pp. 807–818, 2006.

[249] A. Fossdal et al., "Study of inexpensive oxygen carriers for chemical looping combustion," *International Journal of Greenhouse Gas Control*, vol. 5, pp. 483–488, 2011.

[250] A. Abad, T. Mattisson, A. Lyngfelt and M. Ryden, "Chemical-looping combustion in a 300 W continuously operating reactor system using a manganese-based oxygen carrier," *Fuel*, vol. 85, pp. 1174–1185, 2006.

[251] T. Mattisson et al., "Influence of heat treatment on manganese ores as oxygen carriers," *International Journal of Greenhouse Gas Control*, vol. 87, pp. 238–245, 2019.

[252] M. Johansson, T. Mattisson and A. Lyngfelt, "Comparison of oxygen carriers for chemical-looping combustion," *Thermal Science*, vol. 10, no. 3, pp. 93–107, 2006.

[253] L. Silvester et al., "NiO supported on Al_2O_3 and ZrO_2 oxygen carriers for chemical looping steam methane reforming," *International Journal of Hydrogen Energy*, vol. 40, pp. 7490–7501, 2015.

[254] G. Diglio, P. Bareschino, E. Mancusi and F. Pepe, "Numerical assessment of the effects of carbon deposition and oxidation on chemical looping combustion in a packed-bed reactor," *Chemical Engineering Science*, vol. 160, pp. 86–96, 2017.

[255] H. P. Hamers et al., "A novel reactor configuration for packed bed chemical-looping combustion of syngas," *International Journal of Greenhouse Gas Control*, vol. 16, pp. 1–12, 2013.

[256] R. F. Kooiman, H. P. Hamers, F. Gallucci and M. Van Sint Annaland, "Experimental demonstration of two-stage packed bed chemical-looping combustion using syngas with CuO/Al_2O_3 and $NiO/CaAl_2O_4$ as oxygen carriers," *Industrial & Engineering Chemistry Research*, vol. 54, no. 7, pp. 2001–2011, 2015.

[257] C. Dueso, M. Ortiz, A. Abad, F. García-Labiano, L. F. de Diego, P. Gayán, and J. Adánez, "Reduction and oxidation kinetics of nickel-based oxygen-carriers for chemical-looping combustion and chemical-looping reforming," *Chem. Eng. J.*, vol. 188, pp. 142–154, 2012.

[258] L. Han, X. Wang, and L. Fan, "Comparison of Cu-, Fe-, and Ni-based oxygen carriers for chemical-looping combustion," *Energy Fuels*, vol. 27, no. 4, pp. 1845–1854, 2013.

[259] M. C. Iliuta, R. Tahoces, K. Dam-Johansen, and A. D. Jensen, "Modeling of chemical-looping combustion process of methane with nickel-based oxygen carrier," *Energy Fuels*, vol. 24, no. 2, pp. 1187–1197, 2010.

[260] J. Adánez, A. Abad, F. García-Labiano, P. Gayán, and L. F. de Diego, "Reduction and oxidation kinetics of nickel-based oxygen-carriers for chemical-looping combustion and chemical-looping reforming," *Energy Fuels*, vol. 18, no. 2, pp. 371–377, 2004.

[261] Adánez-Rubio, A. Abad, P. Gayán, L. F. de Diego, F. García-Labiano, and J. Adánez, "Effect of gas composition in Chemical-Looping Combustion with copper-based oxygen carriers: Fate of sulphur," *Int. J. Greenh. Gas Cont.*, vol. 6, pp. 156–166, 2012.

[262] J. Adánez, A. Abad, F. García-Labiano, L. F. de Diego, P. Gayán, and A. Lyngfelt, "Comparison of nickel- and iron-based oxygen carriers in chemical-looping combustion for CO_2 capture in power generation," *Energy Environ. Sci.*, vol. 3, no. 11, pp. 1609–1619, 2010.

[263] T. Mattisson, M. Johansson, and A. Lyngfelt, “Comparison of iron-, nickel-, copper- and manganese-based oxygen carriers for chemical-looping combustion,” *Fuel*, vol. 78, no. 2, pp. 195–213, 2001.

[264] F. García-Labiano, L. F. de Diego, J. Adánez, P. Gayán, and A. Abad, “Development of Cu-based oxygen carriers for chemical-looping combustion,” *Fuel*, vol. 83, no. 13, pp. 1749–1757, 2004.

[265] P. Gayán, A. Abad, L. F. de Diego, F. García-Labiano, and J. Adánez, “Investigation of the performance of a copper based oxygen carrier for chemical looping combustion in a 120 kW pilot plant for gaseous fuels,” *Fuel*, vol. 89, no. 5, pp. 1249–1259, 2010.

[266] H. Leion, A. Lyngfelt, M. Johansson, E. Jerndal, and T. Mattisson, “Characterization of chemical looping combustion of coal in a 1 kWth reactor with a nickel-based oxygen carrier,” *Fuel*, vol. 88, no. 11, pp. 1945–1954, 2009.

[267] J. Adánez, P. Gayán, J. Celaya, L. F. de Diego, F. García-Labiano, and A. Abad, “Effect of pressure on the behavior of copper-, iron-, and nickel-based oxygen carriers for Chemical-Looping Combustion,” *Energy Fuels*, vol. 20, no. 5, pp. 1845–1854, 2006.

[268] J. Adánez, A. Abad, F. García-Labiano, P. Gayán, and L. F. de Diego, “Comparison of iron-, nickel-, copper- and manganese-based oxygen carriers for chemical-looping combustion,” *Fuel*, vol. 87, no. 10–11, pp. 949–961, 2008.

[269] E. Jerndal, T. Mattisson, and A. Lyngfelt, “Experiments on chemical looping combustion of coal with a NiO based oxygen carrier,” *Fuel*, vol. 85, no. 10–11, pp. 1631–1641, 2006.

[270] Q. Zafar, A. Abad, T. Mattisson, B. Gevert, and M. Strand, “Using continuous and pulse experiments to compare two promising nickel-based oxygen carriers for use in chemical-looping technologies,” *Fuel*, vol. 84, no. 2–3, pp. 283–296, 2005.

[271] P. Cho, T. Mattisson, and A. Lyngfelt, “A systematic investigation of the performance of copper-, cobalt-, iron-, manganese- and nickel-based oxygen carriers for chemical looping combustion technology

through simulation models," *Fuel*, vol. 83, no. 9, pp. 1215–1225, 2004.

[272] A. Abad et al., "Mapping the range of operational conditions for Cu-, Fe- and Ni-based oxygen carriers in chemical-looping combustion," *Chemical Engineering Science*, vol. 62, pp. 533–554, 2007.

[273] F. Garcia-Labiano et al., "Reduction and oxidation kinetics of copper-based oxygen carrier prepared by impregnation for chemical-looping combustion," *Industrial & Engineering Chemistry Research*, vol. 43, pp. 8168–8177, 2004.

[274] I. Iliuta, R. Tahoces and G. Patience, "Chemical-looping combustion process: Kinetics and mathematical modeling," *AIChE Journal*, vol. 56, pp. 1063–1079, 2010.

[275] C. Dueso et al., "Reduction and oxidation kinetics of nickel-based oxygen-carriers for chemical-looping combustion and chemical-looping reforming," *Chemical Engineering Journal*, vol. 188, pp. 142–154, 2012.

[276] G. Diglio, P. Bareschino, E. Mancusi and F. Pepe, "Novel quasi-autothermal hydrogen production process in a fixed-bed using a chemical looping approach: A numerical study," *International Journal of Hydrogen Energy*, vol. 42, no. 22, pp. 15010–15023, 2017.

[277] G. Diglio et al., "Feasibility of CaO/CuO/NiO sorption-enhanced steam methane reforming integrated with solid-oxide fuel cell for near-zero-CO_2 emissions cogeneration system," *Applied Energy*, vol. 230, pp. 241–256, 2018.

[278] G. Diglio, P. Bareschino, E. Mancusi and F. Pepe, "Simulation of hydrogen production through chemical looping reforming process in a packed-bed reactor," *Chemical Engineering Research and Design*, vol. 105, pp. 137–151, 2016.

[279] M. F. Edwards and J. F. Richardson, "Gas dispersion in packed beds," *Chemical Engineering Science*, vol. 23, pp. 109–123, 1968.

[280] S. Yagi and N. Wakao, "Heat and mass transfer from wall to fluid in packed beds," *AIChE Journal*, vol. 5, pp. 79–85, 1959.

[281] L. Han, Z. Zhou and G. Bollas, "Heterogeneous modeling of chemical-looping combustion. Part 1: Reactor model," *Chemical Engineering Science*, vol. 104, pp. 233–249, 2013.

[282] V. Spallina, P. Chiesa, E. Martelli, R. Gallucci, F. M. Romano, G. Lozza, e M. van Sint Annaland, "Reactor design and operation strategies for a large-scale packed-bed CLC power plant with coal syngas," *Int. J. Greenh. Gas Cont.*, vol. 36, pp. 34–50, 2015.

[283] J. R. Fernández e H. Abanades, "Conceptual design of a Ni-based chemical looping combustion process using fixed-beds," *Appl. Energ.*, vol. 135, pp. 309–319, 2014.

[284] M. P. Boyce, *Gas Turbine Engineering Handbook*, 4th ed. New York, USA: Butterworth-Heinemann, 2011.

[285] C. De Blasio, *Fundamentals of Biofuels Engineering and Technology*. Springer, 2019.

[286] I. Wender, "Reactions of synthesis gas," *Fuel Process. Technol.*, vol. 48, pp. 189–297, 1996.

[287] H. Boerrigter e R. Rauch, "Review of applications of gases from biomass gasification," ECN Biomass, Coal & Environmental Research, Report No. ECN-RX-06-066, giu. 2006.

[288] A. Ramos, E. Monteiro, V. Silva e A. Rouboa, "Co-gasification and recent developments on waste-to-energy conversion: A review," *Renew. Sustain. Energy Rev.*, vol. 81, pp. 380–398, 2018.

[289] G. Ruoppolo, P. Ammendola, R. Chirone e F. Miccio, "H_2-rich syngas production by fluidized bed gasification of biomass and plastic fuel," *Waste Manage.*, vol. 32, pp. 724–732, 2012.

[290] P. Brachi, R. Chirone, F. Miccio, M. Miccio, A. Picarelli e G. Ruoppolo, “Fluidized bed co-gasification of biomass and polymeric wastes for a flexible end-use of the syngas: Focus on bio-methanol,” *Fuel*, vol. 128, pp. 88–98, 2014.

[291] Q. Liu, C. Hu, B. Peng, C. Liu, Z. Li, K. Wu, H. Zhang e R. Xiao, “High H_2/CO ratio syngas production from chemical looping co-gasification of biomass and polyethylene with CaO/Fe_2O_3 oxygen carrier,” *Energy Convers. Manag.*, vol. 199, p. 111951, 2019.

[292] J. Zeng, R. Xiao, D. Zeng, Y. Zhao, H. Zhang e D. Shen, “High H_2/CO ratio syngas production from chemical looping gasification of sawdust in a dual fluidized bed gasifier,” *Energy Fuels*, vol. 30, pp. 1764–1770, 2015.

[293] F. Miccio, A. Picarelli e G. Ruoppolo, “Increasing tar and hydrocarbons conversion by catalysis in bubbling fluidized bed gasifiers,” *Fuel Process. Technol.*, vol. 141, pp. 31–37, 2016.

[294] F. D. Meylan, V. Moreau e S. Erkman, “CO_2 utilization in the perspective of industrial ecology, an overview,” *J. CO_2 Utiliz.*, vol. 12, pp. 101–108, 2015.

[295] S. Rönsch, J. Schneider, S. Matthischke, M. Schlüter, M. Götz, J. Lefebvre, P. Prabhakaran e S. Bajoh, “Review on methanation – From fundamentals to current projects,” *Fuel*, vol. 9, pp. 82–102, 2015.

[296] J. Kopyscinski, T. J. Schildhauer e S. M. A. Biollaz, “Production of synthetic natural gas (SNG) from coal and dry biomass - A technology review from 1950 to 2009,” *Fuel*, vol. 166, pp. 276–296, 2016.

[297] G. Diglio, P. Bareschino, E. Mancusi e F. Pepe, “Novel quasi-autothermal hydrogen production process in a fixed-bed using a chemical looping approach: A numerical study,” *Int. J. Hydrogen Energ.*, vol. 42, n. 22, pp. 15010–15023, 2017.

[298] G. Foment e K. B. Bischoff, *Chemical Reactor Analysis and Design*. John Wiley & Sons, 1979.

[299] J. Xu e G. F. Froment, "Methane steam reforming, methanation and water-gas shift: I. Intrinsic kinetics," *AIChE J.*, vol. 35, pp. 88–96, 1989.

[300] E. Altimari, L. Mancusi, S. Russo e S. Crescitelli, "Temperature wave-trains of periodically forced networks of catalytic reactors" *AIChE J.*, vol. 58, n. 3, pp. 899–913, 2012.

[301] S. Matthischke, S. Roensch e R. Güttel, "Start-up time and load range for the methanation of carbon dioxide in a fixed-bed recycle reactor" *Ind. Eng. Chem. Res.*, vol.57, n. 18, pp. 6391–6400, 2018.

[302] J. Gao, Y. Wang, Y. Ping, D. Hu, G. Xu, F. Gu e F. Su, "A thermodynamical analysis of methanation reactions of carbon oxides for the production of synthetic natural gas," *RSC Adv.*, vol. 2, p. 2358, 2012.

[303] A. Pandey, C. Larroche, E. Gnansounou, S. K. Khanal, C.-G. Dussap e S. Ricke, *Alternative Feedstocks and Conversion Processes for the Production of Liquid and Gaseous Biofuels*, 2nd ed., Academic Press, pp. 817–843, 2019.

[304] P. Bareschino, E. Mancusi, M. Urciuolo, A. Paulillo, R. Chirone e F. Pepe, "Life cycle assessment and feasibility analysis of a combined chemical looping combustion and power-o-methane system for CO_2 capture and utilization," *Renew. Sustain. Energy Rev.*, vol. 130, p. 109962, 2020.